

Index 35726 X  
ISSN 0867-888X

POLISH  
ACADEMY  
OF SCIENCES  
INSTITUTE  
OF FUNDAMENTAL  
TECHNOLOGICAL  
RESEARCH

NATIONAL  
ENGINEERING  
SCHOOL  
OF METZ

# ENGINEERING TRANSACTIONS

ROZPRAWY INŻYNIERSKIE - TRAITE d'INGENIERIE



QUARTERLY  
VOLUME 61  
ISSUE 1

WARSZAWA - METZ 2013



Faster online  
<http://et.ippt.pan.pl>

## Contents of issue 1 vol. LXI

- 3 T.D. MARUSICH, S. USUI, L. ZAMORANO, K. MARUSICH, J. LEOPOLD,  
*New advances in the machining of hard metals using physics-based modeling*
- 15 Ł. MAZURKIEWICZ, K. DAMAZIAK, J. MAŁACHOWSKI, P. BARANOWSKI,  
*Parametric study of numerically modelled delamination process in a composite structure subjected to dynamic loading*
- 33 P. BARANOWSKI, R. GIELETA, J. MAŁACHOWSKI, Ł. MAZURKIEWICZ,  
*Rubber structure under dynamic loading – computational studies*
- 47 M. ROŚKOWICZ, T. SMAL, *Research on the durability of adhesive composites*
- 65 M.S. WĘGŁOWSKI, C.B. HAMILTON, *An experimental investigation and modelling of Friction Stir Processing*

# ENGINEERING TRANSACTIONS

Founded 1952  
Appears since 1953

Copyright ©2013 by Institute of Fundamental Technological Research  
Polish Academy of Sciences, Warsaw, Poland

## Aims and Scope

ENGINEERING TRANSACTIONS promotes research and practise in engineering science and provides a forum for interdisciplinary publications combining mechanics with material science, electronics (mechanotronics), medical science and biotechnologies (biomechanics), environmental science, photonics, information technologies and other engineering applications. The Journal publishes original papers covering a broad area of research activities including experimental and hybrid techniques as well as analytical and numerical approaches. Engineering Transactions is a quarterly issued journal for researchers in academic and industrial communities.

## INTERNATIONAL COMMITTEE

S. A. ASTAPCIK ( <i>Byelorussia</i> )	P. PERZYNA ( <i>Poland</i> )
A. CARPINTERI ( <i>Italy</i> )	L. TOTH ( <i>France</i> )
G. DOBMANN ( <i>Germany</i> )	Z. WESOŁOWSKI ( <i>Poland</i> )
T. IWAMOTO ( <i>Japan</i> )	P. WOOD ( <i>U.K.</i> )
A. N. KOUNADIS ( <i>Greece</i> )	G. VOYIADJIS ( <i>USA</i> )
J. LIN ( <i>U.K.</i> )	R. ZAERA ( <i>Spain</i> )
T. ŁODYGOWSKI ( <i>Poland</i> )	

## EDITORIAL COMMITTEE

R. PEŁCHERSKI – <b>Editor</b>	A. RUSINEK – <b>Co Editor</b>
Z. AZARI	K. KOWALCZYK-GAJEWSKA
P. CHEVRIER	Z. KOWALEWSKI
B. GAMBIN	P. LIPIŃSKI
J. HOLNICKI-SZULC	K. KRIEDEL – assistant of the Co Editor

ENIM, 1 route d'Ars Laquenexy  
57078 Metz Cedex 03  
Phone: +33 3 87344266, E-mail: relinter@enim.fr

J. ŻYCHOWICZ-POKULNIEWICZ – secretary

Address of the Editorial Office:  
Engineering Transactions  
Institute of Fundamental Technological Research  
Pawińskiego 5B, PL 02-106 Warsaw, Poland

Phone: (48-22) 826 12 81 ext. 206, Fax: (48-22) 826 98 15, E-mail: engtrans@ippt.pan.pl

## Abstracted/indexed in:

Applied Mechanics Reviews, Current Mathematical Publications, Elsevier, EMBASE, Engineering Village, Inspec, Mathematical Reviews, MathSci, Reaxys, Scopus, Zentralblatt für Mathematik.

<http://et.ippt.pan.pl/>

**Address of the Editorial Office:**

Engineering Transactions  
Institute of Fundamental Technological Research  
Pawińskiego 5B  
PL 02-106 Warsaw, Poland  
Phone: (48-22) 826 12 81 ext. 206, Fax: (48-22) 826 98 15  
E-mail: engtrans@ippt.pan.pl

**SUBSCRIPTIONS**

**Subscription orders for all journals edited by Institute of Fundamental Technological Research (IPPT) may be sent directly to the Publisher: Institute of Fundamental Technological Research e-mail: subscribe@ippt.pan.pl**

Please transfer the subscription fee to our bank account:

Payee: IPPT PAN

Bank: Pekao S.A. IV O/Warszawa

Account number 05124010531111000004426875.

---

**WARUNKI PRENUMERATY**

**Prenumeratę na wszystkie czasopisma wydawane przez Instytut Podstawowych Problemów Techniki PAN przyjmuje Dział Wydawnictw IPPT.**

**Bieżące numery Engineering Transactions można nabyć bezpośrednio w Redakcji:**

**ul. Pawińskiego 5B, 02-106 Warszawa**

**Tel.: (48-22) 826 60 22; Fax: (48-22) 826 98 15**

**e-mail: subscribe@ippt.pan.pl**

## New Advances in the Machining of Hard Metals using Physics-Based Modeling

Troy D. MARUSICH, Shuji USUI, Luis ZAMORANO,  
Kerry MARUSICH, Juergen LEOPOLD

*Third Wave Systems, Inc.*

7900 West 78th Street Suite 300, Minneapolis, MN USA 55439  
e-mail: sales@thirdwavesys.com

The machining of hard metals historically has been understood to be challenging and costly due to its material properties (such as titanium’s low thermal conductivity and high hardness, and nickel’s rapid work-hardening and high strength at elevated temperatures) and limited understanding in industry of the physics behind chip formation and material removal. The achievement of meaningful cycle time reductions while maintaining part quality depends on a capability to model the physics of hard metal machining operations. With the help of a validated toolpath analysis model that can predict forces at each cutter location, cycle times and scrap can be reduced and machine breakdown can be avoided, all through off-line analysis. Productivity and process efficiency can be improved through simulation, drastically reducing testing setup and machining time. Physics-based modeling technology has been identified as a cost-effective solution for identifying optimum cutting speeds, enabling researchers and manufacturers to increase material removal rates, reduce machining costs, and enhance industry expertise in hard metal machining best practices. This paper presents new advances to physics-based modeling that have been validated using experimental tests and comparisons with finite element milling simulations, used to compare different process parameters and resulting material removal rates, and successfully advance hard metal machining processes.

**Key words:** machining, process improvement, CAE software, aircraft, metal, titanium.

### 1. INTRODUCTION

In addition to complicated toolpaths inherent in airframe components, the machining of titanium alloys and other hard metals pose several challenges due to low thermal conductivity, high specific cutting power [1] and high hardness. Commercially-available verification software products provide methods to optimize such toolpaths, but do not incorporate material behavior or cutting force prediction; [2, 3]. Several empirical models to predict cutting forces in machining processes have been well documented in the literature [4–8]; and yet, these

models are not sufficient to simulate the machining of complex aerospace components utilizing five-axis toolpaths and predict forces for thousands of cutter locations and dozens of tools in a quick and efficient manner. However complicated, implementing toolpath analysis into process design can yield a wide range of benefits in many different areas. With the help of a validated five-axis toolpath analysis model that can predict forces at each cutter location, cycle times and scrap can be reduced, and machine breakdown can be avoided, all through off-line analysis.

## 2. CAD GEOMETRY AND TOOLPATH IMPORT

Prediction of cutting forces requires identification of chip thickness and local cutting edge geometry along the flutes or contour of the cutting tool. Machining houses that manufacture monolithic aerospace components use complicated five-axis toolpaths typically generated with CAM packages [9, 10]. Commercially-available verification software [2, 11] can simulate the workpiece and tool geometries in either their own proprietary formats or in more universally accepted formats such as STP and STL files. While these packages provide a capability to import CNC toolpaths in generally accepted formats (such as G-code or APT code) and import the tool and workpiece geometry, none of these packages consolidate geometric information such as chip thickness and chip shape with material behavior of high temperature alloys to give a unified predictive model which considers the geometry as well as material behavior. The force model presented in this paper utilizes its own solid modeling technology, which allows for the capture of chip loads and process parameters such as cutting speeds, radial and axial depths of cut, etc., the data from which is in turn fed into the force calculation kernel described in the next section. The output of this model is thus in terms of forces, torque and horsepower, rather than just chip load and other process parameters such as cutting speeds.

A variety of helical end mill geometries are used in the metal cutting industry. Helical cylindrical, ball end, taper helical ball, bull nosed, and special purpose end mills are widely used in aerospace, automotive and die machining industries. Similar varieties also exist in drilling geometries. While the geometry of each cutter may be different, the mechanics of the milling process at each cutting edge point are common. The model presented in this paper discretizes the cutting geometry and applies empirically generated force data based on material behavior.

## 3. FORCE PREDICTIONS

Correlating the discretized force computations to the five-axis toolpath geometry is the most critical aspect of modeling the physics of machining operations.

The methodology presented herein utilizes a semi-empirical approach to capture the material properties in the form of force data. The force data is generated experimentally as a function of several variables such as cutting speed, feed, and tool geometry (back rake, side rake angles, etc.). Figure 1 shows a representative setup used to capture the cutting force data.

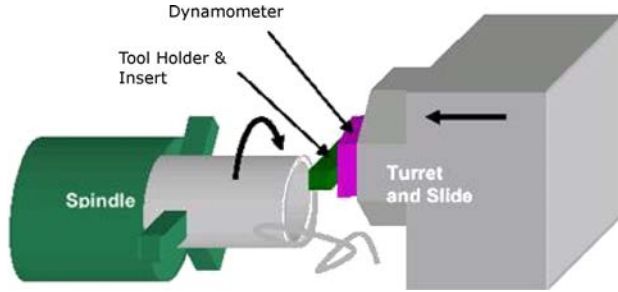


FIG. 1. Setup to capture turning force data.

Typically, force data is captured by performing tube turning measurements since these represent the simplest approach to capturing oblique cutting data. The data is captured in the form of axial, radial and tangential forces; thus for each material, tests are performed for several cutting conditions to cover the typical range of speeds, feeds and tool geometries in terms of rake angles [12].

Figure 2 shows the schematic to collect milling data using the plate dynamometer at Third Wave Systems' Productivity Center in Minneapolis, Minnesota. The force directions are captured in the coordinate system shown on the schematic, with the X-axis representing the feed direction.

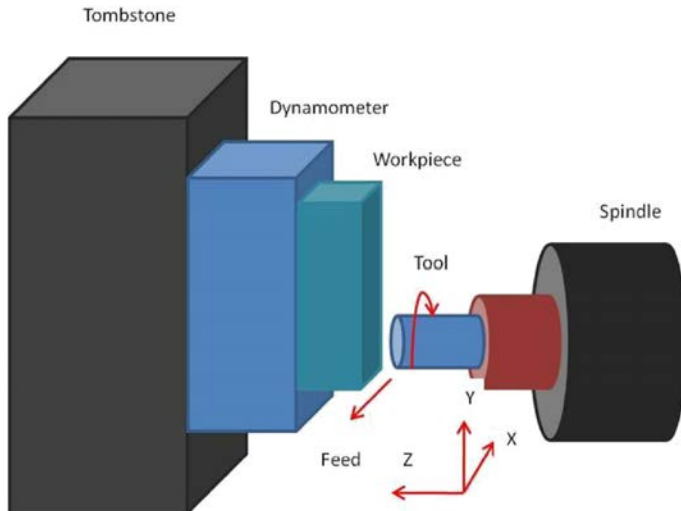


FIG. 2. Setup to capture milling force data.

## 4. EXPERIMENTAL VALIDATION

The model presented in this paper includes a material database that contains multiple materials, including commonly used aerospace and automotive materials such as titanium, nickel, aluminum, and steel alloys. Many standard tool geometries are also either readily available or can be imported in STP or STL format. This section contains a comparison between measured and predicted forces for validation from several different sources.

The first case is a validation of the force model in predicting drilling forces. A commonly used aerospace material, Ti-6Al-4V, was used as the workpiece material for modeling and testing. Forces were recorded using a Kistler 9255B table-mounted dynamometer at Third Wave’s Productivity Center. A total of eight cases were machined to measure both tangential ( $F_t$ ) and normal ( $F_n$ ) forces against predicted data. Figure 3 shows the comparison of measured and predicted force values.

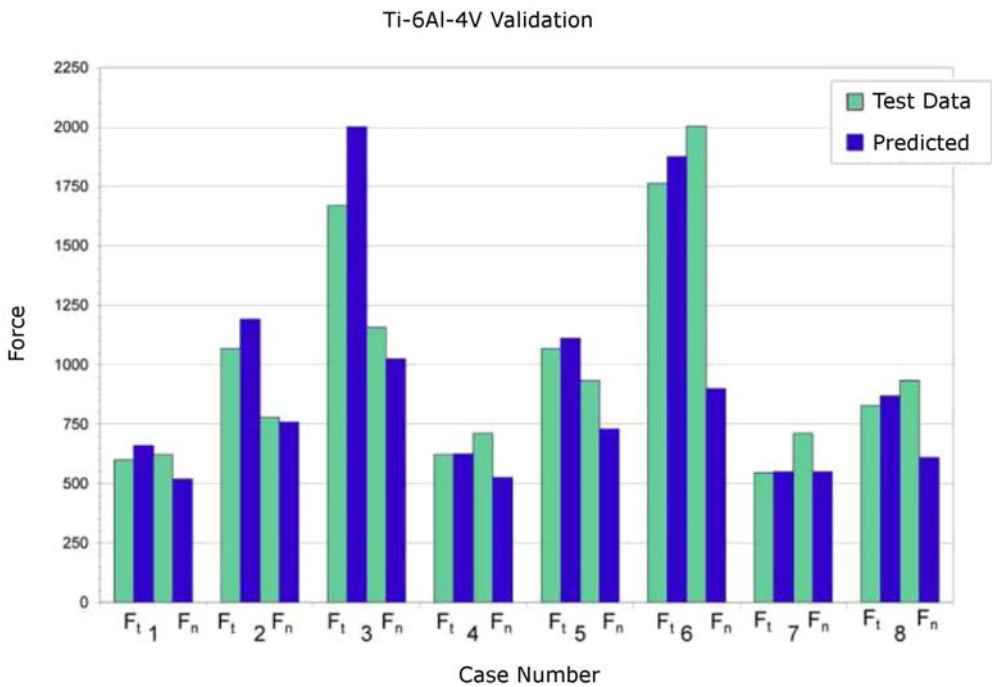


FIG. 3. Force comparison predicted by AdvantEdge FEM and measured by a dynamometer.

A second case, is validation of the force model predicting milling forces, as well as the material model prediction for chip shape. Figure 4 shows a machined chip, as well as the predicted chip behavior as modeled in AdvantEdge FEM 3D.

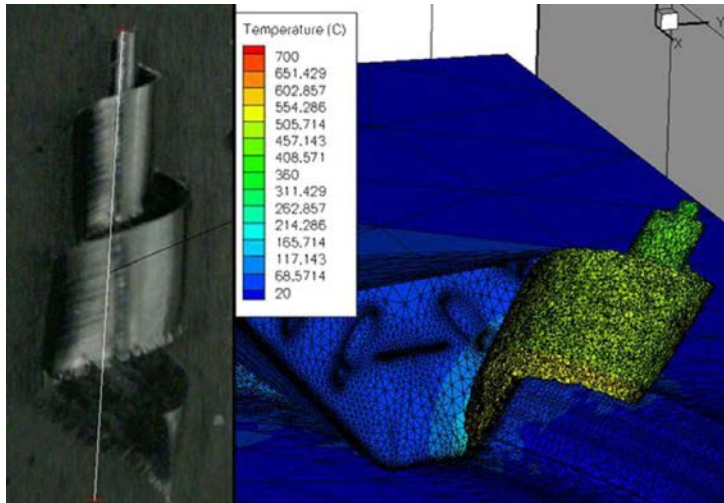


FIG. 4. Experimental test chip and predicted chip shape as modeled in AdvantEdge FEM 3D.

Figure 5 shows the predicted and measured forces of the milling operation along the X-, Y-, and Z-axes. This case was run at a speed of 146 RPM with a feed per tooth of 0.1 mm and a 40 percent radial depth of cut.

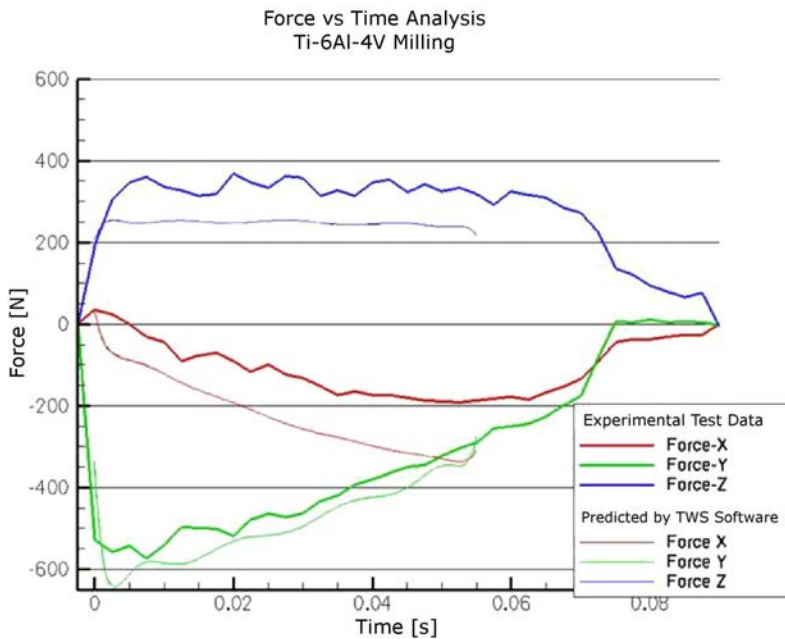


FIG. 5. Comparison of milling forces predicted by AdvantEdge FEM and measured by a dynamometer.

The third case is validation of a force model predicting power exerted on a Ti-6Al-2Sn-4Zr-2Mo workpiece. Figure 6 shows the measured spindle power labeled “TMac” compared with predictions of the force model labeled “PM” for the semi-finishing pass. Spindle power was measured using the Caron Engineering Tool Monitoring Adaptive Control-TMAC system [13]. The experimentally measured power consumption was then compared with the prediction of the force model. Instantaneous deviations between predicted and measured spindle power measurements can be primarily explained as the dynamic effects of the machine tool system that are captured experimentally.

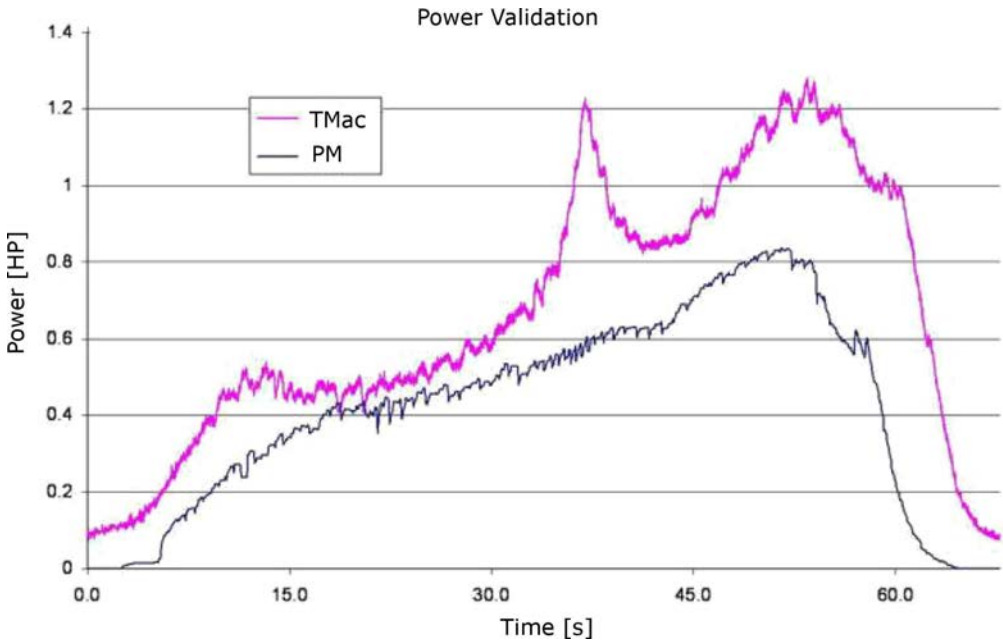


FIG. 6. Comparison of spindle power predicted by the model and measured by TMac for semi-finishing operation.

## 5. LOAD BALANCING APPROACH

With a validated model that predicts cutting forces (tool coordinate system: tangential, axial and radial; or workpiece coordinate system: X, Y and Z), torques, and spindle power, the next logical step is to utilize the model to identify areas of improvement to reduce cycle times without affecting the productivity.

Productivity improvements can be achieved by increasing the feed or speed during the cut. To increase the rate at which the tool is fed while performing a five-axis machining operation on a high temperature alloy such as a titanium or nickel alloy, material behavior and specific cutting power should be considered in addition to the tool-workpiece interactions from a purely geometric perspec-

tive. This is achieved by using the force model generated using the techniques illustrated in the “Force Predictions” section of this paper.

To increase productivity, an approach called “load balancing” was used to analyze cutting forces on the tool (e.g. tangential force) along the entire toolpath. There are instances where forces are at their peak, while at other instances along the toolpath the same tool encounters much lower cutting forces. This is primarily an outcome of tool-workpiece geometric interaction (feeds, tool orientation, and tool and workpiece geometry) and workpiece material behavior (edge and corner radius affects on the chip load and cutting forces). The entire toolpath was analyzed and cutting forces encountered by the tool and workpiece during the entire toolpath for each cutter location were computed, for all tools being called out.

In a typical multi-axis pocketing operation, a tool enters the pocket at the bottom center and gradually cuts the pocket from “inside-out” in a rectangular motion; in some CAM packages this is referred to as “outward helical” operation. The tangential force signature encountered by a tool during this pocketing operation with a workpiece material of Ti-6Al-2Sn-4Zr-2Mo is shown in Fig. 7. Maximum forces are encountered at the beginning of the pocketing operation when the tool plunged blindly into the workpiece. While cutting speeds and feeds were kept constant throughout the pocketing operation, the chip load encountered by the tool varied throughout the pocketing operation. The tool initially encountered a peak force of 9682 N; for subsequent passes, it encountered forces of 6964 N. Thus, it was possible to increase feeds in this sequence where peak tangential forces encountered by the tool were still less than the total peak tangential force encountered by this tool during the entire operation.

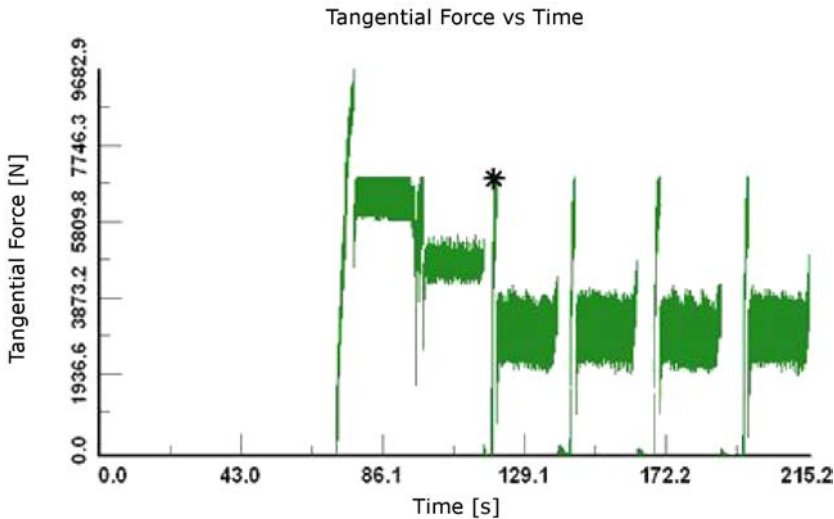


FIG. 7. Tangential force encountered by the tool.

The results, as shown in Fig. 7, are considered to be the baseline for load balancing. At each cutter location the model then compares the calculated baseline cutting forces against the upper and lower force limits set by the user. If the allowable force is higher than the currently calculated force, the feed is increased to achieve the maximum allowable force. If the allowable force is lower than the force calculated in the baseline, the feed is reduced proportionately to achieve a lowered force. The word *optimization* is used in this sense to indicate the load balancing approach; these two phrases are used interchangeably throughout the remainder of this paper.

For the baseline force signature shown in Fig. 7, if a minimum force limit of 7100 N is specified and the maximum force limit of 9682 N is maintained, the optimization yields a new sequence time of 119.8 seconds. With a baseline sequence time of 215.2 seconds, this means an approximate savings of 44 percent, as shown in Fig. 8. Notice that the peak force encountered by the tool did not exceed the original maximum value of 9682 N. It is important to note that during load balancing, spindle speeds were kept unchanged.

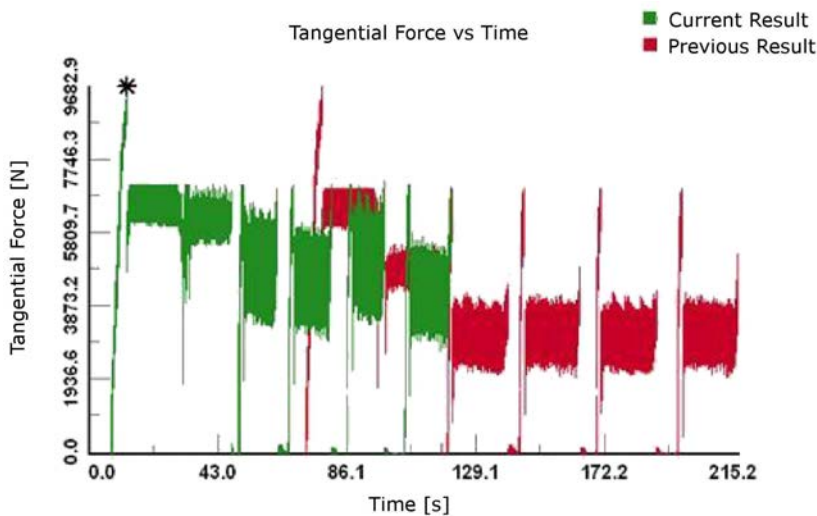


FIG. 8. Comparison of baseline (previous result) and optimized (current result) force signatures.

## 6. APPLICATION

Consider an aerospace part machined from a Ti-6Al-4V rectangular plate with dimensions of 285 mm  $\times$  160 mm  $\times$  55 mm. The minimum thickness of the walls is 7 mm and the lowest feed/tooth is 0.025 mm/tooth. Thus this simulation requires a scale difference of 285 mm/0.025 mm – 11360X – to represent its longest to shortest length scales and capture several magnitude length scales in between. The part calls in four different tools to perform several pocketing

operations on the rectangular plate to achieve the final part geometry. Figure 9 shows the finished workpiece geometry along with the toolpath.

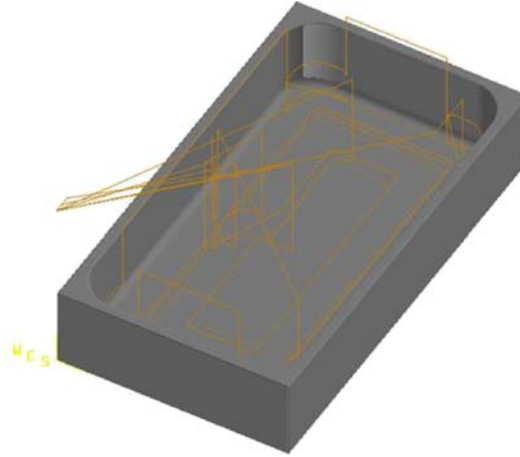


FIG. 9. Aerospace pocket component.

For the sake of the current example, only representative operations by each tool were considered; thus, the total cycle time of the entire part was only a fraction of total cycle time. Each tool encountered different maximum and minimum chip loads and correspondingly different maximum and minimum cutting forces. Figure 10 shows the baseline results noted as “previous results” (tangen-

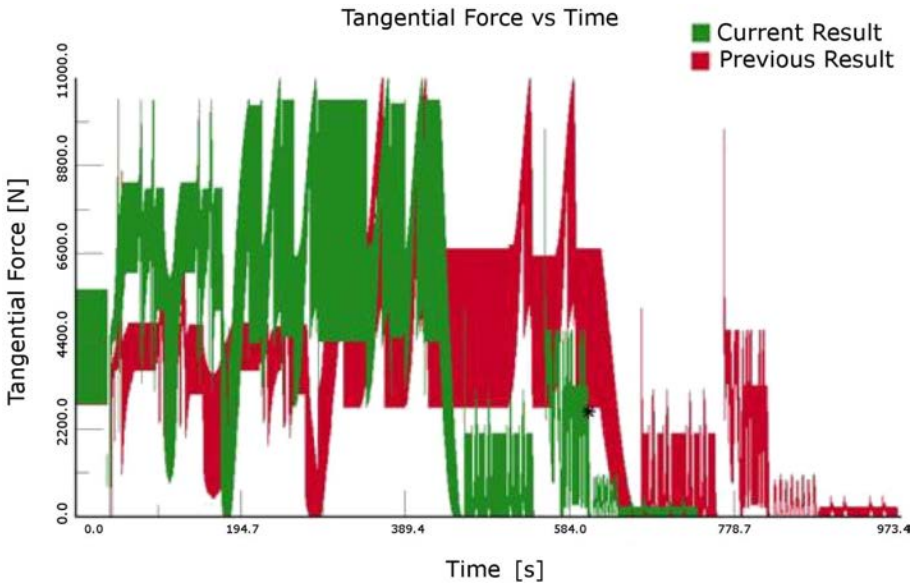


FIG. 10. Comparison of baseline and optimized force signature.

tial forces before load balancing) as well as optimized results noted as “current results” (tangential forces after load balancing.) The total “in cut” machining cycle time for all four tools was reduced from 973 seconds to 734 seconds, approximately a 25 percent improvement in productivity. It is important to note that the peak forces encountered by each tool were different and, correspondingly, the limits of tangential forces used to balance the loads on each tool were set separately.

The example above utilized only changes to the cutting feeds. Other approaches to further improve productivity, such as additional analysis using different tool geometries or toolpaths, are beyond the scope of this paper, yet yield even higher savings in cycle times using the same predictive force model presented here.

## 7. CONCLUSION

An accurate prediction of five-axis machining process behavior, including cutting forces and horsepower consumption, is necessary for the understanding of the process and for subsequent improvements to be made. It is possible to predict forces over the entire toolpath using analytical and numerical techniques to extend an empirical database to generalized cutting conditions. This semi-empirical model is able to predict torque and cutting forces encountered by the tool for drilling and milling operations. Using the same model, it is also possible to achieve a tangible reduction of cycle time while maintaining part quality.

## REFERENCES

1. STEPHENSON D.A., AGAPIOU J.S., *Metal Cutting Theory and Practice*, Second Edition, CRC, Boca Raton, FL, 19, 2006.
2. CG Tech, Vericut, [www.cgtech.com/usa/products/](http://www.cgtech.com/usa/products/).
3. DIEHL S.A., *TrueMill<sup>®</sup> White Paper*, [www.surfware.com/truemill\\_toolpath\\_strategies.aspx](http://www.surfware.com/truemill_toolpath_strategies.aspx)
4. DEVOR R.E., KLINE W.A., ZDEBLICK W.J., *A Mechanistic Model for the Force System in End Milling with Application to Machining Airframe Structures*, Proceedings of the 8th North American Manufacturing Research, 297, 1980.
5. NAKAYAMA K., ARAI M., TAKEI K., *Semi-empirical equations for three components of resultant cutting force*, Annals of the CIRP, **32**, 1, 33–35, 1983.
6. BROWN C.A., *A Practical Method for Estimating Forces from Tool-chip Contact Area*, Annals of the CIRP, **32**, 1, 91–95, 1983.
7. STEPHENSON D.A., AGAPIOU J.S., *Calculation of Main Cutting Edge Forces and Torque for Drills with Arbitrary Point Geometries*, International Journal of Machine Tool Manufacturing, **32**, 4, 521–538, 1992.

8. SRINIVAS B.K., *The Forces in Turning*, SME Technical Paper, MR82-947, 1982.
9. Siemens PLM Software, NX CAM, [www.plm.automation.siemens.com/en\\_us/products/nx/machining/machining/index.shtml](http://www.plm.automation.siemens.com/en_us/products/nx/machining/machining/index.shtml).
10. Dassault Systems, CATIA, [www.3ds.com/products/catia/catia-discovery/](http://www.3ds.com/products/catia/catia-discovery/).
11. Predator Software Inc., Predator SDK, [www.predator-software.com/virtualcnc.htm](http://www.predator-software.com/virtualcnc.htm).
12. STEPHENSON D.A., BANDOPADHYAY P., *Process-Independent Force Characterization for Metal Cutting Simulation*, Transactions of the ASME, **119**, 1997.
13. Caron Engineering, Inc., [www.caron-eng.com/](http://www.caron-eng.com/).

*Received May 10, 2011; revised version January 4, 2013.*

---

# Parametric Study of Numerically Modelled Delamination Process in a Composite Structure Subjected to Dynamic Loading

Łukasz MAZURKIEWICZ, Krzysztof DAMAZIAK,  
Jerzy MAŁACHOWSKI, Paweł BARANOWSKI

*Military University of Technology*  
*Faculty of Mechanical Engineering*  
*Department of Mechanics and Applied Computer Science*  
Kaliskiego 2, 00-908 Warszawa, Poland  
e-mail: {lmazurkiewicz, kdamaziak, jerzy.malachowski, pbaranowski}@wat.edu.pl

Composite materials, especially those fibre reinforced, thanks to their advantages, are being used in a growing number of industries. However, the complex structure of these materials results in many analytical problems. One such problematic field is to model failure of a composite, and especially the delamination process. The aim of this paper is to find a suitable method of layer connection modelling with the ability to describe delamination phenomena. A few chosen modelling parameters are investigated with respect to a parametric delamination numerical model.

**Key words:** fibre reinforced laminates (FRC), progressive crushing, cohesive modelling.

## 1. INTRODUCTION

Composite materials, particularly Fibre Reinforced Laminates (FRC), among other advantages are characterized by high specific strength and stiffness, weather resistance and increasingly lower costs of production. Elements made of composite materials also have high crashworthiness, which means that they are able to absorb a high amount of impact energy. Moreover, energy absorption can proceed in a controlled way [1, 2]. Thanks to its properties, composites make an excellent material for panels that reduce the effects of energy-intensive load due to outbreak acting on structural components [3]. However, to get the best energy-absorbing properties, it is necessary to conduct analyses of such panels to optimize its shape and internal layout, though the internal structure of FRC cause a number of modelling difficulties. Besides complex material properties, it is also very important to map destruction mechanisms of fibres and the matrix.

Due to the large amount of absorbed energy, the process of progressive crushing, where the main mechanism is delamination of the individual composite layers, is of particular interest. Since the analysis of elements made of FRC requires very complex modelling tools and, with the number of different coefficients included [4, 5], the influence of these coefficients on results and behaviour of the numerical model should be investigated. Because progressive crush phenomena are of particular interest in energy absorbing applications, the authors have focused their attention on several parameters related to delamination modelling.

Over recent decades, the modelling of progressive crush of FRC has attracted the attention of many researchers. Numerous modelling methods were developed in order to properly describe delamination phenomena. One of the most popular approaches is to use the so called decohesion material model. The cohesive-zone concept was originally introduced by BARENBLATT [6] and DUGDALE [7] (some authors also recognize the contribution of LEONOV and PANASYUK [8]) to describe the near-tip fracture process, and it has gained great popularity as a tool for simulating delamination, debonding, fracture, and fragmentation, via the Finite Element Method (FEM). A body of publications showing this approach can be found. For instance, the authors of [9] reference around thirty of these. What should be noted though, is that only a few publications are available where the explicit simulation of progressive interface debonding were performed for a model with realistic geometry [10]. On the other hand, the application of composites for protection against outbreak requires quite large structural elements.

This paper shows one of the stages of research aimed to find the best way to include delamination in the simulation of real construction elements. Following some guidelines found in the literature, the very first FE models were made of shell elements (see Fig. 1a). Unfortunately, it so happens that this approach

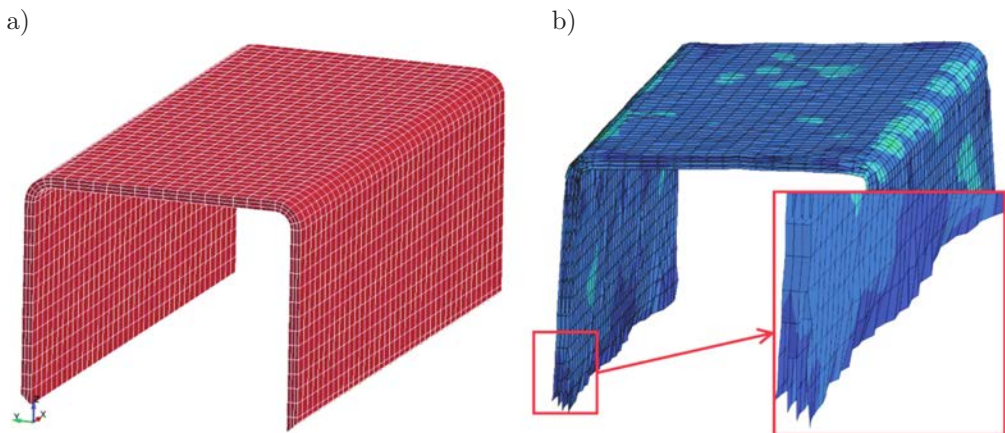


FIG. 1. a) Shell discret model of FRC element; and b) instabilities in a non-loaded model.

leads to numerical instabilities. Despite changes in shell element formulation or element size, it was not possible to stabilize the solution. A typical symptom of instabilities is shown in Fig. 1b, where stress and deformation fields on the free (not loaded) structure are presented.

Due to the above problems, it was decided that the analysed structure would be modelled using 3D hexagonal elements and 2D interface cohesive elements. Keeping in mind the stability problems of 2D models, the authors decided to repeat numerical tests on a small coupon, which was used to identify material properties. Additionally, in order to verify the stability of the problem as an influence of some parameters on analysis of the results, a parametric study was carried out.

## 2. RESEARCH OBJECT

The research object is a rectangular coupon as shown in Fig. 2a. It is made of FRC (glass fibres) and has dimensions, 50 mm  $\times$  25 mm  $\times$  5 mm. It consists of four layers, each made of a fabric composed of four unidirectional layers with directions  $0^\circ/45^\circ/90^\circ/-45^\circ$ . One end of coupon has a  $45^\circ$  chamfer, which

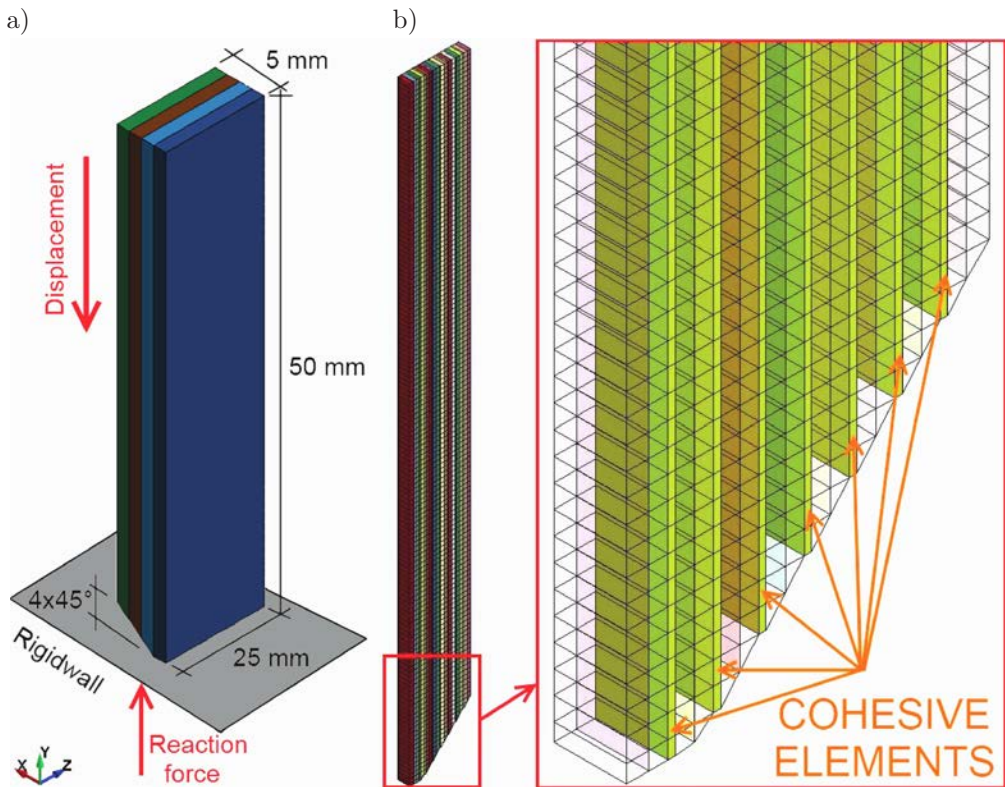


FIG. 2. a) Research object and b) discretisation of the research object.

serves as a delamination initiator. The FEM mesh is shown in Fig. 2b. Each layer was meshed using one row of hexagonal eight-node solid elements with one integration point. Layers were connected using eight-node cohesive interface elements.

Enforced motion along the  $y$ -axis was prescribed to the upper part of the coupon, while the bottom end impacted a rigid surface.

### 3. CONSTITUTIVE MODEL

Due to the nature of the investigated phenomena, the LS-Dyna explicit code was chosen as an analysis tool. From the number of composite material models available in the software, MAT\_162 was chosen. This material model is specially designated to model failure mechanisms observed in composite materials consisting of unidirectional and woven fabric layers, and its usefulness was confirmed by the authors [11, 12].

#### 3.1. Orthotropic material model for composite materials

In unidirectional laminates, the material properties are different along the fibre axis and along two other axes and thus the orthotropic material model is used in this research. The constitutive matrix is defined as [13]:

$$(3.1) \quad C^{-1} = \begin{bmatrix} \frac{1}{E_{aa}} & -\frac{\nu_{ab}}{E_{bb}} & -\frac{\nu_{ca}}{E_{cc}} & 0 & 0 & 0 \\ -\frac{\nu_{ab}}{E_{aa}} & \frac{1}{E_{bb}} & -\frac{\nu_{bc}}{E_{cc}} & 0 & 0 & 0 \\ -\frac{\nu_{ca}}{E_{aa}} & -\frac{\nu_{bc}}{E_{bb}} & \frac{1}{E_{cc}} & 0 & 0 & 0 \\ 0 & 0 & 0 & \frac{1}{G_{ab}} & 0 & 0 \\ 0 & 0 & 0 & 0 & \frac{1}{G_{bc}} & 0 \\ 0 & 0 & 0 & 0 & 0 & \frac{1}{G_{ca}} \end{bmatrix},$$

where  $E_{aa}$ ,  $E_{bb}$ ,  $E_{cc}$ ,  $G_{ab}$ ,  $G_{bc}$ ,  $G_{ca}$ ,  $\nu_{ab}$ ,  $\nu_{bc}$ ,  $\nu_{ca}$ , are material constants obtained from experimental tests.

The material layout with respect to the material axes is presented in Fig. 3.

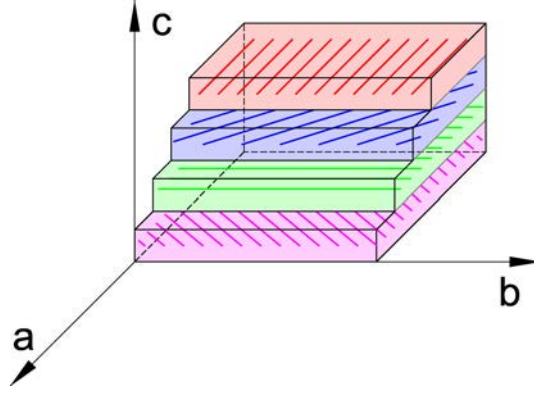


FIG. 3. Material directions.

### 3.2. Failure criteria for composite material

In the chosen material model layer, failure criteria have been established by adopting the methodology developed by Hashin [13] with a generalization to include the affect of highly constrained pressure on composite failure. The following failure criteria are available in the model [14]:

- Tensile/shear fibre failure mode

$$(3.2) \quad F_1 = \left( \frac{\sigma_a}{S_{aT}} \right)^2 + \left( \frac{\tau_{ab}^2 + \tau_{ca}^2}{S_{FS}^2} \right) - 1 = 0$$

- Compression fibre failure mode

$$(3.3) \quad F_2 = \left( \frac{\sigma'_a}{S_{aC}} \right)^2 - 1 = 0, \quad \text{where} \quad \sigma'_a = -\sigma_a + \left( -\frac{\sigma_b + \sigma_c}{2} \right)$$

- Fibre crush failure mode

$$(3.4) \quad F_3 = \left( \frac{p}{S_{FC}} \right)^2 - 1 = 0, \quad \text{where} \quad p = \left( -\frac{\sigma_a + \sigma_b + \sigma_c}{3} \right)$$

- Perpendicular matrix mode

$$(3.5) \quad F_4 = \left( \frac{\sigma_b^+}{S_{bT}} \right)^2 + \left( \frac{\tau_{bc}}{S'_{bc}} \right)^2 + \left( \frac{\tau_{ab}}{S'_{ab}} \right)^2 - 1 = 0, \\ \text{where} \quad S'_{bc} = S_{bc} + \tan(\varphi) (-\sigma_b)$$

- Parallel matrix mode

$$(3.6) \quad F_5 = \left( \frac{\sigma_c^+}{S_{cT}} \right)^2 + \left( \frac{\tau_{bc}}{S''_{bc}} \right)^2 + \left( \frac{\tau_{ca}}{S_{ca}} \right)^2 - 1 = 0, \\ \text{where} \quad S''_{bc} = S_{bc} + \tan(\varphi) (-\sigma_c)$$

In the equations above, the indices  $a, b, c$ , denote directions in the material coordinate system,  $T$  and  $C$  stand for tension and compression,  $\sigma$  and  $\tau$  are normal and shear stresses, and  $S$  are stress limits.

Static material properties were obtained from real-life tests (tension and compression in fibre and crossfibre directions, shearing in the planes 12, 23 and 31) and are shown in Table 1.

**Table 1.** Results of an experimental test of FRC.

Young modulus in tension (1)	$E_{aa}^t$	GPa	21.7
Young modulus in tension (2)	$E_{bb}^t$	GPa	605
Young modulus in compression (1)	$E_{aa}^c$	GPa	224
Young modulus in compression (2)	$E_{bb}^c$	GPa	748
Poisson (12)	$\nu_{ab}$	–	0.19
Poisson (21)	$\nu_{ba}$	–	0.099
Poisson (23)	$\nu_{bc}$	–	0.40
Shear modulus (12)	$G_{ab}$	GPa	3.20
Shear modulus (21)	$G_{ba}$	GPa	224
Shear modulus (32)	$G_{cb}$	GPa	167
Tensile strength (1)	$R_{aa}^t$	MPa	402
Tensile strength (2)	$R_{bb}^t$	MPa	344
Compression strength (1)	$R_{aa}^c$	MPa	375
Compression strength (2)	$R_{bb}^c$	MPa	110
Shear strength (12)	$S_{ab}$	MPa	458
Shear strength (21)	$S_{ba}$	MPa	477
Shear strength (32)	$S_{ca}$	MPa	337
Tension failure strain (1)	$e_{aa}^t$		0.020
Tension failure strain (2)	$e_{bb}^t$	–	0.0065
Compression failure strain (1)	$e_{aa}^c$	–	0.017
Compression failure strain (2)	$e_{bb}^c$	–	0.020
Shear failure strain (12)	$g_{ab}$	–	> 0.05
Shear failure strain (21)	$g_{ba}$	–	> 0.05
Shear failure strain (32)	$g_{ca}$	–	0.019

Data provided by M. Klasztorny, P. Gotowicki, D. Nycz, Military University of Technology, Department of Mechanics and Applied Computer Science.

### 3.3. Cohesive interface constitutive model

Besides composite material data, additional input defining the cohesive interface has to be defined. Its traction-separation behaviour was given by energy

release rates for modes I and II, and peak traction in the normal and tangential directions (Fig. 4). A detailed description of this model can be found in [15].

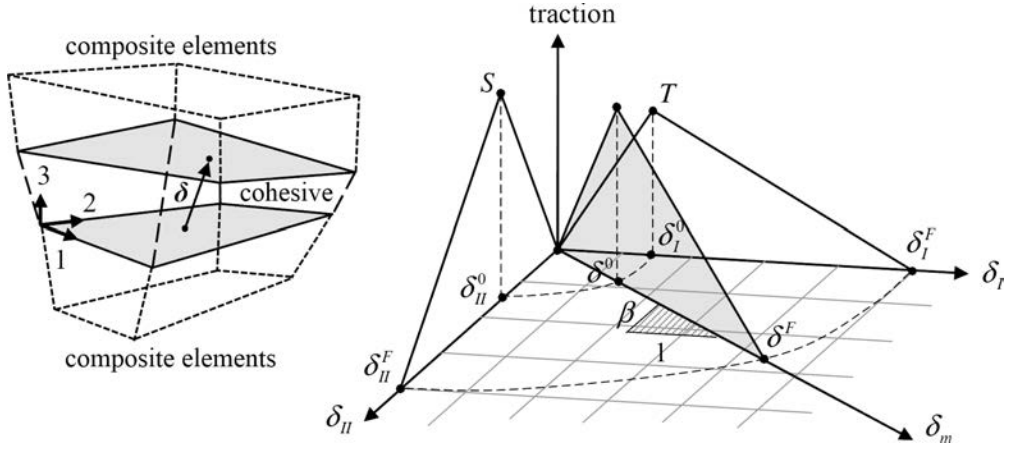


FIG. 4. Cohesive model used in analyses [15].

The ultimate mixed mode displacement is [15]:

$$(3.7) \quad \delta^F = \frac{1 + \beta^2}{\delta^0} \left[ \left( \frac{T}{G_{IC}} \right)^2 + \left( \frac{S\beta^2}{G_{IIC}} \right)^2 \right]^{-1/2} \quad \text{where } \beta = \delta_{II}/\delta_I$$

and where  $T$  and  $S$  are ultimate stress in normal and tangential directions,  $\delta_I$  and  $\delta_{II}$  are the separation in normal and tangential directions, and  $G_{IC}$  and  $G_{IIC}$  are the release energies for models I and II.

#### 4. PARAMETRIC STUDIES

Initial analyses of coupon crushing showed that the FE model has a very different displacement pattern compared to the one seen in real-life tests. Since material data were taken from real-life tests, the cause of different numerical model behaviour has to lie in typical FE-related problems, such as an inadequate contact model, mesh density, etc. Therefore, a parametric study of the model was performed concerning:

- thickness of cohesive elements,
- mesh density and density of interface elements,
- contact stiffness (penalty stiffness factor),
- properties of cohesive elements (energy release rate and peak traction),
- and with respect to maximum crushing force.

Numerical analyses were performed using a transient dynamics procedure with explicit central difference time integration. The equations to be solved have the following form:

$$(4.1) \quad M\ddot{x}_n = F_n^{\text{ext}} - F_n^{\text{int}} - C\dot{x}_n$$

where  $M$  is the diagonal mass matrix,  $F_n^{\text{ext}}$  is the external and body force loads,  $F_n^{\text{int}}$  is the stress divergence vector, and  $C$  is the dumping matrix.

#### 4.1. Thickness of cohesive elements

Three different thicknesses of cohesive elements were investigated: Case A – 0.00 mm, Case B – 0.01 mm, and Case C – 0.10 mm (see Fig. 5).

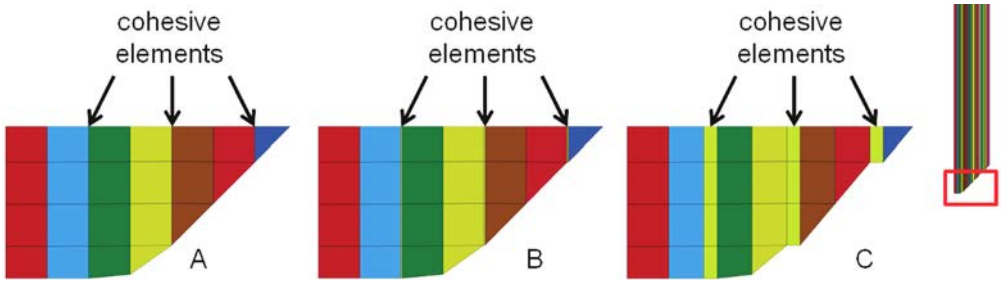


FIG. 5. Analysis cases – thickness of cohesive elements.

Displacement patterns are shown in Fig. 6. As one can see, Case A is numerically unstable, while Case C shows that the distance between composite layers is too big and, after separation (cohesive element failure), there is space allowing for artificial bending of layers.

The results obtained for Case B and Case C in terms of vertical force is shown in Fig. 7. It can be seen that the non-physical behaviour observed in the displacement pattern of Case C somehow does not strongly affect vertical force values.

The energy balance for Case B is presented in Fig. 8. The energy dissipated by cohesive elements has negative values (marked green). The internal energy of composite elements (red) is growing due to the deformation process and the total energy of the system is lower due to the process of dissipation.

The energy dissipated by the cohesive interface (Fig. 9) is significantly higher in Case B. This difference is caused by a different thickness of elements modelling composite layers, which was increased compared to Case C due to the reduced thickness of interface elements. Higher layer stiffness resulted in higher deformation of cohesive elements during coupon bending, since layers tended to separate instead of bend.

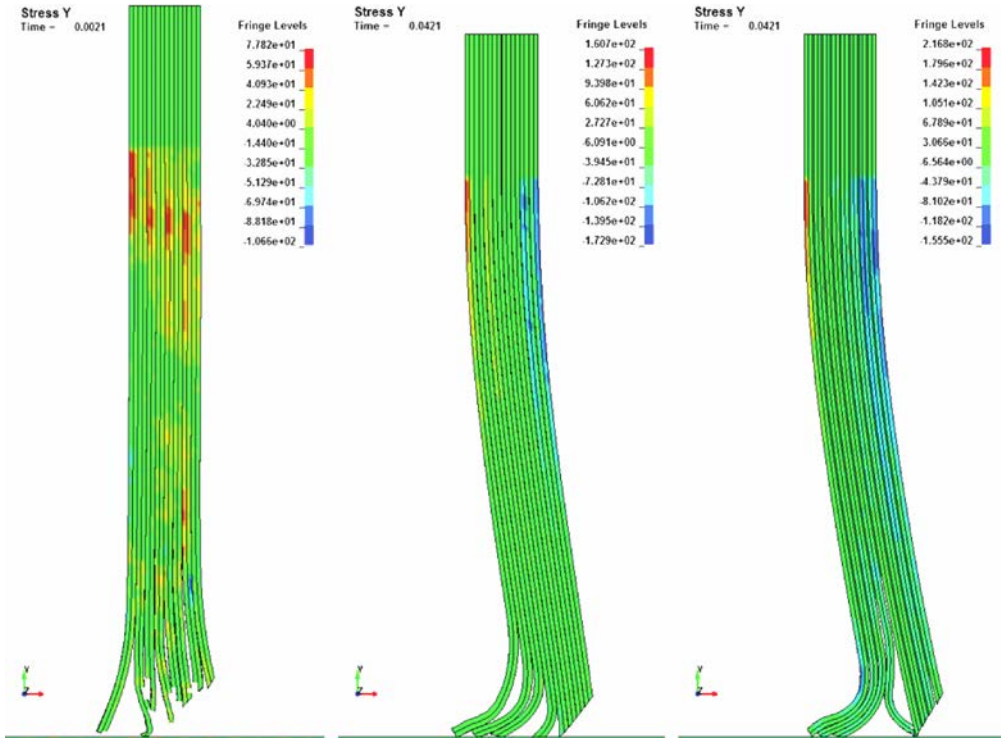


FIG. 6. Stress map and displacement of the models analysed (for model A, B and C, respectively).

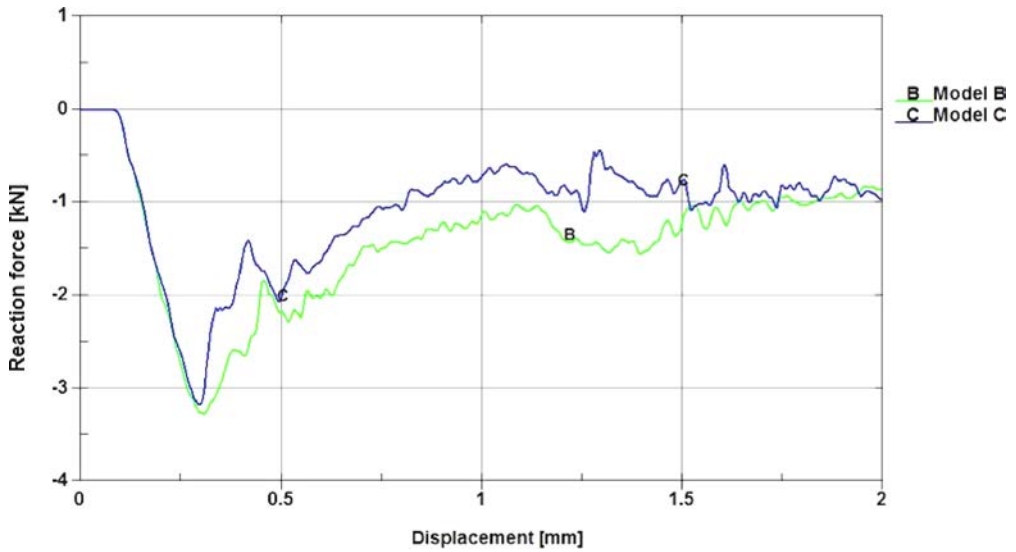


FIG. 7. Vertical force *versus* displacement for cases B and C.

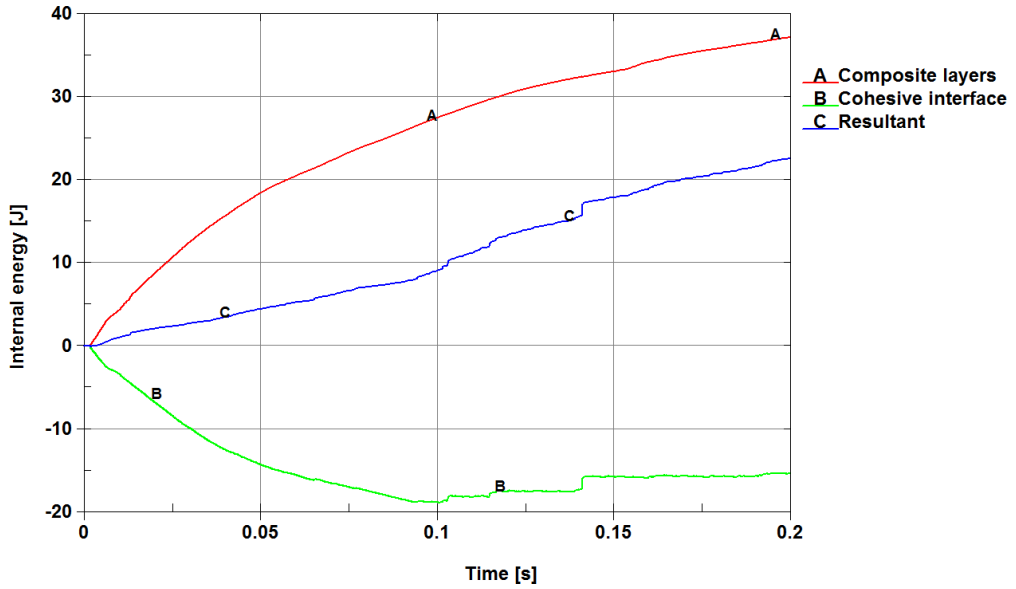


FIG. 8. Energy balance diagram.

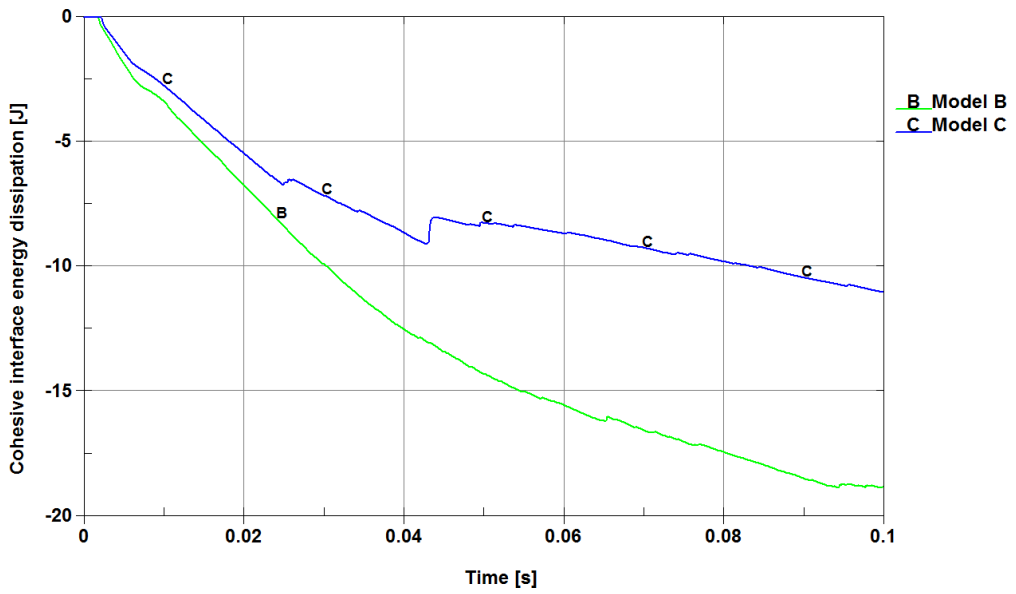


FIG. 9. Cohesive interface energy dissipation.

#### 4.2. Mesh density

Three different FE models were built, as described in Table 2. The mesh layouts obtained are shown in Fig. 10.

**Table 2.** Analysis of cases in a mesh density parametric study.

	Case A	Case B	Case C
Number of solid elements per layer (composite) thickness	1 (16)	1 (16)	2 (32)
Number of cohesive elements per composite thickness	7	15	15

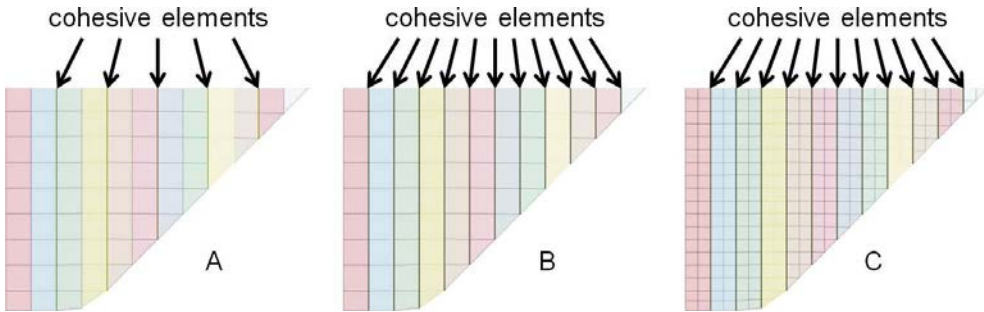


FIG. 10. Mesh layouts for the analysis of cases.

The deformed shapes of the model for all three cases are shown in Fig. 11. Once again it can be noted, that models with one element representing one

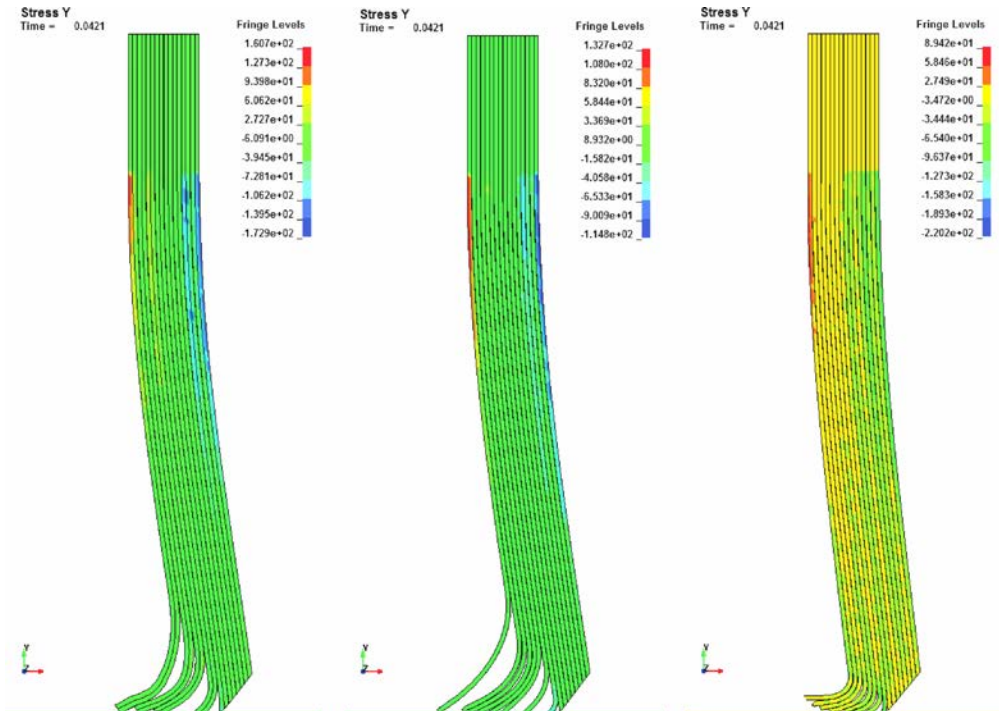


FIG. 11. Stress map and displacement of analysed models (respectively for model A, B and C according to Fig. 10).

layer are too stiff, preventing single layers from bending properly. This problem lays in the mathematical formulation of hexagonal elements with just one integration point as used in the examples presented. The usage of such simple elements is explainable and is because numerical analyses using explicit codes are always a trade off between integration speed and accuracy. Nevertheless, in the cases discussed, the low quality of elements obviously affected the results obtained.

The response of the models, with respect to vertical force is shown in Fig. 12. The curves obtained confirm the observation made based on deformation shapes. Case C, with two elements per layer, is less stiff than the other two.

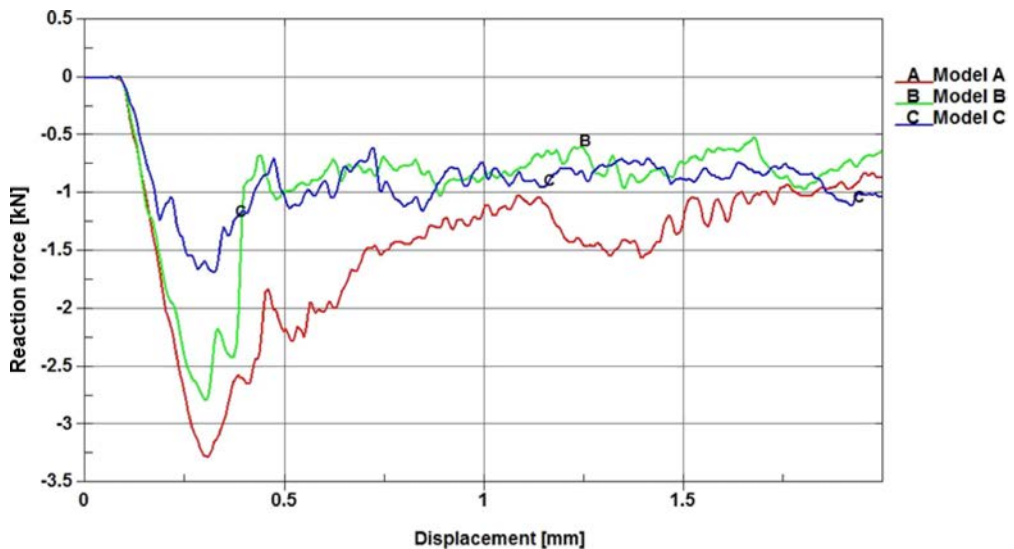


FIG. 12. Vertical force as a function of displacement for the analysed models.

The addition of cohesive interfaces (more delamination planes) in Model B result in higher energy being dissipated by that interface, as compared to Model A (Fig. 13).

The usage of a thickness of two elements per layer (Case C) allow a better description of bending, which result in lower stress values in the coupon and a more even load of cohesive elements. Model B is too stiff, which leads to the development of negative X stress components in the middle part of the coupon. These stresses prevent cohesive elements from opening. As a result, the dissipated energy is significantly smaller than in the case of the more flexible Model C.

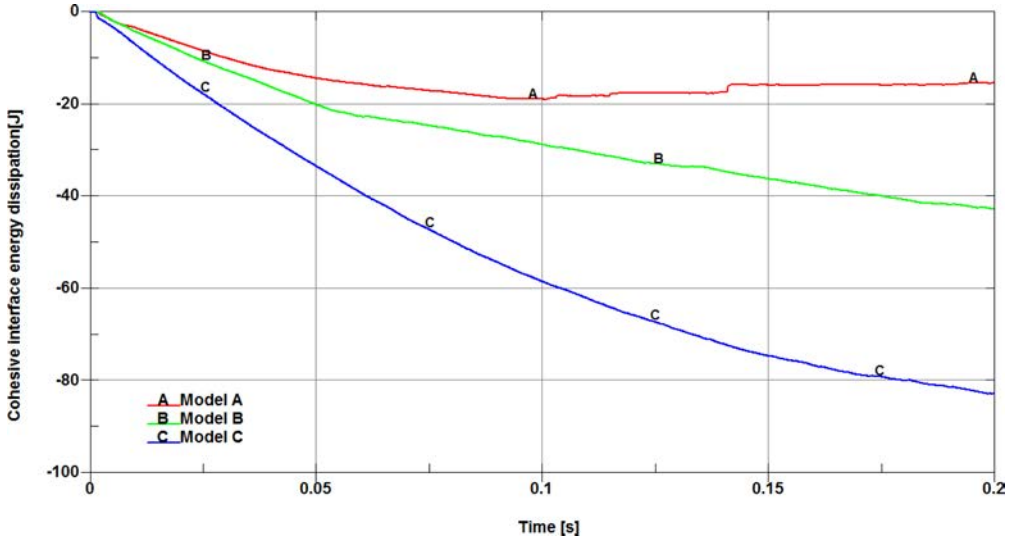


FIG. 13. Cohesive interface energy dissipation.

#### 4.3. Contact stiffness

The next parameter investigated was contact stiffness. The implemented contact formulation is based on a penalty function approach. In segment based contact, stiffness is described as follows:

$$(4.2) \quad k_{cs} = 0.5SLSFAC \left\{ \begin{array}{c} SFS \\ \text{or} \\ SFM \end{array} \right\} \left( \frac{m_1 m_2}{m_1 + m_2} \right) \left( \frac{1}{\Delta t_c(t)} \right)^2,$$

where  $SLSFAC$  is a scaling factor for sliding interface penalties,  $SFS$  is a scaling factor for slave penalty stiffness,  $SFM$  is a scaling factor for master penalty stiffness, and  $m_1$  and  $m_2$  are the masses of slave and master segments.

The stiffness factors  $SFS$  and  $SFM$  were changing in two contact interfaces:

- between base and composite – from 0.001 to 2,
- and between composite layers – from 0.001 to 2.

The results obtained are shown in Fig. 14. As can be seen, the penalty value in contact interfaces has no real influence on the vertical force, but very low values of contact stiffness between the base and composite cause a failure of the contact algorithm. The coupon model has penetrated through the base surface.

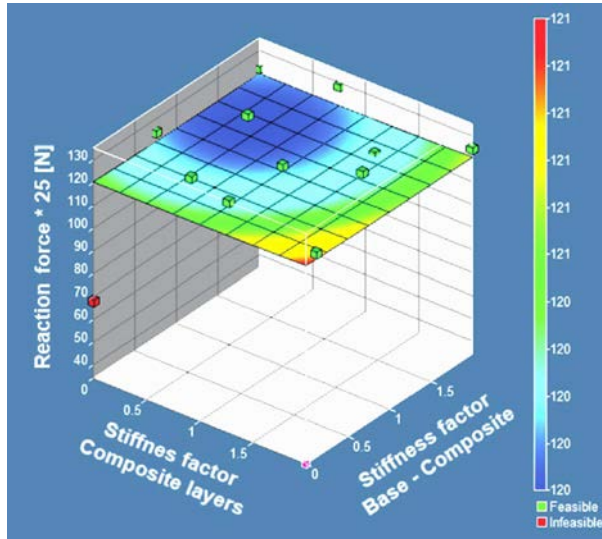


FIG. 14. Response surface of crushing force as a function of contact stiffness factors.

#### 4.4. Cohesive stiffness

The last parameter to be checked is the stiffness of cohesive elements. One particular reason to perform such study was to learn parametric of FE model on possible errors in  $G_I$  or  $G_{II}$  estimates. This time, the variable parameters were (see Fig. 15):

- energy release rate,  $G_{IC} = 0.01 \div 10 \text{ J/mm}^2$  and  $G_{IIC} = 5G_{IC}$ ,
- and peak traction in normal and tangential directions,  $T = 5 \div 100 \text{ MPa}$  and  $S = 2 T$ .

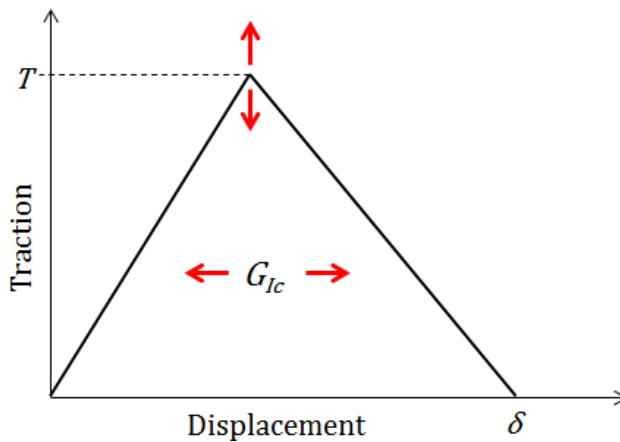


FIG. 15. Traction-separation curve for cohesive elements with red arrows representing changes in the variables.

The results of the analyses are shown on Fig. 16. It can be seen that the coupon FE model is very sensitive to changes in cohesive material properties as far as to make the numerical model unstable (higher values of energy release rates cause shear locking).

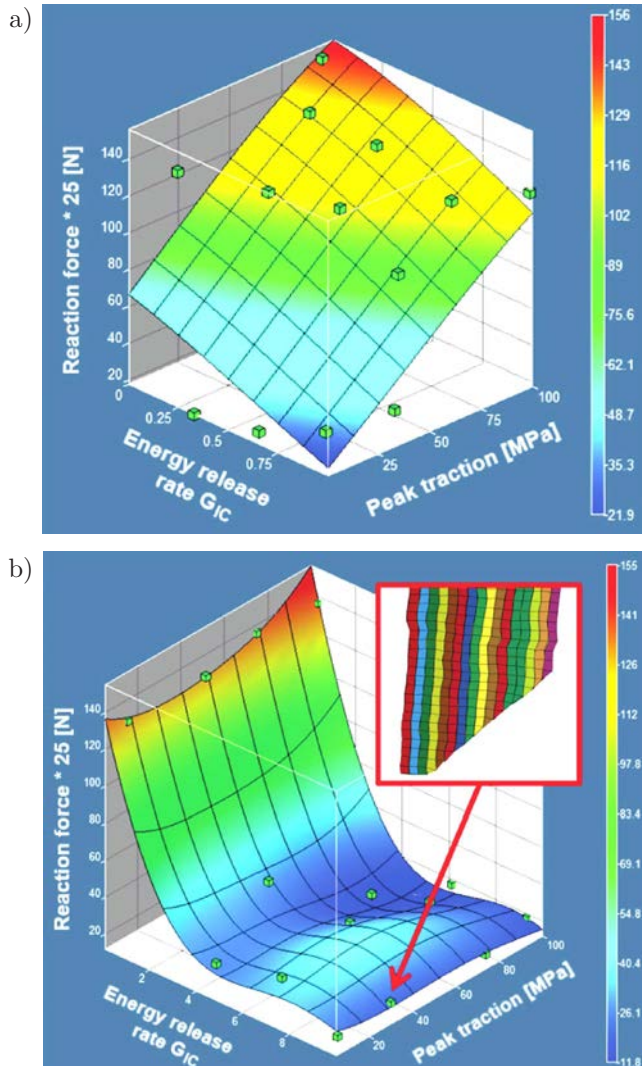


FIG. 16. Response surface of crushing force as a function of energy release rate and peak traction: a)  $G_{IC} = 0.01 \div 1 \text{ J/mm}^2$ ; and b)  $G_{IC} = 0.1 \div 10 \text{ J/mm}^2$ .

## 5. RESULTS DISCUSSION AND CONCLUSIONS

One of the most important conclusions is that numerical modelling of progressive crush phenomena is very challenging. Despite the fact that the cohesive

material model is well established, it is quite difficult to conduct a stable analysis of the process. Additionally, the internal structure of FRC has to be adequately described, which leads to very large and complicated FE models.

Typical limitations of (or rather, incorrect use of) the FE approach manifest themselves during tests. A too large thickness of interface elements leads to the generation of an artificial space between composite layers, which lead to nonphysical behaviour of layers after delamination. An insufficient number of elements-per-layer thickness makes that a single layer is too stiff for bending.

An analysis of the results obtained show that most of the investigated parameters do not greatly affect the crushing force value, with the exception of energy release rates. This means, that just like other material data,  $G_I$ ,  $G_{II}$ , and traction need to be accurately acquired. Therefore, material data taken from literature should be treated as preliminary data only. At the moment, the authors are carrying out real-life tests in order to obtain the fracture toughness of FRC. This means that both the experimental stages of material data acquisition as well as the FE analyses are very laborious and time consuming as far as the lack of usability in the case of modelling real objects is concerned.

#### ACKNOWLEDGMENT

The research was carried out under a research grant from the Polish Ministry of Science and Higher Education, no. 0097/R/T00/2010/12. This support is gratefully acknowledged.

#### REFERENCES

1. OCHELSKI S., BOGUSZ P., KICZKO A., *Static axial crush performance of unfilled and foamed-filled composite tubes*, Bulletin of the Polish Academy of Sciences Technical Sciences, **60**, 1, 31–35, 2012.
2. ZANGANI D., ROBINSON M., GIBSON A.G., *Progressive Failure of Composite Hollow Sections with Foam-Filled Corrugated Sandwich Walls*, Appl. Compos. Mater., **14**, 325–342, 2007.
3. TEKALUR S.A., SHUKLA A., SHIVAKUMAR K., *Blast resistance of polyurea based layered composite materials*, Composite Structures, **84**, 271–281, 2008.
4. GAMA B.A., GILLESPIE J.W. JR., *Finite element modeling of impact, damage evolution and penetration of thick-section composites*, International Journal of Impact Engineering, **38**, 181–197, 2011.
5. XIAO J.R., GAMMA B.A., GILLESPIE J.W. JR., *Progressive damage and delamination in plain weave S-2 glass/SC-15 composites under quasi-static punch-shear loading*, Composite Structures, **78**, 182–196, 2007.
6. BARENBLATT G.I., *The formation of equilibrium cracks during brittle fracture: general ideas and hypotheses axially symmetric cracks*, Appl. Math. Mech., **23**, 622–36, 1959.

7. DUGDALE D.S., *Yielding of steel sheets containing slits*, J. Mech. Phys. Solids, **8**, 100–4, 1960.
8. LEONOV M.Y., PANASYUK V.V., *The micro cracks development in a solid* [in Ukrainian], Prikladnaya Mekhanika, **5**, 391–401, 1959.
9. VALOROSO N., CHAMPANEY L., *A damage-mechanics-based approach for modelling decohesion in adhesively bonded assemblies*, Engineering Fracture Mechanics, **73**, 2774–2801, 2006.
10. SEVKAT E., LIAW B., DELALE F., RAJU B.B., *A combined experimental and numerical approach to study ballistic impact response of S2-glass fiber/toughened epoxy composite beams*, Composites Science and Technology, **69**, 965–982, 2009.
11. HUFENBACH W., LANGKAMP A., HORNIG A., ZSCHEYGE M., BOCHYNEK R., *Analysing and modelling the 3D shear damage behaviour of hybrid yarn textile-reinforced thermo-plastic composites*, Composite Structures, **94**, 121–131, 2011.
12. KUSHCH V.I., SHMEGERA S.V., MISHNAEVSKY L. JR., *Explicit modeling the progressive interface damage in fibrous composite: Analytical vs. numerical approach*, Composites Science and Technology, **71**, 989–997, 2011.
13. HASHIN Z., *Failure Criteria for Unidirectional Fiber Composites*, J. Appl. Mech., **47**, 2, 329–335, 1980.
14. *LS-Dyna Keyword User's Manual Volume I*, February 14, 2012 (revision: 1197), Version 971, Livermore Software Technology Corporation (LSTC).
15. GERLACH S., FIOLOKA M., MATZENMILLER A., *Modelling and analysis of adhesively bonded joints with interface elements for crash analysis*, Konferenzbeitrag zum 4. LS-DYNA FORUM, Bamberg, DYNAmore GmbH, Stuttgart, October 20–21, 2005.
16. HALLQUIST J.O., *LS-Dyna Theory manual*, March 2006, Livermore Software Technology Corporation (LSTC).

*Received May 25, 2012; revised version November 27, 2012.*

---



## Rubber Structure under Dynamic Loading – Computational Studies

Paweł BARANOWSKI, Roman GIELETA, Jerzy MAŁACHOWSKI,  
Łukasz MAZURKIEWICZ

*Military University of Technology  
Department of Mechanics and Applied Computer Science*

Gen. S. Kaliskiego 2, 00-908 Warszawa, Poland  
e-mail: pbaranowski@wat.edu.pl

This study focuses on the rubber structure behaviour assessment under dynamic loading using numerical methods. Dynamic simulations of the TNT explosion under the tire-suspension system were performed using the explicit LS-Dyna code using Arbitrary Lagrangian-Eulerian formulation with Jones Wilkins Lee (JWL) equation defining the explosive material. During analyses two different constitutive materials were used: Mooney-Rivlin without rate-dependency and Ogden rubberlike material (MAT 181 Simplified Rubber) which includes strain rate effects. Consequently, tire rubber material behaviour was investigated and compared for two simulated cases.

**Key words:** rubber, constitutive models, strain rate, dynamic loading, suspension system, tire.

### 1. INTRODUCTION

Due to its mechanical characteristics, including ability to reversible deformation under the loading of mechanical forces, rubber is very popular in various forms in many industries. One of these branches is the automotive industry, where materials and rubber-based composites are often used to produce tires with high strength and durability. Moreover, elastomeric structures because of their low modulus and high damping characteristics are used to absorb energy in dynamic loadings (impulse or impacts) as isolations bearings, shocks absorbers, etc. All above shows that an accurate assessment of their mechanical properties in various operational conditions have much importance in engineering applications. After material development there is a need to conduct experiments to determine the material properties and to validate a specific model of rubber.

Therefore, the dynamic behaviour of the elastomeric material at high and low strain rates have to be examined.

Mechanical properties of rubber in static experimental tests were effectively determined and understood [1, 2] and the behaviour under high-strain rates loading recently becomes more thoroughly investigated with both compression and tension characteristics taking into consideration. Based on literature review it can be noticed that majority of authors determined compression behaviour of elastomers using modified versions of Split Hopkinson Pressure Bar device [3–6] or using finite element method simulating various types of dynamic loading [7–9].

Several authors published results of the dynamic tensile tests, which were performed on the high speed extension device based on a Charpy impact tester [3, 10, 11], using the freely expanding ring technique [12, 13] or using the catapult apparatus [3]. Generally, rubber-like materials behaviour was assessed in strain rates between  $200 \text{ s}^{-1}$  (catapult apparatus) through  $435 \text{ s}^{-1}$  (Charpy impact tester) up to  $13800 \text{ s}^{-1}$  (expanding ring). Based on above it can be concluded that mechanical behaviour of major elastomeric structures mainly depends on large strains, high strain rate (above  $10 \text{ s}^{-1}$ ) and nonlinear viscoelastic response.

Furthermore, it should be pointed out that in presented results failure strain increases with strain rate and also the maximum stresses rises with strain rates but at some point stress-strain curves become almost invariant to rate. This phenomenon is presented in Fig. 1a, which shows an influence of strain rate on the yielding process of the steel material and in Fig. 1b illustrating the comparison stress-strain characteristics of rubber-like materials in different strain rates.

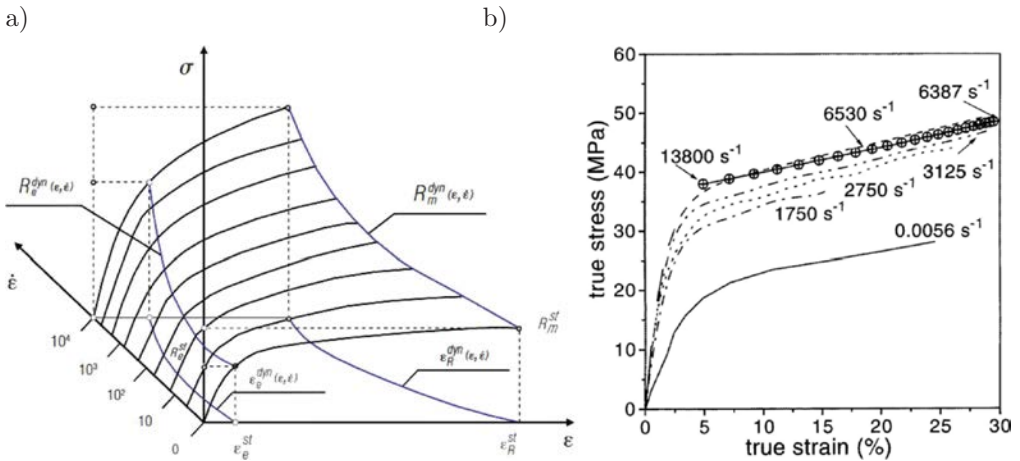


FIG. 1. a) Influence of strain rate on the yielding process of steel material [14] and b) comparison of stress/strain curves for rubber-like materials [3].

The authors of this paper decided to carry out numerical computations of an explosion under the terrain vehicle tire with suspension system. The main objective was to examine a dynamic behaviour of the tire with blast pressure propagation velocity taking into account, which together with other factors like strain rates, gas products characteristics, high reaction rate and exothermic effects have the biggest influence on how the detonation proceeds and what destruction it has [15, 16].

## 2. ANALYSES CONDITIONS

An object of investigations of presented researches is the suspension system with the tire. The major suspension system parts are: motor-car body, longitudinal, spring, axle, axle bush, hub, drum brake, steel rim and wheel. Geometries of the wheel and other suspension elements were achieved thanks to the reverse engineering technology [17, 18] (Fig. 2).

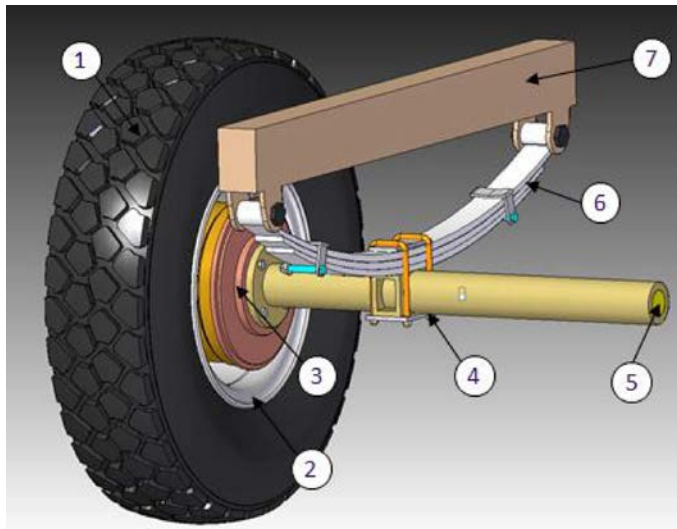


FIG. 2. Suspension system model, 1) Tire, 2) Drum brake, 3) Rim, 4) Axle bush, 5) Axle, 6) Spring, 7) Longitudinal and other hidden elements.

As mentioned before, material model with rate dependency (Ogden rubber-like material) and without rate effect taking into consideration (Mooney-Rivlin) were used in numerical analyses and results for both cases were compared. Material parameters for Mooney-Rivlin were estimated from one of the curves (for a quasi-static loading), which were used in Ogden rubberlike material also. Thus, in order to consider rate dependency in Ogden rubberlike material the load curve defining stress-strain characteristic of the material was replaced by the table with

a number of load curves defining the material response at the different strain rate (Fig. 3) [7]. Each material was implemented into the tire rubber major elements like tread and sidewall.

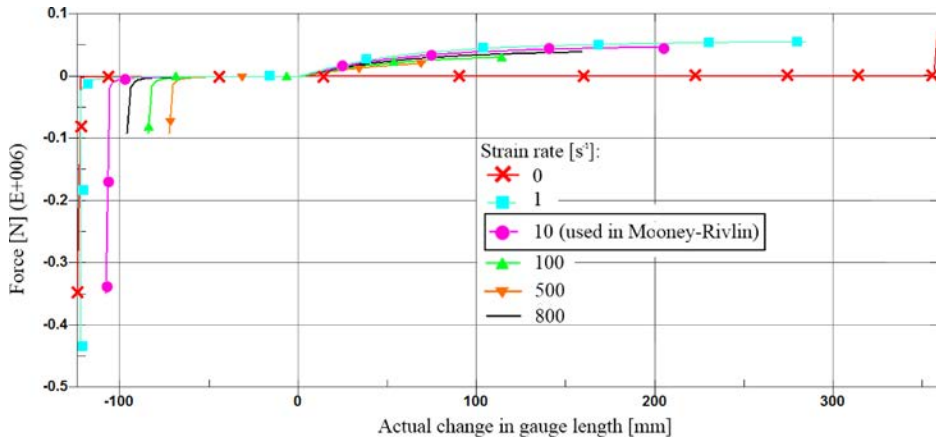


FIG. 3. Force *versus* actual change in gauge length for different strain rates [7].

Also, similar to the actual tire, steel cords were arranged inside radially and circumferentially [20–22]. A detailed description of the tire modelling can be found in the previous authors literature [17, 18]. FE model of the tire (without tread) is presented in Fig. 4.

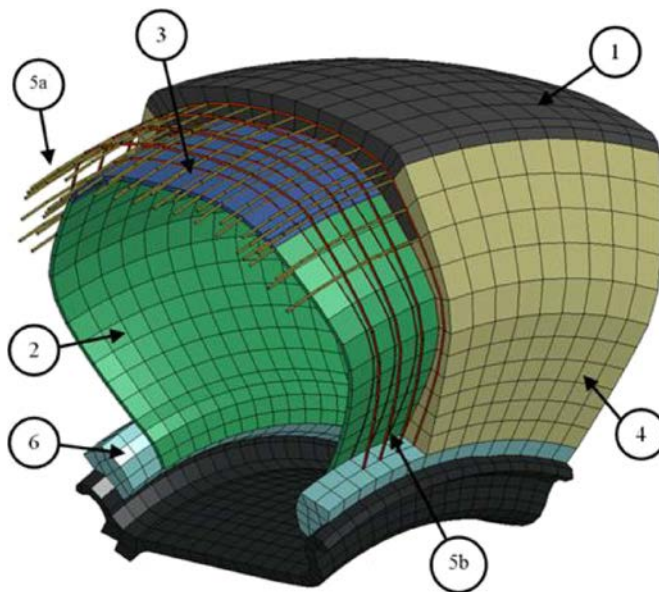


FIG. 4. FE tire model components (1. Tread, 2. Inner fabric, 3. Carcass, 4. Sidewall, 5a. Circumferential cords, 5b. Radial cords, 6. Bead core with cords) [17, 18].

In presented researches previously developed suspension system with the tire was subjected to a dynamic loading, more precisely, to pressure wave generated from the TNT explosion. Dynamic simulations were performed using the explicit LS-Dyna code using Arbitrary Lagrangian-Eulerian formulation with Jones Wilkins Lee (JWL) equation defining the explosive material [23]. Suspension system presented in Fig. 2 was modified by adding a simplified motor-car body, which simulated reflection effects of the pressure wave [17, 18]. All steel-like components were modeled using steel material with parameters taken from literature [19]. Due to the symmetric geometry of the vehicle (suspension system) only one wheel was taken into account (Fig. 5).

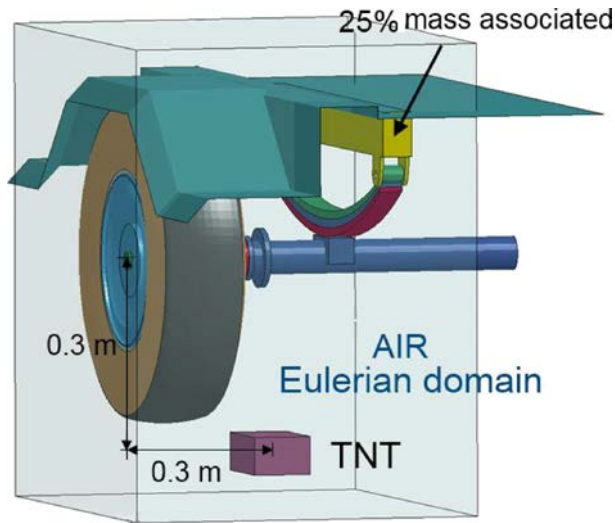


FIG. 5. Suspension system with ALE blast modeling.

Tire pressure was simulated using airbag model with Green function closed volume integration [23]. Tire destruction effect caused by the explosion was simulated using the failure criterion based on the effective strain failure variable. As stated before, in simulations authors used TNT charge with the total mass of 6.34 kg according to NATO STANAG 4569 standard. Charges were located 0.3 m under the wheel and displaced by 0.3 m towards the end of axle. Consequently, results from both analyses were compared with two described earlier constitutive tire rubber models taking into consideration.

### 3. EXPLOSION PROCESS DESCRIPTION

In presented investigations for explosion simulation the Arbitrary Lagrangian-Eulerian formulation was used, where it was necessary to define an Eulerian air

domain, in which the explosive pressure wave propagates. Additionally, on the outer walls of it a non-reflecting option was applied, which considers the flow of the pressure outside the domain. The air is considered as simple ideal gas with linear polynomial equation of state [23]:

$$(3.1) \quad p = (C_4 + C_5\mu) E,$$

where  $\mu = \rho/\rho_0$ :  $\rho$  is density,  $\rho_0$  is initial density;  $C_4$  and  $C_5$  are polynomial equation coefficients,  $E$  is internal energy.

The ALE procedure consists of two major steps: the classical Lagrangian step and the advection Eulerian step. The advection step is carried out with the assumption that nodes displacements are very small in comparison to characteristics of elements surrounding these nodes, e.g. dimensions. Moreover, in this procedure a constant topology of mesh is provided.

The governing equations for the fluid domain (Euler domain) describe the conservation of mass, momentum and energy [23]:

$$(3.2) \quad \frac{dM}{dt} = \frac{d}{dt} \int_{V(t)} \rho dV = \oint_{S(t)} \rho(\underline{w} - \underline{v}) \cdot \underline{n} dS,$$

$$(3.3) \quad \frac{dQ}{dt} = \frac{d}{dt} \int_{V(t)} \rho \underline{v} dV = \oint_{S(t)} \rho \underline{v}(\underline{w} - \underline{v}) \cdot \underline{n} dS - \int_{V(t)} \nabla p dV + \int_{V(t)} \underline{v} g dV,$$

$$(3.4) \quad \frac{dE}{dt} = \frac{d}{dt} \int_{V(t)} \rho e dV = \oint_{S(t)} \rho e(\underline{w} - \underline{v}) \cdot \underline{n} dS - \int_{S(t)} p \underline{v} \cdot \underline{n} dS + \int_{V(t)} \rho \underline{g} \cdot \underline{v} dV,$$

where  $\rho$  is fluid mass density;  $p$  is pressure;  $\underline{g}$  is acceleration of gravity;  $e$  is total specific energy. The quantities  $M$ ,  $Q$  and  $E$  are total mass, total momentum and total energy, respectively, of a control volume  $V(t)$ , bounded by a surface  $S$ , which moves in the fluid (gas-air) with arbitrary velocity  $\underline{w}$  which may be zero in Eulerian coordinates or  $\underline{v}$  in Lagrangian coordinates. The vector  $\underline{n}$  is the outwards normal to the surface  $S$ .

In both cases it was necessary to implement the detonation process of the high explosive material into the model using so called ‘‘explosive burn’’ material model. In this approach the energy of high explosive (HE) material is assumed to be suddenly released inside the front of detonation wave. Detonation process requires to model the movement of the products of detonation (PD) after they reach subsequent specific locations by the detonation wave (DW) front. Applied

explosive burn model was modelled with the JonesWilkinsLee (JWL) equation of state with the following form [23]:

$$(3.5) \quad p = A \left( 1 - \frac{\omega}{R_1 \bar{\rho}} \right) \exp(-R_1 \bar{\rho}) + B \left( 1 - \frac{\omega}{R_2 \bar{\rho}} \right) \exp(-R_2 \bar{\rho}) + \frac{\omega \bar{e}}{\bar{\rho}} \frac{dE}{dt} = \frac{d}{dt},$$

where  $\rho = \rho_{he}/\rho$  is density of products of detonation;  $e = \rho_{he}e$  is specific internal energy of PD;  $\rho_{he}$  refers to density of HE;  $p$  represents pressure of PD;  $A$ ,  $B$ ,  $R_1$ ,  $R_2$ ,  $\omega$  are empirical constants determined for the specific type of HE

**Table 1.** TNT parameters for the JWL equation of state [19, 24].

Material	$\rho$ [kg/m <sup>3</sup> ]	A [Pa]	B [Pa]	R1 [-]	R2 [-]	$\omega$ [-]
TNT	1630	3.712e+11	3.231e+9	4.150	0.900	0.3

#### 4. RUBBER CONSTITUTIVE MODELS

Two chosen constitutive materials laws which are available in LS-Dyna package were investigated: Mooney-Rivlin material model, which doesn't include strain rates and Ogden rubberlike with rate-dependency option. Both are within a large group of materials which behave differently during loading (Fig. 6) and their constitutive relationship between stress and strain is formulated by non-linear elasticity theory, called hyperelasticity [25–27].

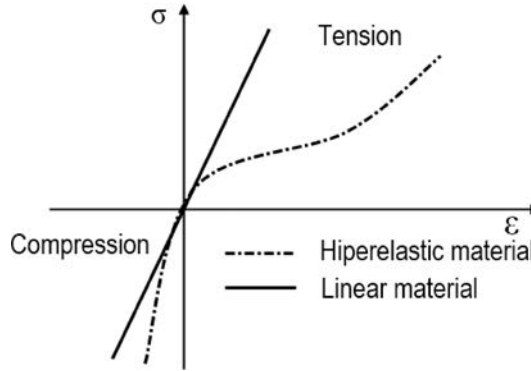


FIG. 6. Stress-strain curve for (non-linear) hyperelastic material [25].

A hyperelastic material is path independent and allows calculating the second Piola-Kirchhoff stress tensor [23, 26, 27]:

$$(4.1) \quad \mathbf{S} = 2 \frac{\partial W}{\partial \mathbf{C}},$$

where  $W = \widehat{W}(\mathbf{C})$  – is a derivative of the energy functional,  $\mathbf{C} = \mathbf{F}^T \mathbf{F}$  – is a right Cauchy-Green strain tensor ( $\mathbf{F} = \text{Grad } \mathbf{x}$ ).

In LS-Dyna two families of hyperelastic materials can be found. The first one is based on energy functional expressed in the invariants of the right Cauchy-Green tensor [23, 26, 27]:

$$(4.2) \quad W = \widehat{W}(I_1, I_2, I_3),$$

where

$$I_1 = \mathbf{1} : \mathbf{C} = \text{tr } \mathbf{C}, \quad I_2 = \frac{1}{2} (I_1^2 - \mathbf{C} : \mathbf{C}), \quad I_3 = \det \mathbf{C}.$$

Then, the derivative yields is given by [23, 26, 27]:

$$(4.3) \quad \mathbf{S} = 2 \frac{\partial W}{\partial I_1} \mathbf{1} + 2 \frac{\partial W}{\partial I_2} (I_1 \mathbf{1} - \mathbf{C}) + 2 \frac{\partial W}{\partial I_3} I_3 \mathbf{C}^{-1}.$$

The Cauchy stress  $\boldsymbol{\sigma}$  can now be obtained by  $\boldsymbol{\sigma} = J^{-1} \mathbf{F} \mathbf{S} \mathbf{F}^T$ , where  $J = \det \mathbf{F}$  is the relative volume.

The second family of hyperelastic materials is formulated in terms of principle stretch ratios. Thus, all expression should be rewritten in terms of principal stretches  $\lambda_i$ . After decomposition  $\mathbf{F} = \mathbf{R} \mathbf{U}$ ,  $\mathbf{R}$  is an orthogonal matrix  $\mathbf{R}^T \mathbf{R} = \mathbf{I}$ ,  $\mathbf{U}$  is a positive definite symmetric matrix  $\mathbf{U}^2 = \mathbf{C} \equiv \mathbf{F}^T \mathbf{F}$ , the invariants are given by:

$$(4.4) \quad \begin{aligned} I_1 &= \lambda_1^2 + \lambda_2^2 + \lambda_3^2, & I_2 &= \lambda_1^2 \lambda_2^2 + \lambda_2^2 \lambda_3^2 + \lambda_1^2 \lambda_3^2, \\ I_3 &= \lambda_1^2 \lambda_2^2 \lambda_3^2 = J^2 \end{aligned}$$

and the Cauchy stress  $\boldsymbol{\sigma}$  and the principal engineering stress  $\tau$  can be obtained from [23, 26, 27]:

$$(4.5) \quad \sigma_i = \frac{1}{\lambda_j \lambda_k} \frac{\partial W}{\partial \lambda_i} \Rightarrow \lambda_j \lambda_k \sigma_i = \tau_i = \frac{\partial W}{\partial \lambda_i}.$$

One of the most popular rubber constitutive model which is also used in presented investigations is the Mooney-Rivlin model [19, 20, 25–27]. Mathematical description of this model includes the elementary function of strain energy  $W$ , which is an elementary strain tensor function:

$$(4.6) \quad W = A(I_1 - 3) + B(I_2 - 3) + C \left( \frac{1}{I_3^2} - 1 \right) + D(I_3 - 1)^2,$$

where  $A$  ( $C_{10}$ ) and  $B$  ( $C_{01}$ ) are material parameters. The last two expressions with the parameters  $C$  and  $D$  are hydrostatic terms given by [23, 26, 27]:

$$(4.7) \quad C = 0.5A + B,$$

$$(4.8) \quad D = \frac{A(5\nu - 2) + B(11\nu - 5)}{2(1 - 2\nu)},$$

where  $\nu$  is Poisson's ratio.

The second material model used in computations is MAT Simplified Rubber, which is based on the Ogden law [7, 9, 23, 28, 29]:

$$(4.9) \quad W = \sum_{i=1}^3 \sum_{j=1}^n \frac{\mu_j}{\alpha_j} (\lambda_i^{*\alpha_j} - 1) + K(J - 1 - \ln J)$$

$$\Rightarrow \sigma_i = \sum_{p=1}^n \frac{\mu_p}{J} \left[ \lambda_i^{*\alpha_p} \sum_{k=1}^3 \frac{\lambda_k^{*\alpha_p}}{3} \right] + K \frac{J - 1}{J},$$

where  $\alpha_j$  are non-integer,  $J = \lambda_1 \lambda_2 \lambda_3$  and  $\lambda_i^* = \lambda_i J^{-1/3}$ ,  $K$  is a material parameter that controls the size enclosed by the failure surface.

In this material Ogden functional is internally determined from the uniaxial engineering stress-strain curve by defining a tabulated of the principal stretch ratio as follows [7, 9, 23, 28, 29]:

$$(4.10) \quad f(\lambda) = \sum_{p=1}^n \mu_p \lambda^{*\alpha_p} \Rightarrow \sigma_i = \frac{1}{J} \left[ f(\lambda_i) - \frac{1}{3} \sum_{j=1}^3 f(\lambda_j) \right] + K \frac{J - 1}{J}.$$

## 5. SIMULATIONS RESULTS

From the performed analyses the tire destruction and overall suspension system elements deformation were obtained. The main aforementioned objective was to compare each material behaviour during TNT explosion. Firstly, the internal energy of the tire was compared, which characteristic is presented in Fig. 7. The comparison graph of stress *versus* strain for the selected finite element (closest to the explosive charge) is presented in Fig. 8. Strain rates characteristics for both type of explosives and both materials for the same finite element of the tire are shown in Fig. 9.

It can be noticed, that for the same moment of time the tire destruction isn't identical for both material models. As expected the most devastated element of the examined suspension system is the tire, which consumes most of the explosive energy. In the Ogden rubberlike material case generated pressure wave

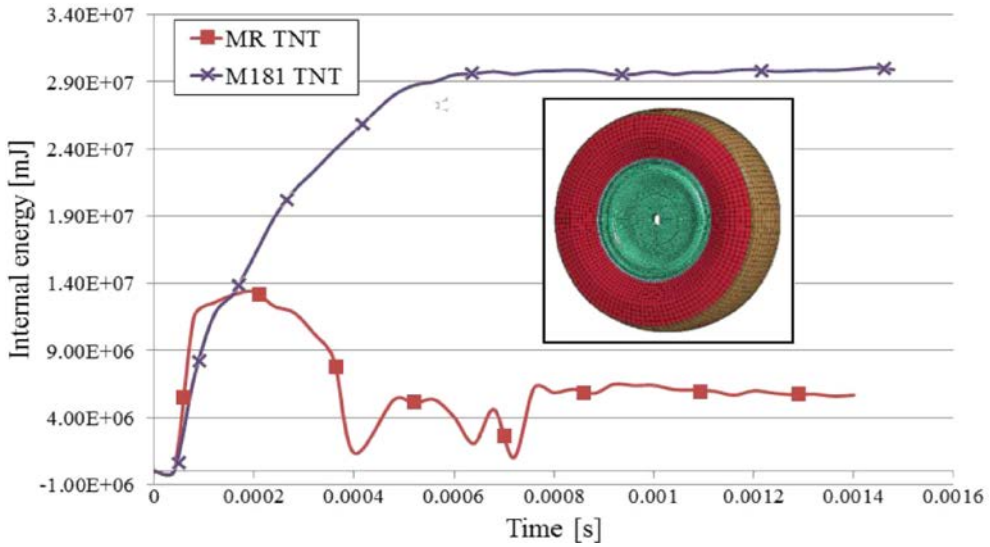


FIG. 7. Tire internal energy graph for all simulated cases.

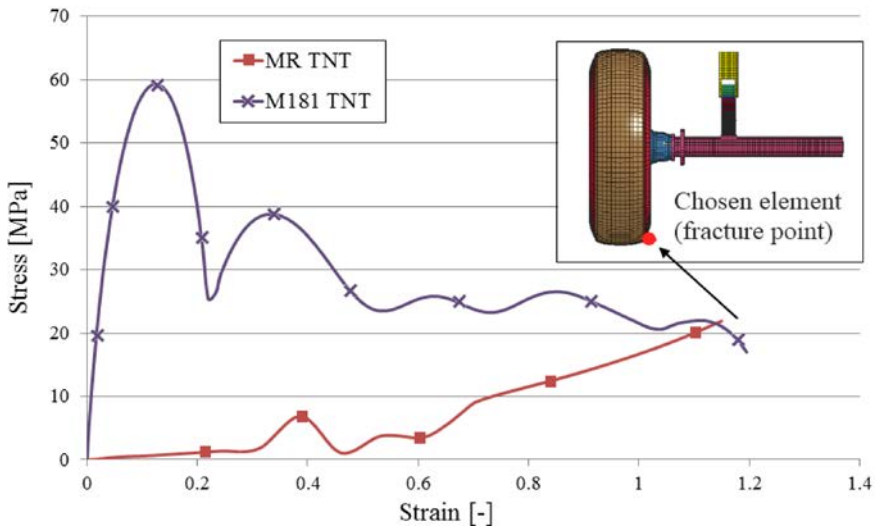


FIG. 8. Stress (equivalent) *versus* strain characteristics for all simulated cases (for selected tire element).

caused more damage to vehicle chassis elements, which means that more internal energy is absorbed by the tire what is clearly noticeable in Fig. 7. Obtained maximum energy values for Ogden rubberlike are approximately twice time bigger than for the Mooney-Rivlin material. Taking closer look at the stress (equivalent)-strain curves presented in Fig. 8 it can be also seen that maximum stress values for Ogden rubberlike are higher than for Mooney-Rivlin material

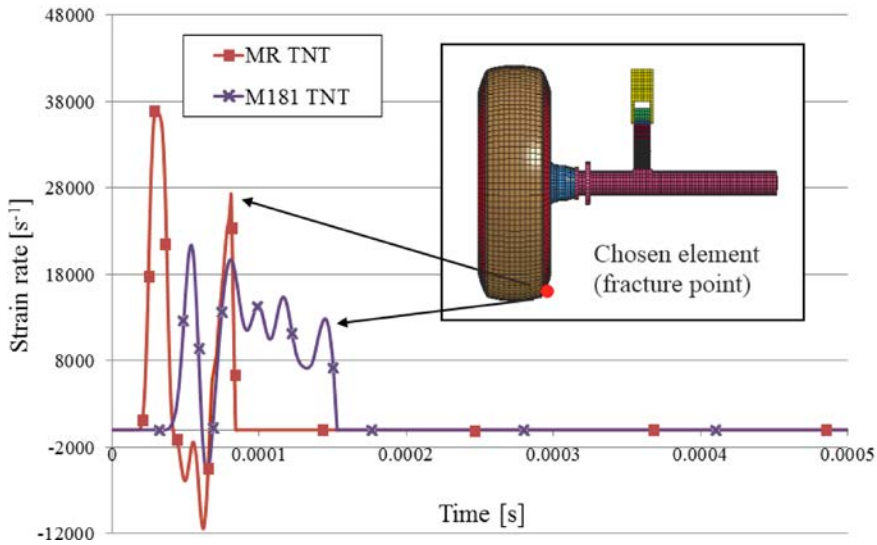


FIG. 9. Strain rate comparison for all cases (for selected tire element).

(about three times), which ideally reflects the strengthening effect presented in Fig. 1a, which indicates the strain-rate dependency not only on the element structure but also on its stresses. From the theoretical point of view it is known that the amount of absorbed energy directly depends on the stress value [23], which is very well presented in the following results for the chosen finite element. For Ogden rubberlike material equivalent stresses are higher (Fig. 8).

As mentioned before, for simulating the tire destruction effect the strain erosion criterion was applied with failure strain value of 120%. This value was obtained for both materials, however in Mooney-Rivlin material chosen element was deleted at approximately 117% strain value.

From Fig. 9 it can be seen that strain rates are different for both simulated materials. In Mooney-Rivlin case obtained maximum strain rates value was approximately  $3.8 \times 10^4 \text{ s}^{-1}$ , whereas for Ogden rubberlike it was about  $2.0 \times 10^4 \text{ s}^{-1}$ , which seems to be reliable if we take into account the results presented by other authors [3, 10–13]. This difference between rates for two materials indicates the absence of rate dependency in Mooney-Rivlin material.

## 6. CONCLUSIONS

The authors of the presented paper made an attempt of simulating a rubber structure, which in this case was the vehicle tire, under a dynamic blast wave loading. Performed analyses have completely confirmed destructive effect of the explosion under the vehicle chassis. As expected, the most devastated element

of the examined suspension system is the tire, which consumes the most of the detonation energy which results in its destruction. By implementing them into the discrete model of the investigated object a high accuracy of numerical solution is provided

Presented results shows, that by choosing the proper constitutive material for the specific phenomenon a high accuracy and reliability of numerical solution is provided. From the above results the general conclusion is that for such strongly dynamic phenomenon as blast explosion the material with rate dependency is necessity. In presented tests the authors used the strain-rate material characteristics taken from literature. Therefore, in subsequent stages the Ogden rubberlike material used in investigations will be more thoroughly tested with the particular attention pointed on its possible adoption into the vehicle tire model. Moreover, complex experimental tests of the rubber and rubber-cord composite within various loading velocities are planned, which will determine the strain rate effect on the material structure behaviour with failure process taking into account. Obtained rate dependency data will be then eventually used in final stages of carried out investigations.

#### ACKNOWLEDGMENT

The material presented in this paper has been shown at Workshop 2012 on Dynamic Behavior of Materials and Safety of Structures, Poznan, 2–4 May, 2012.

#### REFERENCES

1. OCHELSKI S., BOGUSZ P., KICZKO A., *Influence of hardness on mechanical properties of elastomers*, Journal of KONES Powertrain and Transport, **17**, 317–325, 2010.
2. KRAWCZYK A., *Mechanics of polymer and composite materials*, Science, 1985.
3. ROLAND C.M., *Mechanical behaviour of rubber at high strain rates*, Rubber Chemistry and Technology, **79**, 429–459, 2006.
4. CHEN W., LU F., FREW D.J., FORRESTAL M.J., *Dynamic compressive testing of soft materials*, Journal of Applied Mechanics, **69**, 214–223, 2002.
5. QUINTAVALLA S.J., JOHNSON S.H., *Extension of the Bergstrom-Boyce model to high strain rates*, Rubber Chemistry and Technology, **77**, 5, 972–981, 2005.
6. SONG B., CHEN W., *One-dimensional dynamic compressive behaviour of EPDM rubber*, Journal of Engineering Materials and Technology, **125**, 294–301, 2003.
7. LS-Dyna Aerospace Working Group, *Rubber Projectile Impacting a Rigid Plate*, 2012.
8. CHEN Y., ZHANG Z., WANG Y., HUA H., *Crush dynamics of square honeycomb thin rubber wall*, Thin-Walled Structures, **47**, 1447–1456, 2009.

9. DU BOIS P.A., KOLLING S., FASSNACHT S., *Material behaviour of polymers under impact loading*, International Journal of Impact Engineering, **32**, 725–740, 2006.
10. HOO FAT M.S., BEKAR I., *High-speed testing and material modelling of unfilled styrene butadiene vulcanizates at impact rates*, Journal of Materials Science, **39**, 23, 6885–6899, 2004.
11. BEKAR I., HOO FATT M.S., PADOVAN J., *Deformation and fracture of rubber under tensile impact loading*, Tire Science Technology, **30**, 45, 2002.
12. AL-MALIKY N.S., PARRY D.J., *A freely expanding ring technique for measuring the tensile properties of polymers*, Materials Science Technology, **7**, 746–752, 1996.
13. GOURDIN W.H., WEINLAND S.L., BOLING R.M., *Development of the electromagnetically launched expanding ring as a high-strain-rate test technique*, Review of Scientific Instruments, **60**, 427–432, 1989.
14. KRUSZKA L., *The study of static and dynamic properties of steel for safety and protective structures* [in Polish: *Badania eksperymentalne własności statycznych i dynamicznych stali budowlanych dla potrzeb konstrukcji ochronnych i obronnych*], Seminar Materials of Military University of Technology, 2008.
15. MORKA A., KWAŚNIEWSKI L., WEKEZER J., *Assessment of Passenger Security in Paratransit Buses*, Journal of Public Transportation, **8**, 47–63, 2005.
16. LACOME J.L., *Analysis of Mine Detonation, SPH analysis of structural response to anti-vehicles mine detonation*, LSTC, 2007.
17. BARANOWSKI P., MAŁACHOWSKI J., *Blast wave and suspension system interaction- numerical approach*, Journal of KONES Powertrain and Transport, **18**, 2, 17–24, 2011.
18. BARANOWSKI P., MAŁACHOWSKI J., NIEZGODA T., *Numerical Analysis of Vehicle Suspension System Response Subjected to Blast Wave*, Applied Mechanics and Materials, **82**, 728–733, 2011.
19. MAŁACHOWSKI J., *Modelling and research of interaction between gas and pipe structures subjected to pressure impulse* [in Polish: *Modelowanie i badania interakcji ciało stałe-gaz przy oddziaływaniu impulsu ciśnienia na elementy konstrukcji rurociągu*], BEL Studio, Warsaw, 2010.
20. NEVES R.R.V., MICHELI G.B., ALVES M., *An experimental and numerical investigation on tyre impact*, International Journal of Impact Engineering, **10**, 685–693, 2010.
21. CHO I.R., KIM K.W., JEONG H.S., *Numerical investigation of tire standing wave using 3-D patterned tire model*, Journal of Sound and Vibration, **305**, 795–807, 2007.
22. HELNWEIN P., LIU C.H., MESCHKE G., MANG H.A., *A new 3-D finite element model for cord-reinforced rubber composites- application to analysis of automobile tyres*, Finite Elements in Analysis and Design, **4**, 1–16, 1993.
23. HALLQUIST J.O., *LS-Dyna: Theoretical manual*, California Livermore Software Technology Corporation, 2003.
24. WŁODARCZYK E., *Introduction to the mechanics of explosion* [in Polish: *Wstęp do mechaniki wybuchu*], PWN, Warsaw, 1994.
25. ANSYS, *Hyperelasticity*, Structural Nonlinearities, 6, Second Edition Release 5.5, 1999.

26. MOONEY M., *A theorie of elastic deformations*, Journal of Application Physics, **11**, 582–592, 1940.
27. RIVLIN R.S., *Large elastic deformations of isotropic materials*, Philosophical Transactions of The Royal Society A, **240**, 459–490, 1948.
28. BENSON D.J., KOLLING S., DU BOIS P.A., *A simplified approach for strain-rate dependent hyperelastic materials with damage*, 9th International LS-DYNA Users Conference, **15**, 29–36, 2006.
29. OGDEN R.W., *Elastic deformations of rubberlike solids*, Mechanics of Solids, The Rodney Hill 60th Anniversary Volume, Oxford, 1982.

*Received June 5, 2012; revised version December 7, 2012.*

---

## Research on the Durability of Adhesive Composites

Marek ROŚKOWICZ<sup>1)</sup>, Tomasz SMAL<sup>2)</sup>

<sup>1)</sup> *Military University of Technology  
Institute of Air Technology*

Gen. S. Kaliskiego 2, 00-908 Warszawa, Poland  
e-mail: marek.roskowicz@wat.edu.pl

<sup>2)</sup> *The General Tadeusz Kosciuszko Military Academy of Land Forces  
Institute of Command*

Czajkowskiego 109, 51-150 Wrocław, Poland  
e-mail: t.smal@wso.wroc.pl

The paper presents research on the durability of adhesive composites, which may be used for the repair of technical objects. Durability of adhesive composites is understood in this paper as a material ability to transfer long lasting loads. Since that kind of information is not provided by manufacturers, the long-term strength and fatigue-life of selected adhesive composites are determined; especially with regard to their use in expedient (temporary) repairs of weapon systems. The results obtained show that safe values of the maximum long-term and fatigue loads of the adhesive composites investigated should be a half of the short-term strength obtained in a static tests.

**Key words:** durability of materials, adhesive composites features, long-term strength, fatigue life.

### 1. INTRODUCTION

A large number of failures in military equipment are especially visible during different kinds of combat operations. The most common battle failures of weapon systems are punctures, cracks, breaks, and lack of tightness. Any field repair actions of damaged weapon systems can be divided into two basic groups: standard (regular) repairs or expedient (temporary) repairs. Standard repairs are conducted by exchange of whole broken units or single spare parts, which are delivered by supply chains of logistic units or obtained from totally destroyed weapon systems (cannibalization). If possible, a standard repair is preferred, but it is very difficult to perform in the conditions of combat operations. An expedient (temporary) repair can be an alternative solution in many cases. An expedient repair means any improvised action which may lead to broken system being

temporarily available in order to execute a task [12, 21–23]. There are many methods that can be used to execute expedient (temporary) repairs in field conditions [11, 25], and it seems to be that adhesive materials have a great potential of providing that actions. This is caused not only by the numerous advantages of adhesive joints, but also by the increasing capacities of the particular links of the repair system, such as, reducing work consumption, enabling to perform some repairs on a lower level, no necessity to use expensive and heavy equipment, creating possibility of an available soldier and becoming independent of spare parts [23, 26]. As a result, technical objects' repairs are more and more often taking advantage of structural bonding [1, 17, 19], as well as, quick chemically setting materials; so-called adhesive composites, which create new possibilities in the scope of temporary or permanent removal of different types of damages [2, 5]. Modern adhesive composites may provide solutions to many problems, which can occur as the result of intensive exploitation of military equipment, as well as, from the influence of the enemy's munitions.

Adhesive composites applied to field repairs of weapon systems must be able to transfer great loads and create solid construction joints; therefore, it is required of them to show high cohesion and adhesion. However, the adhesive materials are characterised with relatively low durability. These materials are very sensitive to repair conditions, as well as, that they have limited shear and long-term strength – the ability to transfer constant loads in time – and limited fatigue life – the ability to transfer changing loads [5]. Without familiarity with these properties, the application of adhesive materials is burdened with the risk of re-damage in a relatively short time after the performed repair.

## 2. METHODOLOGY OF RESEARCH

Currently, a wide range of specialist adhesives for different purposes is produced. There are many products of numerous companies, but taking the specificity of field repairs into account, it seems that the most useful are composites fulfilling the requirements of multi-purpose materials as “super metals” and those of the quick-setting “rapid” type [2, 24]. Therefore, the main objects of research are well-known and available in the Polish adhesive composites market of Belzona, Unirep and Chester Metal.

Application of adhesive composites to repairs requires, among others, determining their durability, which is broadly understood as a material ability to transfer long-lasting static load (static long-term strength) and their durability to changing load (fatigue life). Since that information is not provided by the manufacturers, the main aim of the work is to determine the aforementioned features of selected adhesive composites with regard to their use in expedient (temporary) repairs of technical objects.

Numerous experimental investigations were conducted in order to execute the planned research, in which specimens of the examined adhesive composites were used to determine their mechanical properties. Bonded specimens were used in order to determine the strength of joints made with the examined materials. It was decided to elaborate the results of experimental investigations with statistical methods. The arithmetic mean and the standard error of the mean value were calculated according to the following formulas [8]:

$$(2.1) \quad \bar{x} = \frac{\sum_{i=1}^n x_i}{n},$$

$$(2.2) \quad \bar{S} = \sqrt{\frac{\sum_{i=1}^n (x_i - \bar{x})^2}{n - 1}},$$

where  $n$  is the number of specimens in a lot;  $x_i$  is the measured result for  $i$  of that specimen; and  $\bar{x}$  is the arithmetic mean of  $n$  results.

Since  $n < 30$ , the confidence interval was defined by means of the Student-Fischer method for a confidence level of  $1 - \alpha = 0.95$ :

$$(2.3) \quad \left( \bar{x} - \frac{t_\alpha \bar{S}}{\sqrt{n(n-1)}}; \quad \bar{x} + \frac{t_\alpha \bar{S}}{\sqrt{n(n-1)}} \right),$$

where  $t_\alpha$  is a number satisfying the relation

$$(2.4) \quad P(|T_{n-1}| \geq t_\alpha) = \alpha$$

in which  $T_{n-1}$  means a random variable of a  $T$ -Student distribution of  $n-1$  degrees of freedom.

### 2.1. Methodology of research on long-term strength

The research on static long-term strength is aimed at an estimation of the permissible value of loads, for which constant influence does not cause damage to adhesive joints for at least 500 hours at a temperature of 60°C. The operation time of a joint was assumed by considering the temporary nature of expedient repairs. The temperature was assumed by taking into consideration the possibility of the heating up of military equipment exposed to sunlight, as well as the possibility of repairing elements heating up during operation; i.e. engine blocks, with adhesive materials [16].

The research on long-term strength was executed with three simultaneous stages. The first stage consisted in determining the specimens strains loaded

at increasing temperature (creep curves). In order to determine creep curves, specially designed and executed devices were used in which the specimens were loaded with compression coil springs. The characteristics of the springs used were linear; therefore, the load on the specimen could be selected (with the sufficient accuracy) on the basis of measurement of spring deflection [13]. The measurement of strain values of the examined specimens was conducted by means of a mechanical micrometric sensor mounted to the moving component of the device. The device together with the specimen was placed into a temperature chamber (Fig. 1). Subsequently, the strain value of the examined adhesives was noted at the specific time intervals. The research was continued until the increase of strain stopped, or until the strain increase became negligible. The specimens used to determine creep curves were made in the form of a cylinder of 12.5 mm diameter and 25 mm length (Fig. 2a).



FIG. 1. View of the device used to determine creep curves with mounted and loaded specimens.

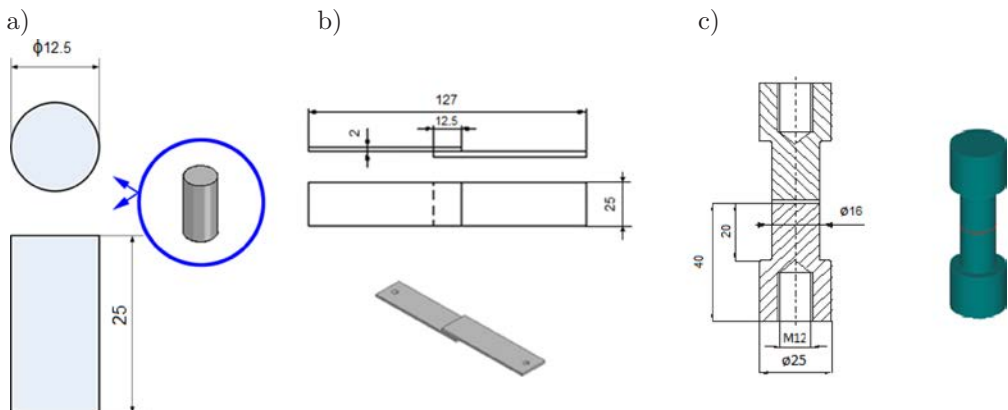


FIG. 2. Shape and dimensions of specimens used to determine properties of adhesive composites.

The subsequent stage of research allowed determination of the shear strength of adhesive composites joints. The determined strength was the basis for load selection to long-term tests. In order to determine shear strength, single-lap joints were used (Fig. 2b), which were made of S235Jr steel. The tests were conducted according to PN-EN 2243-1:1999, with use of a ZD-10 testing machine [14].

The last stage of research defined static long-term strength of the examined adhesive composites. The measured value was the time needed to destroy the joint subjected to certain load with increasing temperature. These tests were conducted by means of devices designed by ROŚKOWICZ [13] (Fig. 3).

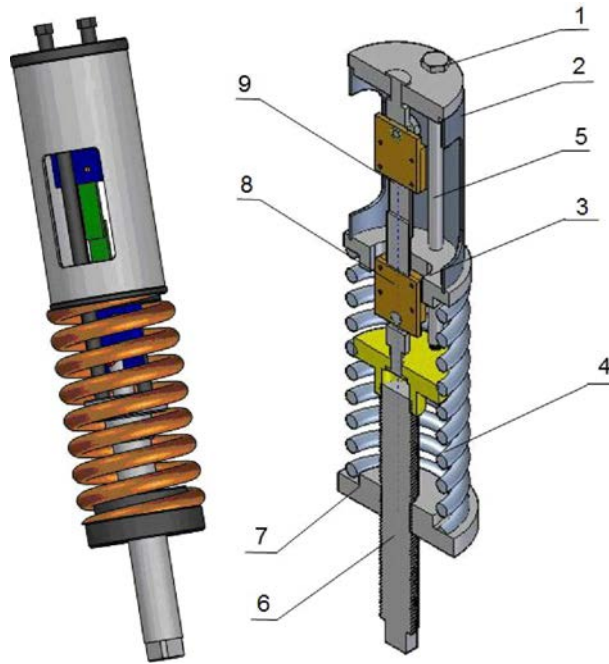


FIG. 3. The device used to determine static long-term strength of adhesive joints: 1, 3 – covers; 2 – spacing sleeve; 4 – spring; 5 – lock screws; 6 – screw tightening the spring; 7 – resistance sleeve; 8, 10 – grips for specimen mounting; 9 – tested specimen [13].

The function of these devices was to apply the required constant load to the lap specimen bonded with the adhesive composite. The research involved simultaneously five devices, which were placed in a KC 100/200 thermal chamber of the EL-CON company (Fig. 4).

The load was imposed – similarly to determining of creep curves – by the spring compression of a value defined with a characteristic of each spring used (Fig. 5). Specimens were kept in the assumed temperature under constant load until their destruction. The particular time was measured to the specimen's destruction. The applied load caused normal negative stress in the specimen of



FIG. 4. The view of devices together with the mounted and loaded specimens used to determine long-term strength of adhesive joints.

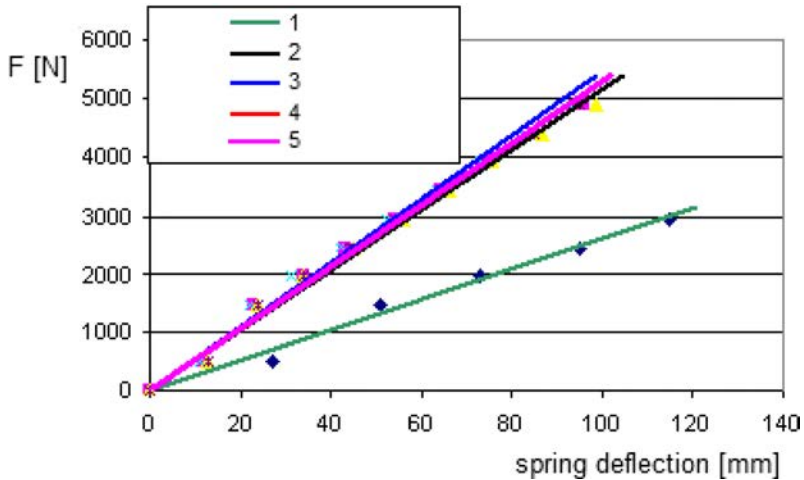


FIG. 5. Characteristics of the springs used in devices with the imposed loads.

30 MPa. The value of stress was selected on the basis of a compromise between the dimensions of the measuring devices (these were designed in such a way that it was possible to place them all in a thermal chamber at the same time) and the value of the load, with which the phenomenon of creep shows itself. The value of the load was in the range of 30–50% of the shear strength of the adhesive composites.

## *2.2. Methodology of research on fatigue life*

The research on fatigue life of adhesive composites made it possible to estimate the permissible loads of joints loaded with changing forces. Thanks to the repeated experimental investigations, the conditions of the experiment were selected: frequency of loads, type of load cycle, value of the maximum load of cycle, and the types of specimen used in the research. With regard to the temporarily nature of field repairs of weapon systems, the fatigue life tests were terminated after 250,000 load cycles. In the first step, specimens used were those presented in Fig. 2a. In the research, adhesives composites of the “super metal” group were loaded with zero-start pulsating compression stresses of 55 MPa, that is, equal to a half of their compression strength. The adhesive composites of the “rapid” group were loaded in fatigue tests with zero-start pulsating compression stresses of 28.5 MPa, and that is a half of compression strength of the material of the lowest strength [5]. The tests were performed on an Instron 8501 testing machine with a frequency of 20 Hz.

Further research on fatigue life was carried out for adhesive joints with use of tensile loaded cylindrical specimens (Fig. 2c). The elements of these specimens were made with a 2024TR aluminium alloy. The method of preparing the specimens' surface for bonding was by sand blasting using aloxite, followed by cleaning with extraction petrol. The specimens were subsequently evaporated in a laboratory dryer at 60°C for ten minutes. In this fatigue test, the chosen adhesive composites were loaded with zero-start pulsating compression stresses of 55 MPa. The tests were performed on an Instron 8501 testing machine with a frequency of 20 Hz. The research concerned adhesive composites whose destruction in static tests was typically cohesive [7]. This was done in order to find out what would be the destruction of joints made of this material in a fatigue test, and whether its fatigue life would be longer than that of joints undergoing adhesive destruction, e.g. those made of Epidian 57/Zl. Apart from that, a correlation was sought between the fatigue life of the materials themselves and the joints made of them.

Subsequently, the materials were subjected to a fatigue life test in lap joints (Fig. 2b). The specimens were loaded with zero-start pulsating shear stresses in the range from 0.1–1.5 kN, that is, about a half of the shear stress. The tests were performed on an Instron 8501 testing machine with a frequency of 20 Hz.

## 3. RESEARCH ON THE DURABILITY OF ADHESIVE COMPOSITES

### *3.1. Long-term strength*

In the literature there are no all-purpose prognostic methods concerning long-term strength that can be applied in practice. Searching for a direct relation

between the short-term and long-term strength of adhesive composites is fallible. The example can be the research results presented in the information material [4], where long-term strength of Araldit AV 138 adhesive in 10000 h test is 75% of the short-term strength and for Araldit AW 106 adhesive it is only 25%.

The manufacturers of adhesives hardly ever define durability of their products to long-term loads. A credible method of determining the longterm strength of adhesive joints is by conducting an experimental analysis; and still, it involves considerable cost and time-consuming research [10, 13, 18].

It was decided to estimate the permissible values of loads of the adhesive composites with regard to their static long-term strength. On the basis of the methodology used in the work [13], creep curves for the selected adhesive composites were determined. On the basis of previous research it seemed that ambient temperature was too low to gain high long-term strength of adhesive composites made of epoxy resins [14]. Therefore, the curing process was carried out by a single stage (at ambient temperature) and by a double stage (at increased temperature) in order to define the influence of curing conditions of adhesive composites on their long term strength [15]. It seems that this state of facts is related to a level of cross-linking of an adhesive. The adhesive cured in the increased temperature is characterized by a higher level of cross-linking, and therefore, it has got different physics and mechanical properties. The research showed that some adhesive composites were characterized by a rapid increase in strains in the increased temperature that caused permanent deformations or destruction of the examined specimen within several or several dozen minutes (Fig. 6). Therefore, these materials were excluded from the further examination.

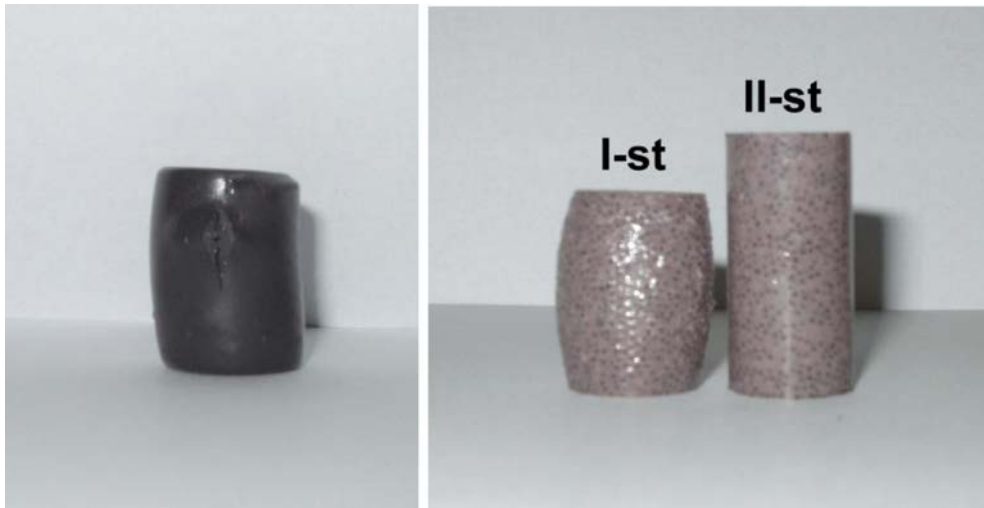


FIG. 6. Unirep 1 and Belzona 1812 (after single-stage stage curing) adhesive composites after a few minutes from the moment of 30 MPa load at a temperature of 60°C.

Creep curves for other materials were presented in Fig. 7. For the purposes of comparative analysis, the creep curves for an adhesive based on physically unmodified epoxy resin Epidian 57 were also plotted on the graph. From among the adhesive composites discussed, the least increase in deformation was visible for Belzona 1812 (double-stage curing) adhesive composite. Unirep 3 and Belzona 1111 also had a good resistance to creep, whereas Epidian 57 had a rather bad resistance.

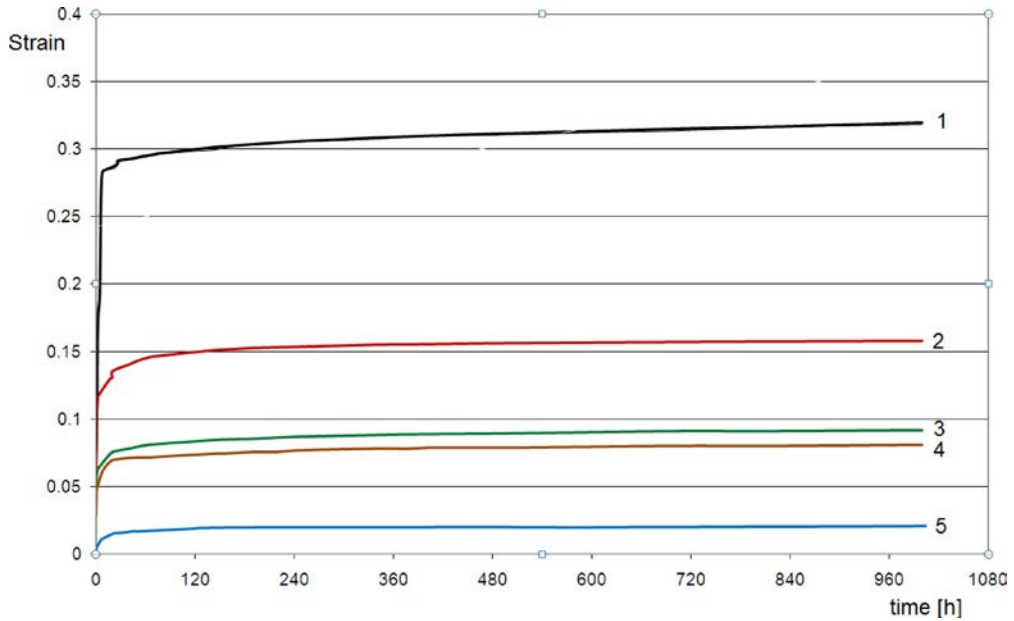


FIG. 7. Creep curves of the adhesive composites in the temperature of  $60^{\circ}\text{C}$  with load causing normal stresses of 30 MPa in the examined specimens (1 – Epidian 57, 2 – Chester Metal Super, 3 – Belzona 1111, 4 – Unirep 3, 5 – Belzona 1812 – II st.).

Subsequently, the long-term strength of adhesive composites was determined. The measure of long-term durability was the lapse of time between the commencement of the experiment and specimen destruction. With regard to the assumed expediency of repairs, 500 hours was the given maximum time of a test. The research was conducted in temperatures of  $60$ ,  $80$  and  $100^{\circ}\text{C}$  taking the possible operational temperature of the repaired elements under consideration. The research results are presented in a form of column charts where time of the certain specimen destruction was marked.

Joints made of Belzona 1111, Chester Metal Super, Unirep 3, and double-stage cured Belzona 1812 were characterized with a durability of 500 h at a temperature of  $60^{\circ}\text{C}$  (none of the examined specimen were destroyed); see Fig. 8.

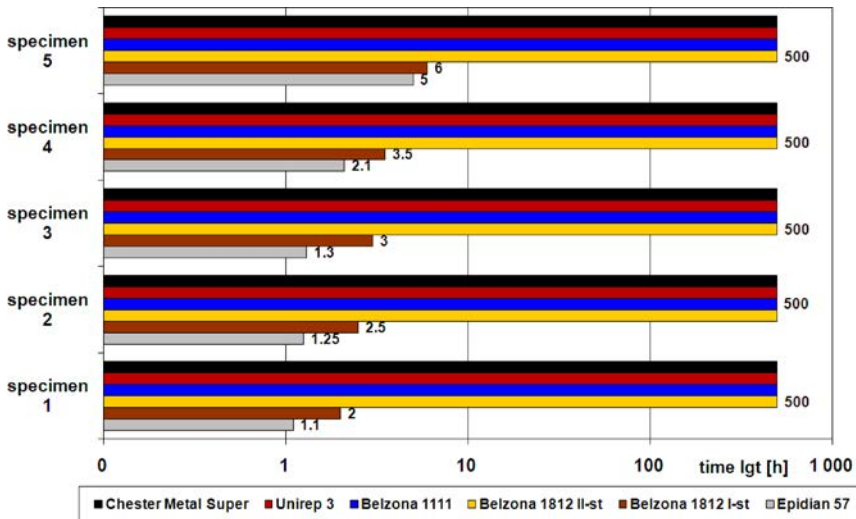


FIG. 8. Static long-term strength of lap joints made of adhesive composites (loaded with a power of 60%  $F_n$  and at a temperature of 60°C).

It was stated that even a preliminary estimation of adhesive creep curve shapes (Fig. 7) enabled the prediction of their ability to transfer long-term loads (Fig. 8), since there is a clear relation between the nature of a composite's creep curve and its ability to long-term load transfer in adhesive joints. Since the durability of adhesive joints did not change considerably at a temperature of 80°C, further research was conducted in temperature increased to 100°C (Fig. 9).

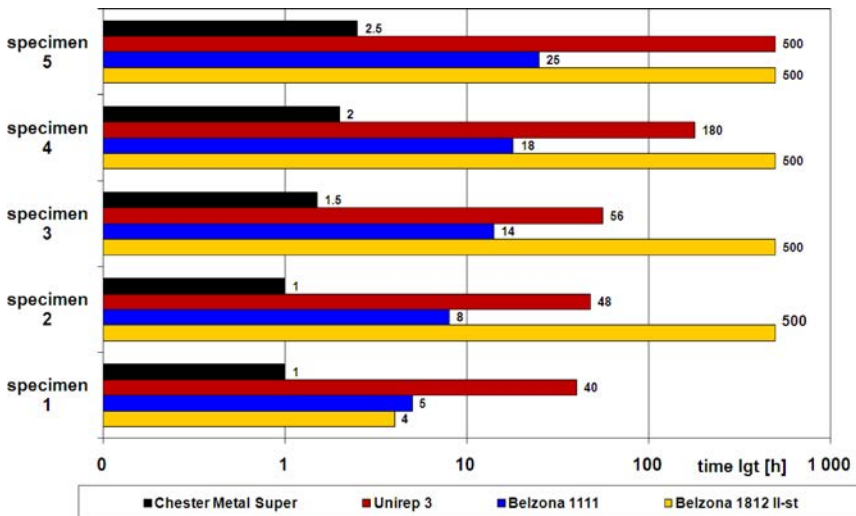


FIG. 9. Static long-term strength of lap joints made of the adhesive composites (load with power of 60%  $F_n$  and temperature of 100°C).

At a temperature of 100°C, most of the examined specimens were destroyed before the assumed time of 500 h passed. The specimens first destroyed were made of Chester Metal Super. Specimens made of Belzona 1111 were destroyed within the first day and night. Better durability was shown by specimens made of Unirep 3, since it lasted from several dozen to several hundred hours; and one of the examined specimens was not destroyed within the assumed 500 h. The best durability was shown by specimens made of double-stage cured Belzona 1812, which is the material designed for operation at increased temperature. However, specimen one showed considerably worse durability than the rest of them. This was probably caused by some fault in the preparation of the specimen (e.g. air bubble inside).

The conducted research proved the thesis that the shortterm strength of adhesives cannot be the only criterion of its usefulness in executing repairs in crucial structures which will have to operate at an increased temperature for quite a long time. On their basis it is hard to find an unambiguous quantitative correlation between creep curves determined for the adhesive composite itself (treated as a material) and the durability of adhesive bonds. Still, one can attempt to give some rough interpretation of this relation and state that if strain of adhesive composite subjected to load at increased temperature (in this case 60°C) does not exceed 20% of specimen's dimension in the assumed time, joints made of this composite should be characterized by durability of approximately 500 h for loads that are equal to a half of the short-term strength (in case of the research conducted here, that was 60% of the shear strength). Moreover, creep curves are valuable sources of information concerning conditions (and especially thermal conditions) in which an adhesive joint can be used for a long time. An example here can be the relation  $\varepsilon = f(t)$ , gained for Epidian 57, where the adhesive showed low durability in joints with great strain caused by creep.

### 3.2. *Fatigue life*

The research on fatigue life of different adhesive joints [1, 3, 9] has shown that fatigue life of these types of joints is much less considerable than their short-term strength. Predicting the fatigue life of adhesive joints is a complicated issue and requires numerous tests [5]. However, using adhesives for the repair of technical objects, one should take the possibility of fatigue loads under consideration. A lot of research has proven that fatigue life of adhesive joints is actually dependent on the maximum reduced stresses present in bonding with the maximum value of load of the fatigue cycle. This thesis has been proven true in the research, which compared the fatigue lives of joints that differed considerably from each other in shape and load method, and which had similar adhesive bonds – the same type of adhesive, identical method of adhesive surface preparation, and similar thickness of bonding (Fig. 10).

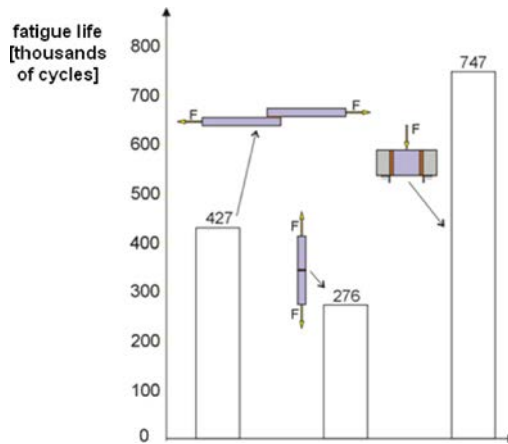


FIG. 10. Influence of the specimen's shape and load method on the average fatigue life of joints made of epoxy adhesive Epidian 57/Z1 [5].

During research on fatigue life the adhesive composites of the “super metal” group were loaded with zero-start pulsating compression stresses of 55 MPa, that is, equal to a half of compression strength. The research on Belzona 1111 and Unirep 3 was terminated after approximately 750,000 cycles. Specimens made of Chester Metal Super material were destructed after a min. of 2,785 and max. of 21,950 cycles (Fig. 11). The short fatigue life of Chester Metal Super adhesive composite has been confirmed by similar research, in which fatigue life was determined for slightly longer cylinder specimens of the same diameter ( $l = 31.5$  and  $\phi = 12.6$ ) with a zero-start pulsating load of 56 MPa at a frequency of 10 Hz. While Belzona 1111 and Unirep 3 adhesive composites reached the assumed value of fatigue life of 100,000 cycles, specimens made of Chester Metal Super composites were destroyed after 2,600 cycles on average [20].

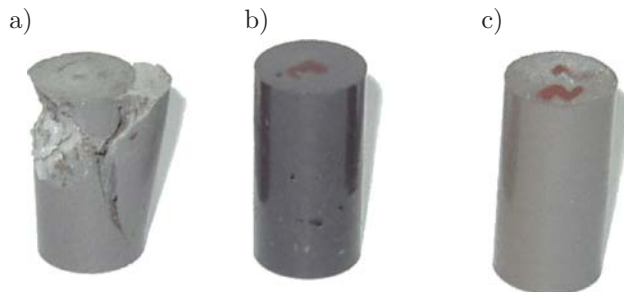


FIG. 11. View of specimens after fatigue tests: a) Chester Metal Super, b) Unirep 3, c) Belzona 1111.

The adhesive composites of the “rapid” group were loaded in fatigue tests with zero-start pulsating compression stresses of 28.5 MPa, that is, a half of the compression strength of adhesive composites of the lowest strength. After 1,483

cycles, the Unirep 1 specimen was subject to permanent deformation. The other was not destroyed after they were loaded by an approximate number of cycles of 1,000,000. The experiment was terminated and the load was increased to 41 MPa, that is, approximately 0.57 of the compression strength of Belzona 1221 and approximately 0.43 of Chester Metal Rapid. The Belzona 1221 specimen deformed plastically after 8,634 load cycles. The Chester Metal Rapid specimen transferred 210,110 load cycles without destruction (Fig. 12).



FIG. 12. View of specimens after fatigue tests: a) Chester Metal Rapid, b) Unirep 1, and c) Belzona 1221.

The research conducted here showed that the Chester Metal Super composite was characterized with a definite shorter fatigue life in comparison to the other materials examined in this group, while the longest fatigue life from the “rapid group” had a Chester Metal Rapid composite; and that is comparable to materials of “super metals” group (Fig. 13).

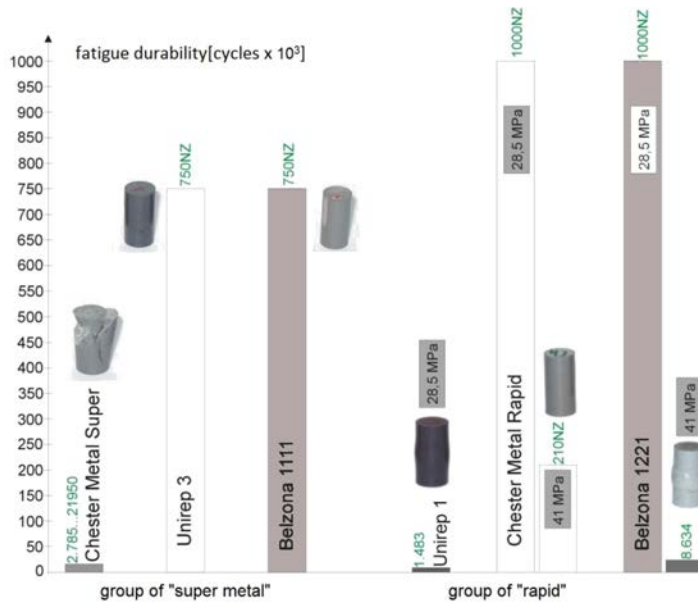


FIG. 13. Fatigue life of the adhesive composites examined (NZ – specimen was not damaged during the test).

Further research on fatigue life was carried out for adhesive joints made of the selected adhesive composites using tensile loaded cylindrical specimens (Fig. 2c). During the research destruction of the cohesive type was noticed in the case of every examined specimen made of Belzona 1111. What is more, it was stated that the examined composite was characterized by longer fatigue life in comparison with Epidian 57/Z1 subject to adhesive destruction. The examined joints made of Chester Metal Super composite showed long fatigue life, despite the fact that Chester Metal Super itself is characterized by a short fatigue life, and that that indicates no correlation between the fatigue life of the adhesive composite itself and tensile loaded bonds made with them. The most probable reason for this state of fact is the relatively high stress-strain strength of this material [6]. The research conducted also showed that the fatigue life of the Chester Metal Super composite examined in bonds was rapidly decreasing with an increase of the maximum load of a fatigue cycle from approximately 05 to approximately 06 of the short-term strength. The Chester Metal Rapid composite showed in this test a shorter average fatigue life of joints in relation to the composites of the “super metal” group, that is, Belzona 1111 and Chester Metal Super. This fact was probably caused by adhesive destruction of joints.

Subsequently, the materials discussed were subjected to a fatigue life test in lap joints (Fig. 2b). The tests were executed in two stages. In the first stage the absolute shear fatigue life was determined, since the adhesive composites investigated were subjected to the same load of 13 kN. In the second stage the adhesive composites were subjected to different loads that had value of  $0.66F_n$ . As a result, a relative shear fatigue life was determined. The fatigue life of Belzona 1111 turned out in single lap joints to be longer than that of Chester Metal Super; contrary to the situation with tensile loaded joints. In the Fig. 14 fatigue lives of specimens loaded with identical cycles and joined with different adhesive composites are compared.

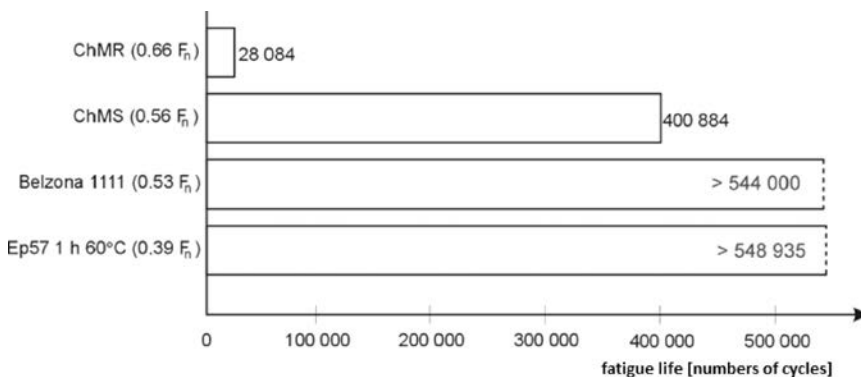


FIG. 14. Comparison of the absolute shear fatigue life of adhesive composites (the maximum load of a fatigue cycle was 1.3 kN for all adhesives).

The shortest fatigue life was visible for specimens joined with Chester Metal Rapid; and still, their relative load was the greatest. Belzona 1111 and Epidian 57/Z1 showed a long absolute fatigue life with the applied load.

The relative fatigue life of specimens joined with Belzona 1111 turned out to be longer than that of specimens joined with Epidian 57/Z1. It was stated that fatigue load of joints made with Chester Metal Rapid and Epidian 57/Z1 at the level of 066 of shear strength was unacceptable with regard to low durability of joints loaded in this way (Fig. 15).

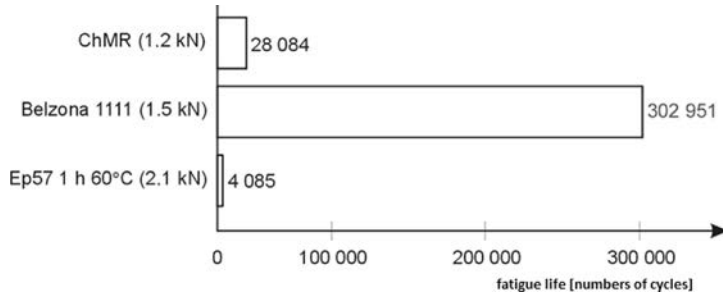


FIG. 15. Comparison of the relative shear fatigue life of adhesive composites (the maximum load of fatigue cycle was  $\sim 0.66F_n$ ).

During the fatigue tests, the strains of adhesive composites were determined which were exemplified by cylinder specimens cast from the examined adhesive composite (Fig. 2a). The specimens were subjected to compression stress for which the maximum load of fatigue life was  $\sim 0.5$  of short-term compression strength. A position of the moving traverse of testing machine was measured after every thousand cycles. The conducted test allowed for the determination of the strain amplitude of the samples, as well as the change in height resulting from movement of the traverse. The exemplary result of this research is presented in Fig. 16.

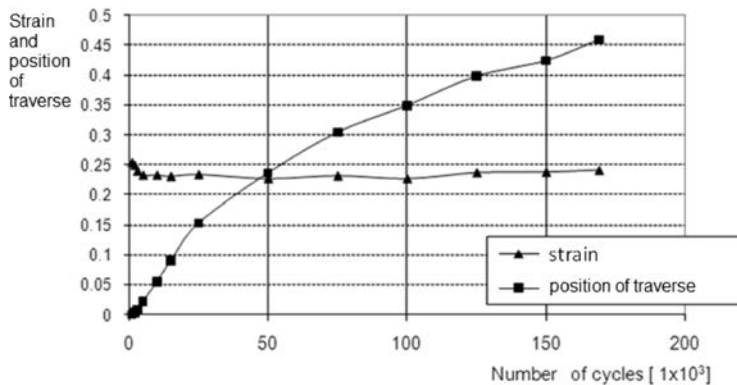


FIG. 16. Change of specimen's strain and position of the traverse (change in specimen's height) during fatigue tests of Belzona 1111 adhesive composite.

It was noticed that after several thousand load cycles, the strain amplitude of the specimen was defined on practically a constant level. Simultaneously, a constant increase of permanent strain of the examined specimen was noticed (by a decrease in height). The nature of the observed strains explicitly shows that the examined material was subject to creep (cf. Fig. 7).

#### 4. CONCLUSION

On the basis of the research presented here, the following conclusions can be drawn:

- There is a quality relation between the nature of the creep curve of the composite itself and the durability of joints made with this composite. The composites, after being loaded at an increased temperature, showed greater initial strains and a greater gradient of increase in strains in time, also showed lower durability at increased temperature (from several to several dozen hours).
- On the basis of the tests conducted so far, it is hard to find a direct quantitative correlation between creep curves and the analysed strength of adhesive bonds. Still, it can be stated that if strains of adhesive joints subjected to loads at an increased temperature (in this case  $60^{\circ}\text{C}$ ) do not exceed 10% within several hundred hours, then the joints of this adhesive composite should show at least 500 h durability at a temperature of up to  $80^{\circ}\text{C}$  with load that is equal to a half of short-term strength in ambient temperature.
- It was stated that for a specific level of loads of adhesive joints (in this case it is 60% of the short-term strength), there is a temperature value near to which the durability of shear loaded bonds is rapidly decreasing. For bonds made of adhesive composites that was at a temperature of  $100^{\circ}\text{C}$ .
- The temperature and time of adhesive composites' curing have a significant influence not only on shortterm strength of adhesive composites, but also on their durability. The increased temperature increases the extent of cross-linking of epoxy matrix; thanks to which the material is more resistant to creep at an increased temperature.
- Fatigue destruction of adhesive bonds can be of an adhesive or cohesive nature, and a longer fatigue life is shown by bonds which undergo cohesive damage during shortterm strength tests. On the other hand, a fatigue life of composite adhesive bonds cannot be predicted on the basis of fatigue life of these materials themselves.
- Both long term strength and fatigue life of adhesive joints made with the use of adhesive composites can be rapidly reduced with a slight increase of their load.

- It seems that, in the mechanism of fatigue destruction of adhesive joints, the process of adhesive material creep is of great significance since, as it has been proved, this occurs even at ambient temperature.
- Value of adhesion's forces has a considerable influence on the short-term strength of adhesive joints, and has a less considerable influence on their fatigue life. Therefore, using procedures that increase the strength of adhesive joints is always advisable; and yet, one should bear in mind that it will not have directly proportional influence on their fatigue life.
- With regard to the requirements of expedient (temporary) repairs executed in field conditions, the long-term strength of adhesive joints longer than 50 hours and a fatigue life of adhesive joints higher than 100,000 cycles, can be accepted as sufficient in most cases. Therefore, a safe value for the maximum long-lasting and fatigue loads of the adhesive composites investigated that ensures the required durability of joints made of these composites should be 0.5 of the short-term strength.

## REFERENCES

1. BAKER A.A., *Bonded composite repair of fatigue-cracked primary aircraft structure*, Comp. Struct., **47**, 431–443, ISSN 0263-8223, 1999.
2. CYPKO E., KOWALCZYK S., RACZKOWSKI D., *Repair of military equipment by application of quick-setting adhesives* [in Polish], General Staff of The Polish Armed Forces, Warsaw, 1998.
3. CLARK G., *Failures in military aircraft*, Engineering Failure Analysis, **12**, 755–771, ISSN 1350-6307, 2005.
4. Information Materials of Ciba-Geigy, *Araldite, Structural Adhesives Supplied by CIBA-GEIGY*, 1988.
5. GODZIMIRSKI J., ROŚKOWICZ M., TKACZUK S., SMAL T., *Epoxy adhesives. An application in repairs of machines and equipment* [in Polish], WNT, Warsaw, ISBN 978-83-204-3605-1, 2010.
6. GODZIMIRSKI J., SMAL T., *Possibilities of adhesive joints executing with use of composite adhesives* [in Polish], Technology and Assembly Automation, **3**, 29, 18–23, ISSN 1230-7661, 2000.
7. GODZIMIRSKI J., KOMOREK A., SMAL T., *Research of strength features of adhesive composites* [in Polish], Maintenance Problems of Machines, **1**, 64, 157–165, ISSN 1232-9312, 2007.
8. ZACHARSKI J., *Probability and mathematical statistics in tasks* [in Polish], The Military University of Technology, Warsaw, 1974.
9. KLUG J.C., MALEY S., SUN C.T., *Characterization of fatigue behavior of bonded composite repairs*, Journal of Aircraft, **36**, 6, 1016–22, ISSN 0021-8669, 1999.
10. FERRY J.D., *Viscoelastic Properties of Polymers*, John Wiley and Sons, New York [polish translation WNT 1965], 1961.

11. REES K., SHAMES J., HORN R., ESSWEIN L., *Current Procedures for Assessment of BDR in Helicopters*, NATO Research and Technology Organisation, RTO-EN-AVT-156, 7/1-27, ISBN 978-92-837-0119-4, 2010.
12. UPDAHYA K.S., SRINIVASAN N.K.A., *A simulation model for availability under battlefield conditions*, Journal of Simulation, **74**, 6, 332–339, ISSN 1747-7778, 2000.
13. ROŚKOWICZ M., *Long-lasting strength of adhesive bonds* [in Polish], Doctor's Thesis, Military Academy of Technology, Warsaw, 2004.
14. ROŚKOWICZ M., SMAL T., *Modification influence of adhesive layer on static long-lasting life of adhesive joint* [in Polish], Technology and Assembly Automation, **2**, 52, 51–54, ISSN 1230-7661, 2006.
15. ROŚKOWICZ M., SMAL T., *Determination of creep curves and long-term strength of adhesive joints* [in Polish], Technology and Assembly Automation, **2**, 3 56, 57, 120–123, ISSN 1230-7661, 2007.
16. ROŚKOWICZ M., SMAL T., *Durability of the Belzona 1111 and the Belzona 1812 Adhesive Composites*, Polymers, **6**, 471–477, ISSN 0032-2725, 2011.
17. DAVIS M.J., *The role of materials and processes in defective bonded structural repairs*, Proceedings of 41st, International Conference SAMPE, Anaheim, 936–50, 1996.
18. MESHGINA P., CHOIB K.K., REDA TAHA M.M., *Experimental and analytical investigations of creep of epoxy adhesive at the concrete – FRP interfaces*, International Journal of Adhesion and Adhesives, **29**, ISSN 0143-7496, 2009.
19. CHESTER R.J., WALKER K.F., CHALKEY P.D., *Adhesively bonded repairs to primary aircraft structure*, Int. J. of Adhesion and Adhesives, **19**, ISSN 0143-7496, 1999.
20. KOWALCZYK S., SMAL T., *Changes in the properties of composite materials and their relation to the technology of regeneration and repair of machines and equipment* [in Polish], Maintenance Problems, **3**, 26, 181–189, ISSN 1232-9312, 1997.
21. STANAG 2418, *Procedures for expedient repair, including battle damage repair*, 2009.
22. SMAL T., *Battle damage repair of military equipment with use of adhesive composites* [in Polish], [in:] *The problems of Armament and Military Equipment Service* [in Polish], The Gen. T. Kosciuszko Military Academy of Land Forces, Wrocław, 205–210, ISBN 13/978-83-87384-03-6, 2006.
23. SMAL T., *Battle damage repair systems in selected NATO armies*, [in:] *Deterioration, Dependability, Diagnostics*, University of Defense, Brno, 33–40, ISBN 978-80-260-0633-6, 2011.
24. SMAL T., ROŚKOWICZ M., *The battlefield maintenance of aircraft equipment* [in Polish], Quarterly Bellona, **4**, 659, 170–175, ISSN 1897-7065, 2009.
25. SMAL T., FURCH J., *Expedient Repairs – Analysis of Possibilities and Needs*, Advanced in Military Technology, **4**, ISSN 1802-2308, 2011.
26. MARIOLI-RIGA Z.P., TSAMASPHYROS G.J., KANDERAKIS G.N., *Design of emergency aircraft repairs using composite patches*, Mechanics of Composite Materials and Structures, **8**, 199–204, ISSN 1075-9417, 2001.

*Received September 4, 2012; revised version December 4, 2012.*

---

## An Experimental Investigation and Modelling of Friction Stir Processing

Marek Stanisław WĘGŁOWSKI<sup>1)</sup>, Carter Benjamin HAMILTON<sup>2)</sup>

<sup>1)</sup> *Institute of Welding (Instytut Spawalnictwa)*  
Błogosławionego Czesława 16-18, 44-100 Gliwice, Poland  
e-mail: marek.weglowski@is.gliwice.pl

<sup>2)</sup> *Miami University, School of Engineering and Applied Science*  
Oxford 45056, Ohio, USA

In this paper experimental and numerical modelling of the Friction Stir Processing technique are presented. The experiments were carried out on cast aluminium alloy AlSi9Mg. A conventional tool without a pin was used. During the trials, the tool temperature, torque and forces acting on the tool were measured. The results revealed that an increase in the rotational speed caused an increase in the temperature and a decrease in the torque. Furthermore, the increase in travelling speed caused a decrease in the tool temperature and an increase in the torque. The experimental results were compared with that achieved based on the numerical modelling.

**Key words:** Friction Stir Processing, aluminium alloys, modelling.

### 1. INTRODUCTION

Friction Stir Processing (FSP), based on the stir of material, utilizes the same process principles as FSW (Friction Stir Welding) [1]; however, instead of joining samples together, the process modifies the local microstructure of monolithic specimens to achieve specific and desired properties by surface modifying the microstructure (Fig. 1a). As in FSW, the tool induces plastic flow during the process, but depending on the selection of process parameters, i.e. applied force, travelling speed and rotational speed, the material flow can yield a modified microstructure that is beneficial to the performance/requirement of the material. Developed by Mishra in 2000, the modified process is a new and exciting technique for microstructural development and modification as well as property enhancement [2].

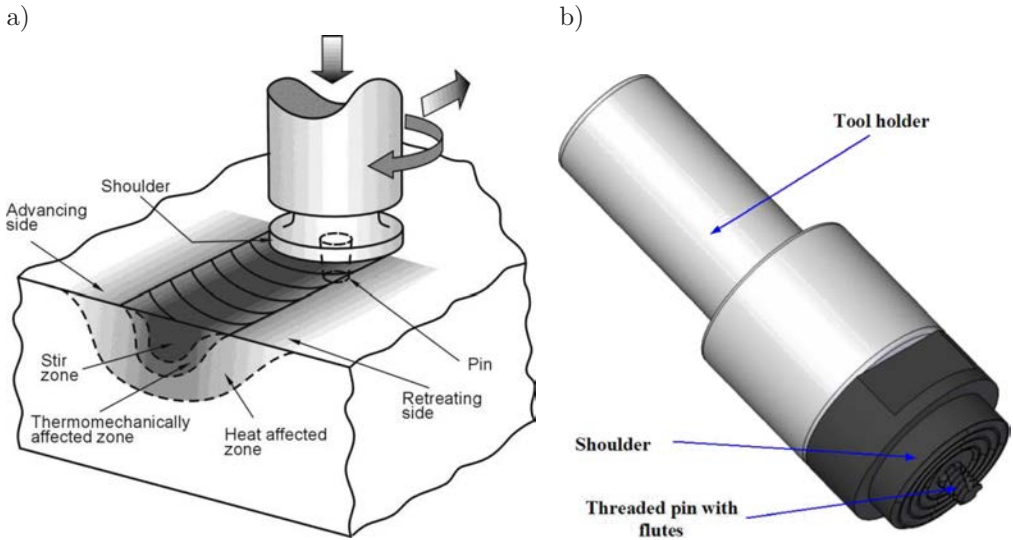


FIG. 1. Schematic drawing of Friction Modified Processing technique a) and tool b).

Friction stir welding is an energy-efficient, environmental-friendly and versatile joining technology that delivers superior strength, corrosion resistance and fatigue resistance when compared to conventional welding methods [2]. Developed and patented in 1991 [1] by The Welding Institute (TWI) – the United Kingdom, friction stir welding is a novel solid-state joining process that continues to gain popularity in the manufacturing sector [2, 3]. Prominent examples of FSW application include EADS/Airbus' utilization of friction stir welding to join aluminium components on the new A400M transport aircraft and Lockheed-Martin Michoud's use of FSW to join aluminium panel sections of the Space Shuttle's external fuel tank. Utilizing a rotating tool design, FSW induces plastic flow in the base materials and effectively stirs (or extrudes) the workpieces together. Since no melting occurs during FSW, the process is performed at much lower temperatures than conventional welding techniques and circumvents many of the environmental and safety issues associated with these welding methods. FSW produces a welded joint that is fundamentally defect-free and that displays excellent mechanical properties when compared to liquid state welds [3–5]. Due to these benefits, industries are embracing FSW technology and implementing new welding capabilities into their manufacturing sectors.

During the FSP process, a pin is plunged into the material with the shoulder of the rotating tool abutting the base metals (a tool without a pin can also be used). As the tool (Fig. 1) transverses the modified direction, the rotation of the shoulder under the influence of an applied load heats the metal surrounding the modified area and with the rotating action of the pin/shoulder induces

metal from each section to flow and form the modified area. The microstructure that evolves during FSP results from the influence of material flow, plastic deformation and elevated temperature and is characterized by a central stir zone surrounded by a thermomechanically affected zone (TMAZ) and heat affected zone (HAZ) as shown in Fig. 1. On the “advancing side” (Fig. 1) of the modified area, rotation of the tool is in the same direction as the modified direction, but on the “retreating side” (Fig. 1), rotation of the tool is in the opposite direction of the modified direction. In the FSP process the most important area is between the stir zone and the thermomechanically affected zone. This area will determine the properties of modified area, especially adhesion. In FSW the most important area is the stir zone, a key difference between the FSP and FSW processes. The second difference is that for FSP another critical area is the zone directly below the pin. This is less critical for FSW, which is concerned with the weld/joint quality throughout the thickness of the workpieces.

Numerous investigations have sought to characterize and model the FSW process, and the current status of friction stir research has been summarized well by Mishra [2] and Ma [6]. Friction Stir Processing involves complex processes such as flow of material, temperature distribution, rotary forces, tool design etc. that are not fully understood.

Although several numerical models of friction stir welding have been developed for the calculation of the heat generation rate [7, 8] and heat transfer and materials flow [7, 9], their testing has, for most part, been limited to the comparison of the numerically predicted temperatures *versus* time plots with the corresponding experimental data. A rigorous validation of numerical models must include examination of the model’s capability to predict several important features of the friction processing such as the torque, temperature, power needed for modification and the geometry of the stir zone as a function of important process parameters over a wide range of values.

In this paper the results of experimental trials and numerical modelling are presented. The main goal of this investigation was to determine the relationship between the process parameters of Friction Stir Processing and the torque acting on the tool and the temperature of the tool.

## 2. EXPERIMENTAL PROCEDURE

The chemical composition of the AlSi9Mg cast aluminium alloy used in this study is provided in Table 1. The base metal microstructure consists of coarse acicular Si particles distributed along the primary aluminium dendrite boundaries. Furthermore, the material exhibited numerous pores as shown in Fig. 2. Test plates were prepared from 6 mm thick plate with dimensions of 400 mm in length and 100 mm in width. Prior to tests, each plate was milled on both

**Table 1.** Chemical composition of cast aluminium alloy AlSi9Mg acc. to EN 1706 [10].

Chemical composition [%] mass							
Si	Fe	Cu	Mn	Mg	Zn	Ti	Al
9.0–10.0	0.19	0.05	0.10	0.25–0.45	0.07	0.15	balance

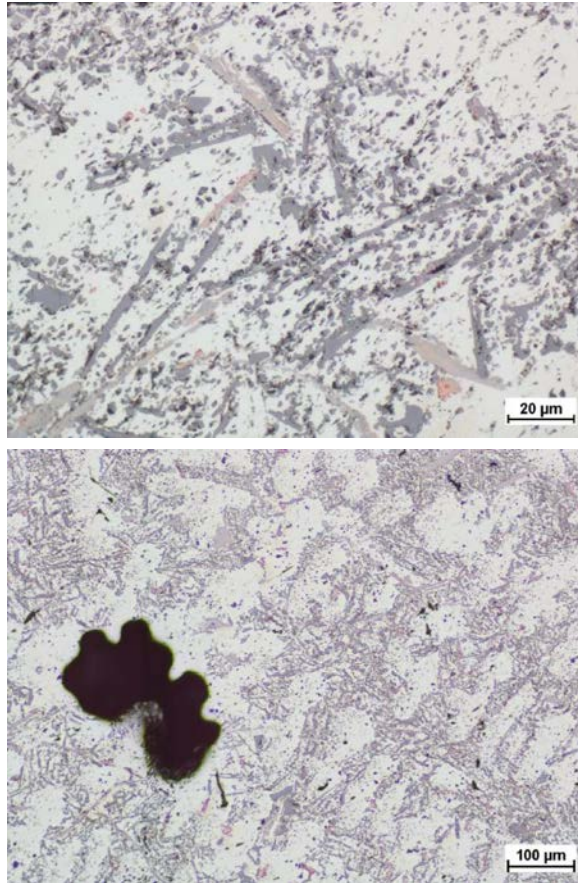


FIG. 2. Microstructure of parent material, cast aluminium alloy AlSi9Mg, light microscop.

sides to remove roughness as a result of casting. The plates, however, were not cleaned before experimentation.

A conventional tool with a scrolled shoulder (20 mm in diameter) and no pin was used for all the trials. The shoulder of the tool is manufactured from high speed tool steel -HS6-5-2. The geometry of the tool is shown in Fig. 3. A 0.5-deg head tilt was applied during plunge and FSP trials. Trials were conducted to determine the working range of rotation and travelling speeds. Thirty experimental conditions were taken into consideration (Fig. 4).



FIG. 3. The geometry of the FSP tool.

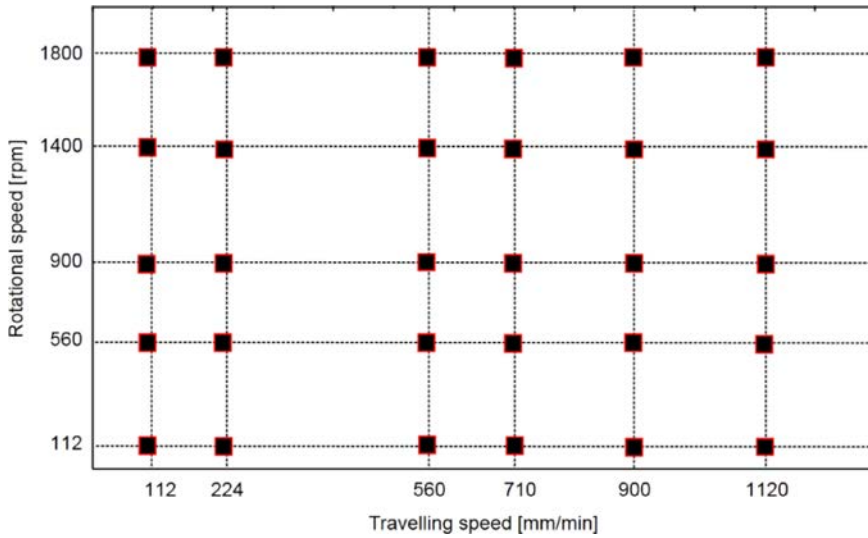


FIG. 4. Range of parameters utilised during experiments.

Transverse samples were removed from the modified plates for light metallographic analysis. Each sample was ground, polished through  $1\ \mu\text{m}$  diamond paste and final polished with a  $0.25\ \mu\text{m}$   $\text{Al}_2\text{O}_3$  suspension. Samples were analysed optically at magnifications up to  $500\times$  using a Nikon Eclipse MA 200 microscope without etching.

The TermSTIR device recorded the temperature of the tool. The variations in temperature during the processing were measured by a K-type thermocouple inserted to a place located  $1.0\ \text{mm}$  away from the tip of the rotating tool shoulder. The temperature of the tool was measured at  $60\ \text{Hz}$  of frequency. The mean value of the spindle torque, vertical force and down force were measured by the LOWSTIR head and calculated from 100 points in the area of the fully stabilized FSP process (Fig. 5) at a sampling rate of  $100\ \text{Hz}$ . It should be emphasized that the signals recorded during FSP are characteristic for the specific

tool geometry, parameters of the process, base material, measurement system (LOWSTIR) and experimental setup.

### 3. RESULTS AND DISCUSSION

#### 3.1. Experimental results of measurements

Data of torque and temperature for the changes of rotational and travelling speeds are shown in Figs. 5 to 8. As has been generally observed [11] increasing the rotational speed rapidly decreases the torque acting on the tool, as can be seen in Fig. 5. This is caused by the well-known phenomena for friction welding (rotary) in which an increase of the rotational speed causes a decrease in the torque [12] and the thickness of stir material layer [13]. In the FSP process the increase in rotational speed causes the volume of modified (stir) material to also become lower. And at this smaller volume the rotating tool generates a high amount of heat. Thus the temperature increases for increasing rotational speeds (Fig. 6) and causes the friction coefficient to decrease. Therefore, the “resistance” of the material becomes lower, thereby reducing the torque. An empirical relationship was developed to describe the relationship between torque and rotational speed. The evaluation of the rotational speed affecting the temperature of the modified material was successfully approximated by linear functions. The results of mathematical modelling for torque and for temperature are given in Tables 2 and 3, respectively.

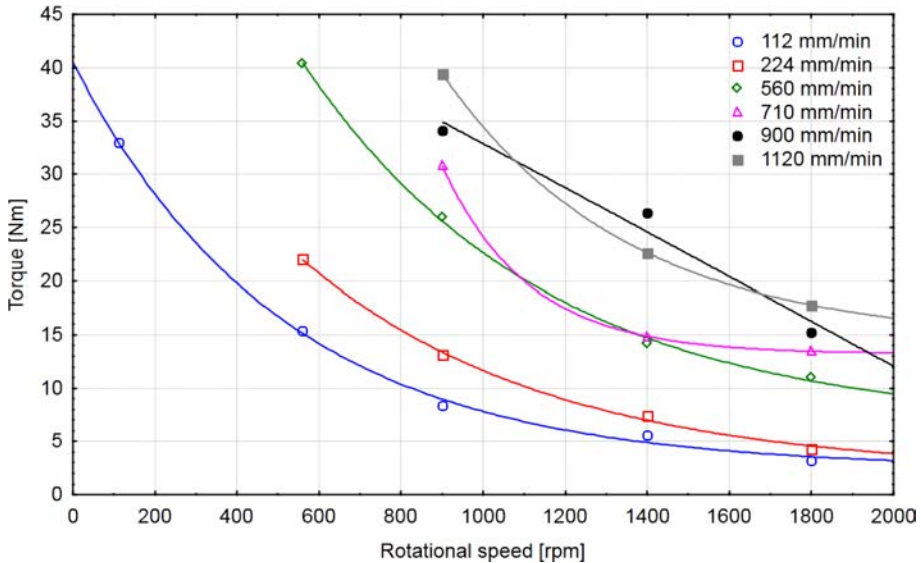


FIG. 5. Influence of the rotational speed on the torque acting on the tool at constant travelling speed.

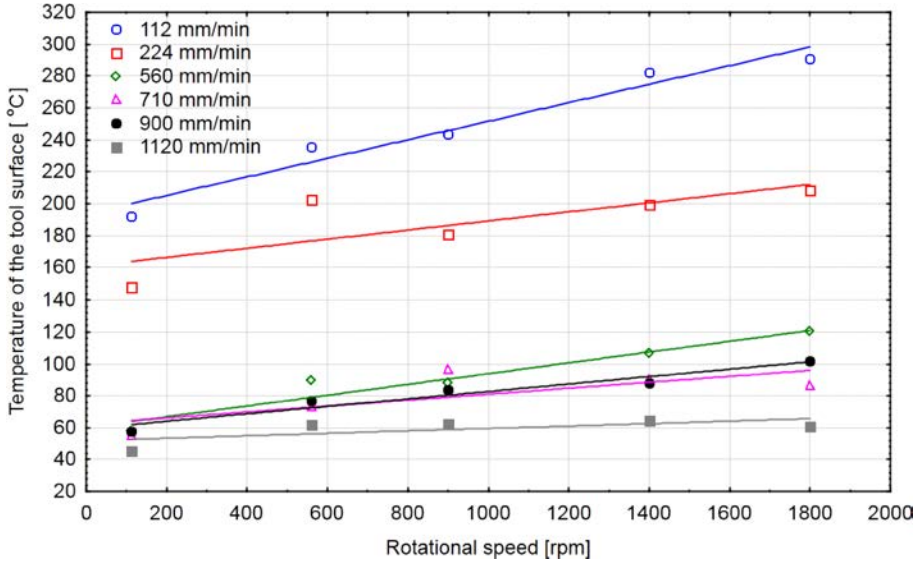


FIG. 6. Influence of rotational speed on tool temperature at constant travelling speed.

**Table 2.** The mathematical relationship between rotational speed ( $\omega$ ) and torque acting on the tool ( $M$ ) at constant travelling speed ( $v$ ).

No.	$v$ [mm/min]	Models
1	112	$M_{112} = 38.01 \cdot \exp(-\omega/509.78) + 2.46$
2	224	$M_{224} = 50.75 \cdot \exp(-\omega/600.77) + 2.04$
3	560	$M_{560} = 87.74 \cdot \exp(-\omega/590.46) + 6.51$
4	710	$M_{710} = 1265.79 \cdot \exp(-\omega/210.45) + 13.22$
5	900	$M_{900} = -1049.18 \cdot \exp(\omega/51865.59) + 1102.48$
6	1120	$M_{1120} = 184.79 \cdot \exp(-\omega/450.44) + 14.38$

**Table 3.** The mathematical relationships between rotational speed ( $\omega$ ) and tool temperature ( $T_p$ ) at constant travelling speed ( $v$ ).

No.	$v$ [mm/min]	Models
1	112	$T_{p112} = 193.61 + 0.58 \cdot \omega$
2	224	$T_{p224} = 160.71 + 0.03 \cdot \omega$
3	560	$T_{p560} = 60.11 + 0.03 \cdot \omega$
4	710	$T_{p710} = 62.45 + 0.02 \cdot \omega$
5	900	$T_{p900} = 59.44 + 0.02 \cdot \omega$
6	1120	$T_{p112} = 51.85 + 0.01 \cdot \omega$

The opposite trend can be observed for changes in travelling speed (Fig. 7). Increasing the travelling speed causes an increase in the torque. This phe-

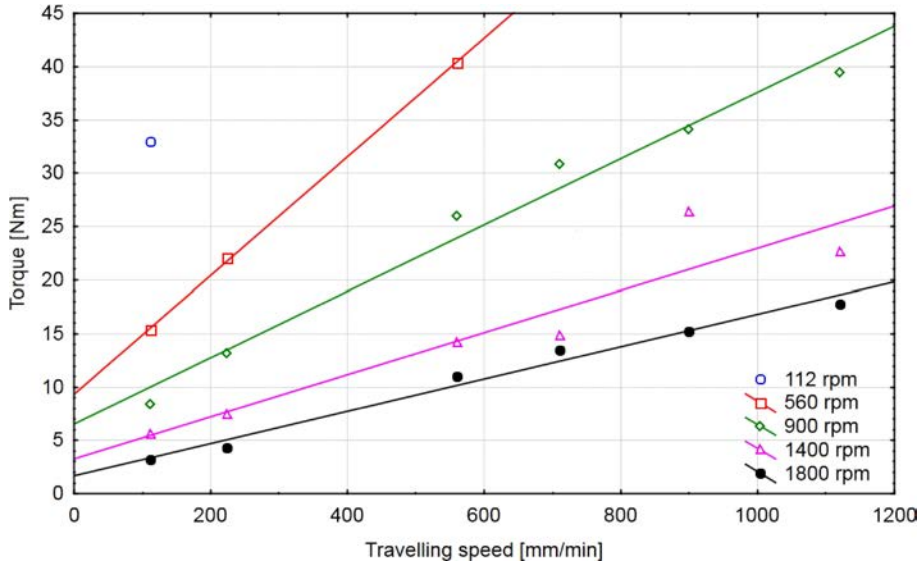


FIG. 7. The influence of the travelling speed on the torque acting on the tool at constant rotational speed.

nomenon is caused by the temperature changes during changes in the travelling speed. If the travelling speed increases, the total volume of stir material for each distance of linear travel of the tool decreases, so that small heat is generated. The temperature in the tool, therefore, becomes lower (Fig. 8). At low temperature the friction coefficient is high and the torque is higher for higher travelling

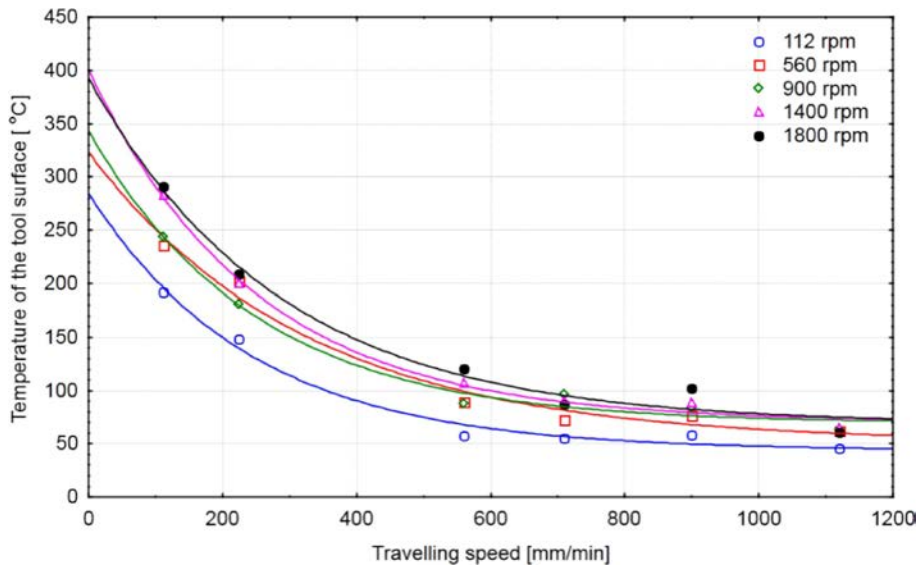


FIG. 8. The influence of travelling speed on tool temperature at constant rotational speed.

speeds. If the travelling speed is low, for single distance of travel the total volume of stir material is high so that the heat generated in the material is high. The temperature, therefore, is also high and the friction coefficient is lower. Hence the torque becomes lower. A linear formula has been found to describe the relationship between torque and travelling speed. The effect of travelling speed on the temperature of the modified material was successfully approximated by exponential functions. The results of mathematical modelling for torque and for temperature are given in Tables 4 and 5, respectively.

**Table 4.** The mathematical relationships between travelling speed ( $v$ ) and torque acting on the tool ( $M$ ) at constant rotational speed ( $\omega$ ).

No.	$\omega$ [rpm]	Models	Remarks
1	112	The mathematical formula cannot be determined because of too small number of measurements point	
2	560	$M_{560} = 9.36 + 0.06 \cdot v$	
3	900	$M_{900} = 6.53 + 0.03 \cdot v$	
4	1400	$M_{1400} = 3.26 + 0.02 \cdot v$	
5	1800	$M_{1800} = 1.71 + 0.02 \cdot v$	

**Table 5.** The mathematical relationships between travelling speed ( $v$ ) and tool temperature ( $T_p$ ) at constant rotational speed ( $\omega$ ).

No.	$\omega$ [rpm]	Models
1	112	$T_{p112} = 240.90 \cdot \exp(-v/243.53) + 43.86$
2	560	$T_{p560} = 272.02 \cdot \exp(-v/322.94) + 51.35$
3	900	$T_{p900} = 274.35 \cdot \exp(-v/247.36) + 69.28$
4	1400	$T_{p1400} = 330.36 \cdot \exp(-v/246.58) + 70.73$
5	1800	$T_{p1800} = 324.15 \cdot \exp(-v/283.23) + 68.68$

### 3.2. Results of metallographic examination

A representative light microstructure of the modified material is shown in Fig. 9. Two well defined regions can be easily distinguished: the parent material (lower area) and the FSP zone (upper area). The parent material is characterized by a coarse grain structure while the microstructure in the processed zone is modified by the tool action. The modified area resulted in the refinement of the microstructure. Figure 9 shows a region closer to the surface where the microstructure changes in a continuous way from that typical of the parent material to the refined one adjacent to the surface.

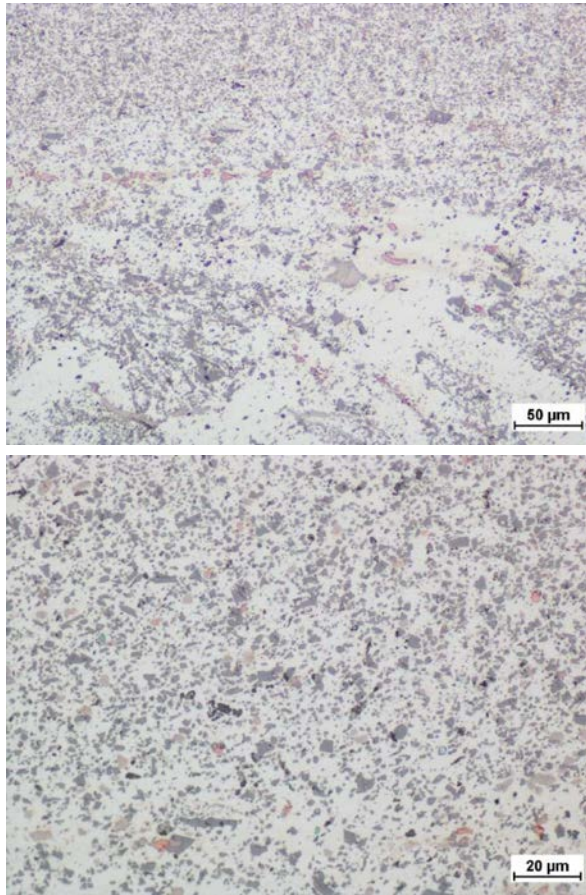


FIG. 9. A representative light microstructure of the FSP modified material – aluminium alloy AlSi9Mg.

High plastic deformation and material flow caused by the stirring action of the tool together with increased temperature due to friction phenomena are responsible for the refinement of grains and dynamic recrystallization in the modified area [14]. FSP also reduced casting pores and caused homogenization of the microstructure. As a result of FSP the as-cast material is converted into a near-wrought condition. This homogenized and refined microstructure along with the reduced porosity results in improved mechanical properties [15, 16]. It is also evident from the present study that the dramatic change in microstructure occurs even when a tool without a pin is used during FSP.

### 3.3. Modelling of the FSP process

Adapted from the friction stir welding thermal model presented by Hamilton et al. in [17], a thermal model was developed for friction stir processing utiliz-

ing COMSOL multi-physics software. As an initial simplification to the model, only heat generation due to the friction between tool and the workpiece was considered, i.e. heat generation due to plastic deformation was not taken into account. Based upon these conditions, the heat generation at the tool/workpiece interface,  $q$ , may be expressed as [17]:

$$(3.1) \quad q = \delta_E \mu P_N (\omega r - v_x \sin \theta),$$

where  $\delta_E$  is an energy-based slip factor,  $\mu$  is the coefficient of friction between the tool and the workpiece,  $P_N$  is the normal pressure relative to the tool face,  $\omega$  is the angular velocity of the tool,  $r$  is the radial distance measured from the tool center,  $v_x$  is the tool velocity and  $\theta$  is the radial angle measured about the tool axis.

For typical tool velocities during friction stir welding, the  $v_x \sin \theta$  term in Eq. (3.1) becomes small relative to the  $\omega r$  term and is often ignored. For the FSP process, however, the magnitude of certain tool velocities that were utilized, such as 900 mm/min and 1120 mm/min, makes the  $v_x \sin \theta$  term non-negligible. Therefore, Eq. (3.1) was evaluated with  $\theta = 90^\circ$ , and the heat generation was averaged over the tool/workpiece interface to yield the following expression for the tool heat flux,  $q_{tool}$ :

$$(3.2) \quad q_{tool} = \frac{\int_0^{r_{\text{interface}}} \delta_E \mu P_N (\omega r - v_x) r \, dr \, d\theta}{\pi r_{\text{interface}}^2} = \delta_E \mu P_N \left( \frac{2}{3} \omega r_{\text{interface}} - v_x \right),$$

where  $r_{\text{interface}}$  is the radius of the tool face in contact with the workpiece. Basically, the FSP process stabilizes after approximately 10 seconds of runtime [18]. Prior to stabilization, the vertical force (as well as the torque) increases approximately linearly during the ramping period. Since the heat flux is directly proportional to the vertical force, a linear ramp for the heat flux was incorporated into the thermal model such that for runtimes less than or equal to 10 seconds ( $t \leq 10$ ), the heat flux utilized in the thermal model,  $q_{\text{model}}$ , is given by:

$$(3.3) \quad q_{\text{model}} = \left( \frac{q_{\text{tool}}}{10} \right) t.$$

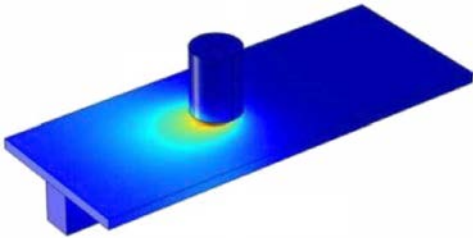
Beyond 10 seconds, i.e. after stabilization, the heat flux from Eq. (3.2) was used in the model.

In the first step the influence of pitch (rotational speed/travelling speed) on temperature at constant travelling speed was determined. Four numerical simulations were performed at a constant travel speed of 224 mm/min for the

following tool rotation speeds: 560, 900, 1400 and 1800 rpm. The predicted maximum surface temperatures for these simulations are summarized in Fig. 10. Included in the figure are the experimentally measured surface temperatures. As seen in the figure, though the predicted surface temperatures follow the same trend as the experimental values relative to the pitch, the thermal model under-predicts the processing temperature for the largest pitch (slowest rotation speed) and over-predicts the temperature for the two smallest pitches (the highest rotation speeds). The inability of the model to accurately predict the temperature at the highest pitch is most likely due to the fact that the thermal model does not presently capture heat generation due to plastic deformation. At slower rotation speeds, the processing energy transferred into the workpiece is reduced; therefore, the flow stress of the workpiece remains relatively high. As such, plastic deformation significantly contributes to the total heat generation.

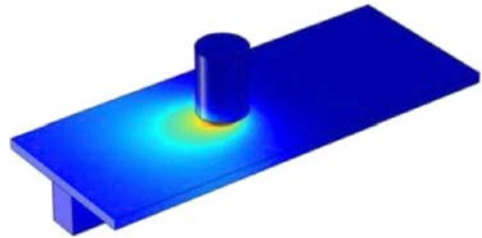
a)

Travel Speed: 224 mm/min  
RPM: 560  
Experimental Temp.: 194°C  
Thermal Model Temp.: 156°C



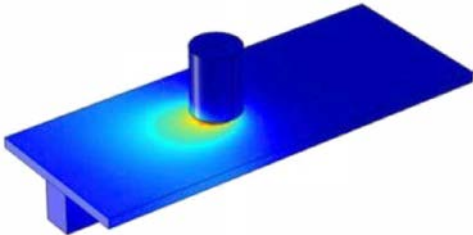
b)

Travel Speed: 224 mm/min  
RPM: 900  
Experimental Temp.: 203°C  
Thermal Model Temp.: 200°C



c)

Travel Speed: 224 mm/min  
RPM: 1400  
Experimental Temp.: 208°C  
Thermal Model Temp.: 248°C



d)

Travel Speed: 224 mm/min  
RPM: 1800  
Experimental Temp.: 211°C  
Thermal Model Temp.: 249°C

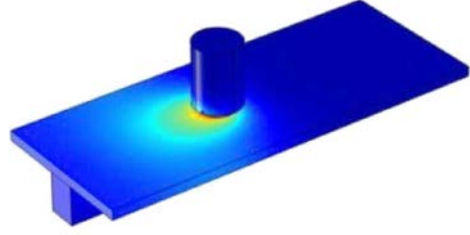


FIG. 10. Influence of pitch on temperature at constant travel speed:  
a) 0.4, b) 0.25, c) 0.16, d) 0.12.

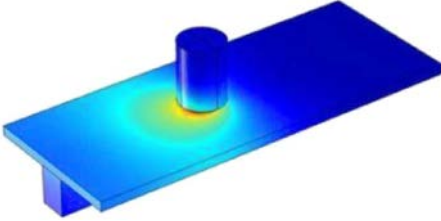
The temperature over-predictions by the model at smaller pitches may be related to the slip factor,  $\delta_E$ , utilized to calculate the heat flux (Eq. (3.1)). As previously discussed, the current model for FSP was adapted from a thermal model for friction stir welding for which  $\delta_E$  represents the efficiency of frictional heat transfer. During friction stir welding, both a pin that is inserted into the workpiece and a shoulder that is in contact with the workpiece transfer frictional heat into the system, creating three heat generating surfaces: the pin bottom, the pin sides and the tool shoulder. During FSP, however, there is only one heat generating surface – the interface between the tool and the workpiece. The heat transfer during FSP, therefore, may be less efficient than during friction stir welding and is not accounted for by the current formulation of  $\delta_E$ . For processing conditions for which heat generation due to friction dominates, such as at smaller pitches, the thermal model over-predicts the surface temperatures.

Secondly the influence of pitch on temperature at constant rotational speed was established. Six numerical simulations were performed at a constant rotational speed of 900 rpm for the following tool travelling speeds: 112, 224, 560, 710, 900 and 1120 mm/min. The predicted maximum surface temperatures for these simulations are summarized in Fig. 11. Included in the figure are the experimentally measured surface temperatures. As indicated in this figure for this rotational speed and associated travelling speeds, the experimental temperatures decline from approximately 250°C for pitch values less than 0.2 and then level off at approximately 100°C for pitch values greater than 0.8. Unfortunately, the thermal model failed to capture this experimental behaviour. Instead, the thermal model predicts that the surface temperatures for these conditions should begin at approximately 190°C for a pitch value of 0.12, rise to a maximum temperature of nearly 250°C at a pitch of 0.62, and ultimately fall to 145°C for the highest pitch value of 1.24.

Certainly the limitations of the model discussed in the previous section regarding heat generation due to plastic deformation and the slip factor can contribute to the discrepancies observed for these process conditions. In this instance, however, the effect of travel speed may be the primary cause for the discrepancies. Equation (3.2) captures the effect of travel speed in the  $(\omega r - v_x)$  term, reducing the heat flux as the travel speed increases. This equation, however, assumes that the heat generating surfaces of the tool are in perfect contact with the workpiece. At travel speeds typical to friction stir welding, such as 127 mm/min, this assumption is undoubtedly valid. As the travel speed increases to values like those used in this investigation, such as 900 mm/min or 1120 mm/min, the efficiency of heat transfer from the tool to the workpiece could be reduced by the influence of these speeds on the tool/workpiece interface. As a result, the thermal model over-predicts the surface temperatures for these process conditions as the pitch increases.

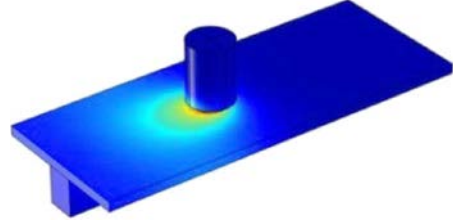
a)

Travel Speed: 112 mm/min  
 RPM: 900  
 Experimental Temp.: 250°C  
 Thermal Model Temp.: 186°C



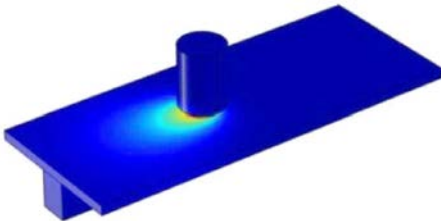
b)

Travel Speed: 224 mm/min  
 RPM: 900  
 Experimental Temp.: 203°C  
 Thermal Model Temp.: 200°C



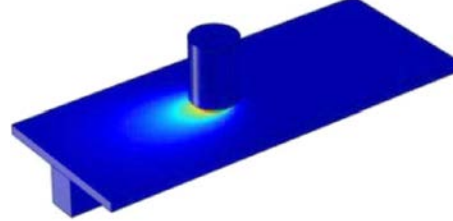
c)

Travel Speed: 560 mm/min  
 RPM: 900  
 Experimental Temp.: 140°C  
 Thermal Model Temp.: 247°C



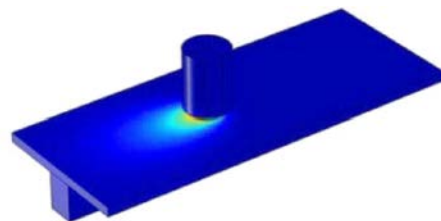
d)

Travel Speed: 710 mm/min  
 RPM: 900  
 Experimental Temp.: 100°C  
 Thermal Model Temp.: 219°C



e)

Travel Speed: 900 mm/min  
 RPM: 900  
 Experimental Temp.: 100°C  
 Thermal Model Temp.: 177°C



f)

Travel Speed: 1120 mm/min  
 RPM: 900  
 Experimental Temp.: 100°C  
 Thermal Model Temp.: 145°C

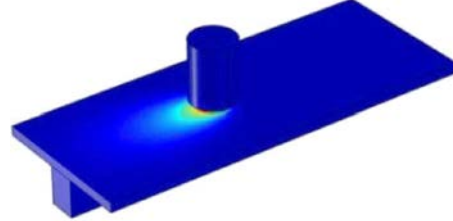


FIG. 11. Influence of pitch on temperature at constant rotational speed:  
 a) 0.12, b) 0.25, c) 0.62, d) 0.79, e) 1.00 and f) 1.24.

#### 4. CONCLUSIONS

The effects of rotational and travelling speeds on the torque and temperature of the tool were investigated for FSP of cast aluminium plates using experimen-

tal techniques and numerical modelling. The simulated temperatures were compared to measured values. From the simulation and experiments, the following are observed:

- The torque decreases with an increase in the rotational speed because it becomes easier for the material to flow at higher temperatures and strain rates. For an increasing temperature of the surface, the friction coefficient becomes lower. This is also due to the well-known relationship, from the conventional friction welding, that an increase in the rotational speed decreases the volume of mixed material.
- Changes in travelling speed influence the torque and temperature in opposite directions. An increase in the travelling speed decreases the temperature and increases the torque acting on the tool. This is due to the fact that an increase in the travelling speed raises the resistance of mixed materials, and a much higher volume of material is mixed per tool revolution.
- It is also evident from the present study that a dramatic change in the microstructure occurs, even when a tool without a pin is used during FSP. The modification process resulted in a significant breakup of large Si particles and subsequent uniform distribution in the aluminium matrix. Furthermore, porosity in the as cast AlSi9Mg was nearly eliminated by FSP.
- In the presented numerical model only heat generation due to the friction between tool and the workpiece was considered. The limitations of the presented model regarded heat generation due to plastic deformation and the slip factor. The influence of pitch on temperature at constant travelling and rotational speeds was determined. As a result, the thermal model over-predicts the surface temperatures for these process conditions as the pitch increases at constant rotational speed. At constant travelling speed the experimental and modelling results correspond.

#### ACKNOWLEDGMENT

The authors would like to thank the Ministry of Science and Higher Education in Poland for founding this work and Miami University for the support of our investigations.

#### REFERENCES

1. THOMAS W.M., NICHOLAS E.D., NEEDHAM J.C., MUCH M.G., TEMPLESMITH P., DAWES C.J., GB Patent Application No 9125978.8, 1991.
2. MISHRA R.S., MA Z.Y., *Friction stir welding and processing*, Materials Science and Engineering R: Reports, **50**, 1–2, 1–78, 2005.
3. THREADGILL P.L., LEONARD A.J., SHERCLIFF H.R., WITHERS P.J., *Friction stir welding of aluminium alloys*, International Materials Review, **54**, 2, 49–93, 2009.

4. MISHRA R.S., MAHONEY M.W., *Friction stir welding and friction stir processing*, ASM International, Materials Park (Ohio) 2007.
5. HAMILTON C., DYMEK S., Blicharski M., *Mechanical properties of Al 6101-T6 welds by friction stir welding and metal inert gas welding*, Archives of Metallurgy and Materials, **52**, 1, 67–72, 2007.
6. MA Z.Y., *Friction Stir Processing Technology – A review*, Metallurgical and Materials Transactions A, **39 A**, 3, 642–658, 2008.
7. ARORA A., NANDAN R., REYNOLDS A.P., DEBROY T., *Torque, power requirement and stir zone geometry in friction stir welding through modeling and experiments*, Scripta Materialia, **60**, 1, 13–16, 2009.
8. KHANDKAR M.Z.H., KHAN J.A., *Prediction of temperature distribution and thermal history during friction stir welding: input torque based model*, Science and Technology of Welding and Joining, **8**, 3, 165–174, 2003.
9. COLEGROVE P.A., SHERCLIFF H.R., *Two-dimensional CFD modelling of flow round profiled FSW tooling*, Science and Technology of Welding and Joining, **9**, 6, 483–492, 2004.
10. EN 1706:2010 Aluminium and aluminium alloys – Castings – Chemical composition and mechanical properties.
11. CUI S., CHEN Z.W., ROBSON J.D., *Interrelationships among speeds, torque and flow volumes during friction stir welding/processing*, 8th International Friction Stir Welding Symposium, 18–20 May 2010, Timmendorfer Strand, Germany.
12. LEBIEDIEV W.K., CIERNIENKO I.A., WILIJA W.I., *Friction welding – handbook* [in Russian: *Svarka Treniem. Spravochnik. Izdatelstwo Maszinostronije*], Leningrad 1987.
13. PILARCZYK J., PIETRAS A., *Mechanism of heat release and propagation during friction welding of high speed to constructional steels*, International Conference Welding and Related Technologies for the 21st Century, Kiev Ukraine, 1998.
14. KARTHIKEYAN L., SENTHILKUMAR V.S., BALASUBRAMANIAN V., NATARAJAN S., *Mechanical property and microstructural changes during friction stir processing of cast aluminium 2285 alloy*, Materials and Design, **30**, 6, 2237–2242, 2009.
15. MAHMOUD T.S., GAAFER A.M., KHALIFA T.A., *Effect of tool rotational and welding speeds on microstructural and mechanical characteristics of friction stir welded A319 cast Al alloy*, Materials Science and Technology, **24**, 5, 553–559, 2008.
16. JAYARAMAN M., SIVASUBRAMANIAN R., BALASUBRAMANIAN V., BABU S., *Influences of process parameters on tensile strength of Friction Stir welded cast A319 aluminium alloy joints*, Metals and Materials International, **15**, 2, 313–320, 2009.
17. HAMILTON C., DYMEK S., SOMMERS A., *A thermal model of friction stir welding in aluminum alloys*. International Journal of Machine Tools & Manufacture, **48**, 1120–1130, 2008.
18. WĘGŁOWSKI M.ST., *An experimental study on the Friction Stir Processing process of aluminium alloy*. Key Engineering Material, 2013 in print.

*Received December 5, 2012.*

---

**3<sup>rd</sup> International Conference on Material Modelling**  
incorporating  
**13<sup>th</sup> European Mechanics of Materials Conference**

September 9–11, 2013  
Warsaw, Poland

The logo for the International Conference on Material Modelling (ICMM) features the letters 'ICMM' in a stylized font. The 'I' is a solid orange vertical bar. The 'C' is a solid black circle. The 'M' is a solid orange shape with a pointed top. The second 'M' is also solid orange but has a white outline.

Following the tradition of the ICMM series, which took place in Dortmund (2009) and Paris (2011) respectively, the ICMM3 conference will take place in Warsaw, in the Old Library Building at the University of Warsaw.

**Main topics planned for ICMM3:**

- Linear elasticity and viscoelasticity
- Nonlinear elasticity
- Plasticity and viscoplasticity
- Strain gradient approaches
- Nonclassical approaches
- Atomistic/continuum transition on nanoscale
- Optimization and inverse problems in multiscale modelling
- Granular materials and particle systems
- Biomechanics and biomaterials
- Electronic materials
- Heterogeneous materials
- Coupled field problems
- Creep, damage and fatigue
- Experimental identification and material characterization

**Lectures and posters:** No opening, general, plenary nor keynote lectures are planned. According to the tradition of ICMM all speakers will have the equal time of presentation lasting 20 minutes. A poster session is also planned.

**Venue, facilities, lecture rooms, accommodations:** The Old Library Building of the University of Warsaw is situated in the central pedestrian zone which leads to the Old Town. In the close neighbourhood of the conference venue there are a plethora of restaurants and cafes with various standard and prices. A variety of hotels of different standard and prices are located in the vicinity of the conference venue.



**Social programme:** The *gala dinner banquet* and *welcome party* will be organized for participants.

**Conference fee:** Early Registration: 300 €  
Late Registration: 350 €  
Conference Dinner: 40 €

**Tentative Schedule:** September 8: Registration & Welcome Party  
September 9: Talks  
September 10: Talks & Poster Session  
September 11: Talks & Conference Dinner

**Important Dates:** Abstract Submission Closes: May 15, 2013  
Abstract Acceptance Decision: June 1st, 2013  
Early Registration Closes: June 15, 2013  
Paper Submission: Sept. 30, 2013

**Conferences organizer:** ICMM3 conference is organized by IPPT in cooperation with EUROMECH and the Committee of Mechanics PAN.

### **Scientific Committee:**

- Douglas J. Bammann, Mississippi State University, USA
- Frederic Barlat, Pohang University of Science and Technology, Korea
- Albrecht Bertram, University of Magdeburg, Germany
- Paweł Dłużewski, Institute of Fundamental Technological Research PAN, Warsaw, Poland
- Fionn Dunne, University of Oxford, UK
- Yuri Estrin, Monash University, Melbourne, Australia
- Samuel Forest, Mines ParisTech, Paris, France
- Marc Geers, Eindhoven University of Technology, The Netherlands
- Sanjay Govindjee, University of California, Berkeley, USA
- Istvan Groma, Eötvös University, Budapest, Hungary
- Gerhard A. Holzapfel, Graz University of Technology, Austria;  
Royal Institute of Technology, Sweden
- Dave McDowell, Georgia Institute of Technology, USA
- Nobutada Ohno, Nagoya University, Japan
- Roberto Paroni, University di Sassari, Alghero, Italy
- Arun Srinivasa, Texas A&M University, College Station, USA
- Srinivasan M. Sivakumar, Indian Institute of Technology, Madras, India
- Bob Svendsen, RWTH Aachen University, Germany
- George Voyiadjis, Louisiana State University, USA
- Zheng Quan-Shui, Tsinghua University, Beijing, China

### **Local Organizing Committee:**

Paweł Dłużewski – Chairman  
Grzegorz Jurczak – Secretary  
Jan Cholewiński  
Grzegorz Maciejewski  
Marcin Maździarz  
Piotr Przybyła  
Agnieszka Rutecka  
Piotr Tauzowski  
Toby D. Young

### **Detailed information:**

Please visit ICMM3 homepage at: <http://icmm3.ippt.gov.pl>.

You may download the ICMM3 flyer at: [http://icmm3.ippt.gov.pl/icmm3\\_flyer.pdf](http://icmm3.ippt.gov.pl/icmm3_flyer.pdf).

## Aims and Scope

ENGINEERING TRANSACTIONS promotes research and practise in engineering science and provides a forum for interdisciplinary publications combining mechanics with material science, electronics (mechanotronics), medical science and biotechnologies (biomechanics), environmental science, photonics, information technologies and other engineering applications. The Journal publishes original papers covering a broad area of research activities including experimental and hybrid techniques as well as analytical and numerical approaches. Engineering Transactions is a quarterly issued journal for researchers in academic and industrial communities.

## INTERNATIONAL COMMITTEE

S. A. ASTAPCIK ( <i>Byelorussia</i> )	P. PERZYNA ( <i>Poland</i> )
A. CARPINTERI ( <i>Italy</i> )	L. TOTH ( <i>France</i> )
G. DOBMANN ( <i>Germany</i> )	Z. WESOŁOWSKI ( <i>Poland</i> )
T. IWAMOTO ( <i>Japan</i> )	P. WOOD ( <i>U.K.</i> )
A. N. KOUNADIS ( <i>Greece</i> )	G. VOYIADJIS ( <i>USA</i> )
J. LIN ( <i>U.K.</i> )	R. ZAERA ( <i>Spain</i> )
T. ŁODYGOWSKI ( <i>Poland</i> )	

## EDITORIAL COMMITTEE

R. PEŁCHERSKI – <b>Editor</b>	A. RUSINEK – <b>Co Editor</b>
Z. AZARI	K. KOWALCZYK-GAJEWSKA
P. CHEVRIER	Z. KOWALEWSKI
B. GAMBIN	P. LIPIŃSKI
J. HOLNICKI-SZULC	K. KRIEDEL – assistant of the Co Editor

ENIM, 1 route d’Ars Laquenexy  
57078 Metz Cedex 03

Phone: +33 3 87344266, E-mail: relinter@enim.fr

J. ŻYCHOWICZ-POKULNIEWICZ – secretary

Address of the Editorial Office:

Engineering Transactions  
Institute of Fundamental Technological Research  
Pawińskiego 5B, PL 02-106 Warsaw, Poland

Phone: (48-22) 826 12 81 ext. 206, Fax: (48-22) 826 98 15, E-mail: engtrans@ippt.pan.pl

## Abstracted/indexed in:

Applied Mechanics Reviews, Current Mathematical Publications, Elsevier, EMBASE, Engineering Village, Inspec, Mathematical Reviews, MathSci, Reaxys, Scopus, Zentralblatt für Mathematik.

<http://et.ippt.pan.pl/>

## DIRECTIONS FOR THE AUTHORS

The periodical *ENGINEERING TRANSACTIONS (ROZPRAWY INŻYNIERSKIE)* presents original papers which should not be published elsewhere.

As a rule, the volume of a paper should not exceed 40 000 typographic signs. The following directions are particularly important:

1. **The paper submitted for publication should be written in English.**
2. The title of the paper should be as short as possible. The text should be preceded by a brief introduction; it is also desirable that a list of notations used in the paper should be given.
3. Short papers should be divided into section and subsection, long papers into sections, subsections and points. Each section, subsection or point must bear a title.
4. The formula number consists of two figures: the first represents the section number and the other the formula number in that section. Thus the division into subsections does not influence the numbering of formulae. Only such formulae should be numbered to which the author refers throughout the paper. This also applies to the resulting formulae. The formula number should be written on the left-hand side of the formula; round brackets are necessary to avoid any misunderstanding. For instance, if the author refers to the third formula of the set (2.1), a subscript should be added to denote the formula, viz. (2.1)<sub>3</sub>.
5. All the notations should be written very distinctly. Special care must be taken to distinguish between small and capital letters as precisely as possible. Semi-bold type must be underlined in black pencil. Explanations should be given on the margin of the manuscript in case of special type face.
6. Vectors are to be denoted by semi-bold type, transforms of the corresponding functions by tildes symbols. Trigonometric functions are denoted by sin, cos, tan and cot, inverse functions – by arcsin, arccos, arctan and arccot; hyperbolic functions are denoted by sh, ch, th and cth, inverse functions – by Arsh, Arch, Arth and Archth.
7. The figures in square brackets denote reference titles. Items appearing in the reference list should include the initials of the first name of the author and his surname, also the full of the paper (in the language of the original paper); moreover:
  - a) In the case of books, the publisher's name, the place and year of publication should be given, e.g., 5. ZIEMBA S., *Vibration analysis*, PWN, Warszawa 1970;
  - b) In the case of a periodical, the full title of the periodical, consecutive volume number, current issue number, pp. from ... to ..., year of publication should be mentioned; the annual volume number must be marked in semi-bold type as to distinguish it from the current issue number, e.g., 6. SOKOŁOWSKI M., *A thermoelastic problem for a strip with discontinuous boundary conditions*, Arch. Mech., **13**, 3, 337–354, 1961.
8. The authors should enclose a summary of the paper. The volume of the summary is to be about 100 words, also key words are requested.
9. The preferable format for the source file is TeX or LaTeX while MS Word is also acceptable. Separate files for the figures should be provided in one of the following formats: EPS or PostScript (preferable), PDF, TIFF, JPEG, BMP, of at least 300 DPI resolution. The figures should be in principle in gray-scale and only if necessary the color will be accepted.

Upon receipt of the paper, the Editorial Office forwards it to the reviewer. His opinion is the basis for the Editorial Committee to determine whether the paper can be accepted for publication or not.

Once the paper is printed, the issue of Engineering Transactions free of charge is sent to the author. Also the PDF file of the paper is forwarded by the e-mail to the authors.

*Editorial Committee*  
*ENGINEERING TRANSACTIONS*